UNIVERSITY OF KWAZULU-NATAL

Radio Wave Propagation Modeling under Precipitation and Clear-air at Microwave and Millimetric Bands over Wireless Links in the Horn of Africa

Feyisa Debo Diba

February, 2017

Supervisor: Professor Thomas J. Afullo

Co-supervisor: Dr. Akintunde Ayodeji Alonge

Radio Wave Propagation Modeling under Precipitation and Clear-air at Microwave and Millimetric Bands over Wireless Links in the Horn of Africa

Feyisa Debo Diba

In fulfillment of the Degree of Doctor of Philosophy in Electronic Engineering, College of Agriculture, Engineering and Science, University of KwaZulu-Natal, Durban

February, 2017

Supervisor:

As the candidate's Supervisor, I agree/do not agree to the submission of this thesis

Professor T.J. Afullo ————————————-

Date————————————————

Co-Supervisor:

Dr. Akintunde Ayodeji Alonge

As the candidate's Co.Supervisor, I agree to the submission of this thesis

Dr. A. A. Alonge ————————————-

Date————————————————

DECLARATION 1 - PLAGIARISM

I, Feyisa Debo Diba, with Student Number 214584673,with the thesis entitled "Radio wave Propagation Modeling under Precipitation and Clear-air at Microwave and Millimetric Bands over Wireless Links in the Horn of Africa," declare that

1. The research reported in this thesis, except where otherwise indicated, is my original research.

2. This thesis has not been submitted for any degree or examination at any other university.

3. This thesis does not contain other persons data, pictures, graphs or other information, unless specifically acknowledged as being sourced from other persons.

4. This thesis does not contain other persons' writing, unless specifically acknowledged as being sourced from other researchers. Where other written sources have been quoted, then: a. Their words have been re-written but the general information attributed to them has been referenced b. Where their exact words have been used, then their writing has been placed in italics and inside quotation marks, and referenced.

5. This thesis does not contain text, graphics or tables copied and pasted from the Internet, unless specifically acknowledged, and the source being detailed in the thesis and in the References sections.

Signed.....Date .....

DECLARATION 2 - PUBLICATIONS

DETAILS OF CONTRIBUTION TO PUBLICATIONS that form part and/or include research presented in this thesis (include publications in preparation, submitted, in press and published and give details of the contributions of each author to the experimental work and writing of each publication).

JOURNAL PUBLICATIONS

- **F. D. Diba**, T. J. Afullo and A. A. Alonge, "Rainfall Rate and Attenuation Performance Analysis at Microwave and Millimeter Bands for the Design of Terrestrial Line-of-Sight Radio Links in Ethiopia," SAIEE African Research Journal, Vol.107 (3).pp. 177- 186, September 2016.

- **Feyisa D. Diba**, Thomas J. Afullo and Akintunde A. Alonge, "Rainfall Characterization and Generation from Markov Chains for Rain Fade Modeling over Wireless Links in Ethiopia," Submitted to IET Journal of Microwave,Antennas and Propagation, United Kingdom, September 2016.

CONFERENCE PROCEEDINGS

- **Feyisa D. Diba** and Thomas J. Afullo, "Estimation of Rain Attenuation over Microwave and Millimeter Bands for Terrestrial Radio Links in Ethiopia," Proceedings of 2015 IEEE AFRICON Conference, Addis Ababa, Ethiopia, September 14 - 17 , 2015.

- **Feyisa D. Diba**, Thomas J. Afullo, and Akintunde A. Alonge, "Time Series Rainfall Spike Modelling from Markov Chains and Queueing Theory Approach for Rainfall Attenuation over Terrestrial and Earth-space Radio Wave Propagation in Jimma,

Ethiopia," Proceedings of 2016 PIERS Conference, Shanghai, China, August 8- 11 , 2016.

Signed.....Date .....

Acknowledgements

First of all, I would like to thank God who has offered me grace and strength to complete this work successfully.

I would like to express my special thanks and appreciation to my supervisor and Discipline Academic Leader, Department of Electrical, Electronic and Computer Engineering, Professor Thomas J. Afullo, and my Co-supervisor, Dr. Akintunde Alonge, for advising, encouraging and allowing me to grow as a research scientist. Your support, professional guidance and constructive criticism during my study are highly appreciated.

Special thanks to Jimma University and the Ethiopian Ministry of Education for giving me the opportunity to carry out my doctoral study and for offering financial support.

I sincerely appreciate Ethiopian National Meteorological Agency for providing rainfall intensity and clear-air radio-climatological data used in this study.

I would like to acknowledge and appreciate Ethio Telecom and Mr. Feromsa Girma Temesgen for providing measured signal level data for this study.

The assistance of Mr.Vuttaradi Anand, Dr. Kinde Anlye and Mr. Mohammed Muntaz of Jimma University are appreciated and acknowledged for the provision of rainfall data from the Davis Vantage weather station installed at Jimma, Ethiopia every week and for taking care of the equipment.

I would like to express my appreciation to my dear friends, Mr.Ahmed Kedir and Shemsedin Kedir, who have been supportive throughout my doctoral studies in one way or the other. I would like to thank my love, Aisha Muhammed, for being patient and understanding during my study.

Additionally, I want to express gratitude to my colleagues: Mr.Wehib Abubeker, Mr.Ayele Legesse, Mr.Getahun Aklilu, Mr. Dauda Ayanda, Mr.Modisa Mosalaosi, Mr.Mike Asiyo, Mr.Jide Afolayan, Mr. Sumbir Djuma and Mr. Ebenezer Esenogho, for their accompany.

Dedication

This thesis is dedicated to my mother, the late Safiya Kawo Geda, and my grandmother, the late Dadhi Mudde.

I would not be who I am today without their genuine prayer, love, support and inspiration

Abstract

The congestion of lower operating frequency bands has led to the rapid growth of utilizing higher frequency spectrum for wireless communication systems. However, attenuation caused by precipitation is the main problem for systems operating at higher frequency bands. For this reason, for efficient operation of wireless networks, this problem should be properly addressed.

This thesis has investigated the radio wave propagation modelling under clear air and precipitation environment over wireless communications in the horn of Africa. The research emphasises both precipitation and clear air effects over radio links in Ethiopia. Radio climatological parameters for different rain and clear air fade models are adequately derived. To this end, three years of atmospheric data of temperature, pressure and relative humidity obtained from National Meteorological Agency (NMA) of Ethiopia and clear air signal measurements over terrestrial Line-of-Sight (LOS) links measured with EthioTelecom for a period of one year are used for clear air fade modelling and analysis. On the other hand, based on experimental measurements of rainfall from a Davis Vantage weather station installed at Jimma University, Ethiopia, time series rainfall generation and characterization is also done.

Clear air fading is modeled either from radio-climatological parameters or from extensive signal level measurements over wireless links. In terrestrial LOS links, prediction of the refractivity gradient uses ITU-R worldwide contour map. However, in this work, data from NMA is used for the determination of refractivity and refractivity gradient. Applying the ITU-R model, the geo-climatic factor is derived from atmospheric refractivity. Geo-climatic factor, in turn, is used for the estimation of fade depth, outage probability and multipath fading distribution over existing path lengths and operating frequencies for four different locations of Ethiopia. From clear air signal measurements, the distribution of signal level

is modeled using kernel density estimator. The fade exceedance probability distributions of signal level are thus determined. The outage probabilities from measured signal level and ITU-R P530-16 for measured radio climatological parameters are also compared.

While the International Telecommunications Union (ITU-R) recommends rain attenuation models based on measured rainfall and radio propagation data, the propagation model in Ethiopian context remains unstudied. This work thus addresses the following: the derivation of one-minute rain rate distribution using the Rice-Holmberg (R-H) model, and then proposing the rainfall rate conversion factors for Ethiopian sites from 15-minute to 1-minute integration time; the development of rainfall rate and fade margin contour maps for Ethiopia; and modelling rain attenuation using the ITU-R method.

Using a semi-Markovian model, the transition probability matrices are established for the four rain regimes namely: drizzle, widespread, shower and thunderstorm. The sojourn time of spikes in every regime is found to be appropriately described by Erlang-k distribution. The proposed Markov chain model uses the transition probability matrix, state vector, and sojourn time distributions for characterization and generation of rainfall events. The number of spikes of generated rainfall events and the corresponding sojourn times follow the power-law relationship. Further, by applying the queueing theory approach the service time, inter-arrival time, and overlap time of spikes are modelled. The result obtained using this approach are consistent with earlier queue results of subtropical and tropical regions, where rain queues exhibit the $M/E_k/s$ queue discipline in microwave and millimeteric spectrum.

Contents

List of Figures

List of Tables

Chapter 1

Introduction

1.1 Introduction

The enormous clamour for high speed, reliable and seamless connectivity of high capacity, wireless communication systems has motivated researchers, communication engineers and network designers to investigate communication systems that operate at microwave and millimetric wave bands. This is because of the crowding of the lower frequency spectrum and increasing demand for large bandwidth and high channel capacity to accommodate ever-growing customer services. However, the trustworthiness of radio communication systems at the higher operation frequency spectrum can be affected by various atmospheric elements such as rainfall, temperature, pressure, humidity and gases [1, 2, 6]. From the atmospheric ingredients, rainfall is the major cause of impairment at higher frequency bands bringing about scattering, attenuation and depolarization of signals at the receiver [7, 8]. In addition to rain, multipath fading is also a main cause of propagation degradation of radio wave transmission [9]. Typically, 99.99% service availability in the worst month is the design objective of radio networks, which implies the network outage should not exceed 53 minutes in a year [10].

Atmospheric factors such as relative humidity, pressure and temperature are variable in time and space producing geo-climatic factor variations, These geo-climatic variations bend electromagnetic wave propagation in various directions over the curvature of the earth causing clear-air multipath fading [11, 12]. Clear-air fading can be described from signal level measurements or from radio climatological parameters. ITU-R Recommendations P 530 [13] gives methods for predicting the probability of time exceedance percentage of a fade

margin in the average worst month. It also proposes estimation techniques depending on specific topographical and climatic conditions.

Performance analysis of wireless networks at higher radio frequencies, mainly depends on the assessment of rain attenuation. Rainfall is a stochastic process, that exhibits temporal and spatial variations over radio wave propagation paths, causing rainfall attenuation [5, 14, 15]. The fading due to rain on radio propagation is a common phenomenon at frequencies spectrum above 7 GHz and 10 GHz in tropical equatorial and temperate climates, respectively [16, 17, 18]. Rain attenuation can be characterized from signal level measurements of the radio links or from rainfall rate and raindrop size distributions.

To give insight into this phenomenon, this investigative thesis will attempt to further advance the understanding of radio wave propagation at microwave and millimetric wave bands by addressing two aspects: wireless communications under clear-air and rainy scenarios. Therefore, signal level measurements, rainfall rate distribution and clear-air radio climatological parameters are determined from this perspective for wireless networks in Ethiopia. More interestingly, a detailed study of the rainfall rate series and its influence on the time-varying wave propagation at microwave and millimeteric operating frequencies, are the subjects of this work.

1.2 Problem Formulation

Many authors have conducted research on the prediction of rain fading, as detailed in [5, 13, 19, 20, 21, 22, 23, 24, 25, 26, 27, 28] . Most of these authors proposed models for the prediction of rain attenuation, particularly in circumstances where satisfactory measurements are unavailable. However, due to the stochastic nature of rain process in time and space, it is challenging to get a model that adequately predicts the dynamic behaviour of propagation in a rain [27]. Yet, there is need for precise propagation estimation due to the fact that over-prediction results in costly over-design, whereas, under-prediction can result in unreliability of the systems [29]. Rainfall is a random process that exhibits variations over radio wave propagation paths from place-to-place and time-to-time, causing varying rainfall attenuation [5, 14, 15].

Efforts have been made initially by the ITU-R 837 [4] and then by Crane [30] to classify the world into rain climatic zones to expand the existing propagation data to a broader

range. These models have however, resulted in much inaccuracy in tropical and equatorial regions because of the fact that most of the recorded dataset was developed for temperate zones [18]. In [31] Allnut et al observe that the current ITU-R rain attenuation estimation technique is not as precise for the tropical zone as it has been observed in the temperate zone.

During non-rainy times, the network outage probability mostly depends on clear-air fading phenomenon which can be determined either from signal level measurements or from the atmospheric parameters such as radio refractivity gradient and the Geo-climatic factor. Therefore, statistical determination of clear-air atmospheric refractivity and refractivity gradient are parameters of interest in radio link design under clear air conditions [32, 33].

In the past 13 years, research efforts on attenuation in Durban, South Africa have come out with exciting results on rain fading and clear-air attenuation over radio propagation paths [34, 35, 36, 37, 38, 39, 40]. Indeed, a thorough investigation into the stochastic features of rainfall is vital in proposing a mitigation technique for dynamic fade cancellation. The probability theory of rainfall, built on stochastic properties, proposes an interesting viewpoint for the modeling and generation of time-varying rainfall events. For instance, Alonge and Afullo propose queueing theory, with a special case of Markovian process to clarify the existence of queues in rainfall process and characterize the rainfall cycle in Durban and Butare, Rwanda [41, 42, 43, 44, 45, 46, 47, 48]. In this work, a more general approach is adopted, where transition probability matrices and sojourn times of rainfall rate spikes (which contribute to rain fade duration) are considered.

Further in this thesis, clear-air radio wave propagation model from signal level measurements and radio-climatological parameters are proposed for the Horn of Africa, particularly in the Ethiopian context. Furthermore, the work also proposes rain attenuation model at microwave and millimetre bands for Ethiopia. The research further investigates the characterization and generation of rainfall process from Markovian and queueing theory approach for radio wave links. Generally, this research tries to answer the following queries: what are the appropriate rain attenuation models for the Horn of Africa? What are the satisfactory rain fade depth levels needed to compensate for propagation degradation over radio links at carrier frequency of microwave or millimeter-wave? How are the region's climatological parameters modelled for characterization of clear-air multipath fading to achieve the necessary signal propagation quality? Is the Markov chain model appropriate for character-

ization and generation of time series rainfall process over wireless network in the region?, This research will contribute in enhancing the understanding of the stochastic nature of time-varying rainfall in the tropical Horn of Africa for wireless networks.

1.3 Scope of the Work

The focus of this study encompass the following:

- To investigate the atmospheric effects on electromagnetic radio waves and to model clear-air multipath fading from radio climatological parameters for the Horn Africa, particularly Ethiopia.
- To develop a model that proposes the solution for signal fading under clear-air situations from signal level measurements in Ethiopia.
- To propose rain rate and attenuations distribution models for Ethiopia.
- To investigate the application of the Markov chain model on time series rainfall process over radio wave propagations.
- To compare the Markov model and the queueing theory approach for generation and characterization of rainfall events in Ethiopia.

1.4 Thesis Overview

The overall structure of this thesis is organized into seven chapters. Chapter one presents motivation for the study, literature review of some works related to this thesis, objective of the thesis, problem formulation, scope of the work, original contributions and publications.

Chapter two is a brief review of clear-air radioclimatic effect on radio links, the kernel estimation technique, effects of rainfall on microwave and millimetric wave links, and review of stochastic models for time series rainfall process.

Chapter three presents the results of clear air multipath fading due to radio climatological parameters for different radio links in Ethiopia. Refractivity gradient and point refractivity gradient values are calculated and used for the determination of Geo-climatic factors which are in turn used for fade depth analysis over various regions in Ethiopia.

Chapter four presents rain-rate distributions and conversion methods from 15-minute to one-minute integration times; rain attenuation, contour mapping of rainfall rate and fade margins for Ethiopian radio links.

Chapter five the investigation and modelling of rainfall time series characteristics over microwave and millimmetric wave bands in Ethiopia. The Markov model and queueing theory approaches are used for the generation and analysis of time varying rainfall process.

Chapter six presents an extensive analysis of time varying received signal level measurement over the line of sight link between Addis Ababa and Furi. A Kernel density estimator is used for the analysis of signal level distribution. The signal analysis is imperative in order to determine fade margin of the link at different probability of time exceedance.

Chapter seven gives conclusions and recommendations. In this chapter, precise conclusions of the research achievements are drawn, and future works are suggested.

1.5 Contributions to Knowledge

This thesis has aimed at making substantial contributions to this topic. Some of the significant contributions of this work are highlighted as follows:

- From the different point refractivity gradient values, the Geo-climatic factor K, for the various regions of Ethiopia have been estimated . It is seen that since K depends on time and locations, it is imperative to determine the K value for regions of interest for more precise prediction of multipath fading. Outage probability at different percentages of time exceedance in Ethiopia are obtained.

- The application of the kernel model on time series of the received signal level distribution is a significant contribution essential for the analysis of probability density function of received signal levels. The analysis of different fade depths at various percentage of probability of time exceedance for signal level measurements is vital contribution for the application of network outage prediction.

- Determination of the cumulative probability distribution, proposing the rainfall rate conversion factors for Ethiopian sites from 15-minute to one-minute integration times; developing rain-rate and fade margin contour maps for Ethiopia; and modelling rain attenuation, are also useful contributions for design tools over terrestrial microwave

links.

- The Markov chain model that considers the sojourn time distribution was investigated for the characterization and generation of time series of rainfall events for the locations under study. Analysis of rainfall traffic from this approach is useful to understand the performance of wireless channels under the influence of rain or to deal with rain fade mitigation.

1.6 Publications

The following Conference Proceedings and journal publications are part of this thesis which appear in conference proceedings and accredited journals:

- **F. D. Diba**, T. J. Afullo and A. A. Alonge, "Rainfall Rate and Attenuation Performance Analysis at Microwave and Millimeter Bands for the Design of Terrestrial Line-of-Sight Radio Links in Ethiopia," SAIEE African Research Journal, Vol.107 (3).pp. 177- 186, September 2016.

- **Feyisa D. Diba**, Thomas J. Afullo and Akintunde A. Alonge, "Rainfall Characterization and Generation from Markov Chains for Rain Fade Modeling over Wireless Links in Ethiopia," Submitted to IET Journal of Microwave,Antennas and Propagation, United Kingdom, September 2016.

- **Feyisa D. Diba** and Thomas J. Afullo, "Estimation of Rain Attenuation over Microwave and Millimeter Bands for Terrestrial Radio Links in Ethiopia," Proceeding of 2015 IEEE AFRICON Conference, Addis Ababa, Ethiopia, September 14 - 17 , 2015.

- **Feyisa D. Diba**, Thomas J. Afullo, and Akintunde A. Alonge, "Time Series Rainfall Spike Modelling from Markov Chains and Queueing Theory Approach for Rainfall Attenuation over Terrestrial and Earth-space Radio Wave Propagation in Jimma, Ethiopia," Proceeding of 2016 PIERS Conference, Shanghai, China, August 8- 11 , 2016.

Chapter 2

Literature Review

2.1 Introduction

The basic concept of radio wave propagation goes back to the ground-breaking study of James Clark Maxwell, who developed electromagnetic propagation theory in 1864 that projected the presence of radio waves. Heinrich Hertz confirmed the physical existence of these waves in 1887. The work of Maxwell and Hertz created the field of radio communications. Oliver Lodge used these principles to build the first wireless communication system in 1894, although its transmission distance was limited to 150 meters. In 1897, the entrepreneur, Guglielmo Marconi, succeeded in sending a radio signal from the Isle of Wight to a tugboat 18 miles away, and in 1901, Marconi's wireless system would cross the Atlantic Ocean. These early communication systems used telegraph signals for exchanging information. The first transmission of music and voice was made by Reginald Fessenden in 1906, applying amplitude modulation that circumvented the propagation limitations at low frequencies detected by Hertz.

Electromagnetic wave propagates through environments in which they are attenuated, reflected, scattered, absorbed and diffracted by walls, terrain, buildings, rain, atmospheric gases and other objects. The ultimate information of this propagation can be obtained by solving Maxwell's equations with boundary conditions that express the physical characteristics of these obstructing bodies. Since these calculations are difficult and since the necessary parameters are often not available, approximations have been developed to characterize signal propagation without resorting to Maxwell's equations [49].

Thus there is need for the appropriate knowledge on variations in atmospheric conditions

from place to place, time to time and with height will influence the performance of radio propagation. As such, poorly designed radio networks will experience episodic outages that in turn lead to poor system availability, increase in system latency, and in worst case scenario, total system failure, and thus loss of revenue. Therefore, this chapter will review studies on factors affecting electromagnetic wave propagation in the atmosphere.

2.2 Earth's Atmosphere

The atmosphere is divided into four layers according to temperature as in Figure 2.1: troposphere, stratosphere, mesosphere, and thermosphere. The troposphere will be the main area of interest for this work because of the fact that it is an area of high radio-climatological instability due to its ground proximity and the unfettered effects of the natural environment on wave propagation in its domain. The effects of precipitation on radio wave propagation increase with operating frequencies, particularly for frequencies above 7 and 10 GHz in temperate and tropical zones, respectively [50, 51]. The influences of the troposphere, the region of the atmosphere adjacent to the earth and extending upwards to 10 km and where clouds are formed, on radio wave propagation under precipitation and clear-air are usually dealt with differently. The ionosphere extends from about 50 km to roughly 2000 km above the surface. Due to the radiations from the sun, the ionosphere takes on a stratified character, referred to as the D, E and F layers. The radiations are mainly ultraviolet rays, gamma rays and cosmic particles such as electrons and protons. The D layer is found occasionally at a height of 50 to 100 km in the daytime and is of little importance. The E layer is a relatively permanent layer at about 100 km. During the day the ionic density in this layer is strong and may almost vanish at night due to the recombination of ions. The F layer is also more or less permanent at about 300 km. In the daytime, it divides into F_1 and F_2 layers and is subject to erratic variations. Apart from seasonal variations, sun-spot activity causes further magnetic storms and consequent radio fadeouts [52].

It is the ionised layers high up in the ionised atmosphere and the moist, turbulent layers way down in the lower reaches of the neutral atmosphere which are the principal factors in radio wave propagation. The various regions in the ionosphere act as reflectors or absorbers of radio waves at frequencies below about 30 MHz, and space communications are not possible. As the frequency is increases, the reflection properties of the E and F

layers are reduced and the signal will propagate through. Radio waves above about 30 MHz will propagate through the ionosphere with degradation of varying degrees depending on the frequency, geographic location and time of the day. As the frequency of the wave increases, ionospheric effects become less significant and above about 3 GHz, the ionosphere is essentially transparent to space communications [52, 53].

Figure 2-1: Atmospheric layer [1]

2.3 Clear-Air Radio-Climatic Effects on Radio Wave Propagation

Variations in the atmospheric situations will mainly come from changes in the atmospheric parameters such as temperature, pressure and relative humidity [54]. These parameters are important in defining how signals are affected as they propagate through the atmosphere, particularly under the so called clear-air conditions. These three quantities can be characterized and modelled, in terms of the refractivity gradient, refractive index, effective earth

radius factor and Geo-climatic factor. These effects can be defined in terms of multipath fading, diffraction fading, scintillation and gaseous absorption.

2.3.1 Diffraction Fading

Diffraction fading results from blockage of a terrestrial Line-of-Sight link (LOS) radio wave propagation by obstacles whose dimensions are larger than the wavelength of the radio signal. The extent of the obstruction loss is reliant on the area of the beam blocked in comparison to the total frontal area of the propagation energy and to the diffraction properties of the obstruction [55]. During terrestrial LOS link design and planning, the propagation path assumed to be free of any barriers or at lowest path clearance needed and the value is expressed by Fresnel zones. The first Fresnel zone defines the point where the additional path distance compared with the shortest distance does not exceed $\lambda/2$, ITU- P 530.15 [56].

The extent of wave bending can determine how much electromagnetic waves are interrupted by barriers along the path. The bending is commonly determined from the effective earth radius factor (k-factor). The refractive index of the troposphere, n is given by:

$$n = \frac{c}{v} = \sqrt{\mu\varepsilon} \tag{2.1}$$

where v is the speed of a radio wave in air, c is the velocity of an electromagnetic wave in a vacuum, ε is the relative permittivity of air and μ is the relative permeability of air.

The radio refractive index n is slightly greater than unity, and slowly decreases to unity with increase in altitude. Therefore, a more convenient quantity, the atmospheric refractivity N (N-units) is usually used as given in [8].

In terrestrial LOS radio links, atmospheric elements (temperature, pressure, humidity) vary along the propagation path. Equation (2.2) relates these elements to atmospheric refractivity, where n and N are refractive index and refractivity of the atmosphere respectively and also T (K), P (hpa) are temperature and pressure while e is the water vapor pressure [57, 58].

$$N = (n-1)10^6 = \frac{77.6}{T}[P + 4810\frac{e}{T}] \tag{2.2}$$

$$K = \left[1 + \frac{dN}{dh}/157\right]^{-1} \tag{2.3}$$

where $\frac{dN}{dh}$ is the refractivity gradient.

Water vapour content, atmospheric pressure, and temperature decrease with height in the troposphere. The decrease in water vapour pressure and dry air pressure is often approximated as an exponential function of height [59].

$$N = \ N_s e^{-h/H} \tag{2.4}$$

where h is height above the ground level, H is the applicable scale height and Ns is the surface level refractivity.

Under temperate atmospheric conditions $dN/dh = -40$ N-units/km, which yields k=4/3. In general, over the height range, refractivity profiles can be designated as sub-refractive, super-refractive or ducting, according to the following criteria [58, 59]:

$$Sub - refraction;\ dN/dh > 40\ or\ \frac{4}{3} >\ k > 0 \tag{2.5}$$

$$Super - refraction;\ -157 < dN/dh < 40\ or\ \infty\ > k > \frac{4}{3} \tag{2.6}$$

$$Ducting;\ dN/dh < 157\ or\ -\infty\ < K <> 0 \tag{2.7}$$

An index of refraction that decreases uniformly with altitude resulting in $k = 4/3$ is referred to as standard atmosphere of refraction. Sub-refraction occurs when the gradient is greater than -40 N-units/km and results in an upward bending of waves. This may occur with the formation of fog or as cold air passes over the warm earth. Super-refraction causes the radio waves to refract downward. This may occur when temperature rises or humidity decreases with height or both. An increase with temperature with altitude, called temperature inversion, occurs when the temperature of the earth's surface is significantly less than that of the air. Under ducting conditions, signals are propagated over very long distances due to the waveguide behaviour of the duct.

Refractivity variation beyond 2 km above ground level is negligible, whereupon N decreases almost linearly with increasing height. But since for radio communication and radio broadcasting links we are only interested in towers which are 100 m to 1 km in height, this study focuses on the range of turbulence only ie. 0 - 2 km above ground level.

Table 2.1: Water and ice parameters coefficients that are usable between -20^0 to 50^0

coefficients	For Water	For ice
a	6.1121	6.1115
b	17.502	22.452
c	240.97	272.55

For line-of-sight radio links (VHF-SHF, 0 - 100 m a.g.l.), anomalies in the refractivity gradient variation result in surface ducts, which cause outages in such networks. On the other hand for broadcasting networks, elevated ducts (500 m - 2 km a.g.l.) result in interference, due to extended propagation ranges.

2.3.2 Clear-air Multipath Propagation Fading Prediction

Multipath fading occurs when signals propagating in different paths reach the receiver at different times and angles. A parameter needed for the prediction of terrestrial LOS clear-air multipath fading is the Geo-climatic factor, K. The Geo-climatic factor is determined from point refractivity and refractivity gradient [33]. The refractivity gradient and point refractivity gradient depend on temperature, pressure and humidity for a height less than 65 m above ground level according to ITU-R recommendations [56]. The water vapour pressure, e, is defined by [33]:

$$e = H\frac{e_s}{100} \tag{2.8}$$

where e_s is expressed by the following equation:

$$e_s = a\exp\left(\frac{bt}{t+c}\right) \tag{2.9}$$

Here, H is the relative humidity(%), t is the temperature in ^OC , e_s is the saturation vapour pressure (hPa) at the temperature t and and the coefficients a, b, c, are given in Table 2.1.

For water, the coefficients are usable between -20 to 50^0C with an accuracy of $\pm$ 0.2%, and for the ice they are variable between -50^0 to 0^0C with a precision of $\pm$ 0.2% [56].

Multipath fading occurs due to random changing of atmospheric elements in the troposphere, therefore,use of an appropriate statistical tool is necessary for the prediction of

random fade depth exceedance caused by multipath fading. The ITU-R multipath prediction methods consider operating frequency, path distance, Geo-climatic factor and path inclination. The ITU-R recommends that region-based Geo-climatic factor determination from local dataset is more accurate than the estimation from the ITU-R map [60].

Techniques for predicting the deep-fading range of the multipath fading distribution have been available for several years. The common worst month link unavailability prediction models are Morita [61], Barnett - Vigants [61, 62], Pearson- Doble [63, 64] used in Japan, North America,and the United kingdom, respectively.

Morita and Kakita [65] introduced the power-law relation of multipath fade occurrence probability based on 4 GHz link in Japan. They showed the effect of path length on the number of hours containing Rayleigh fading in the worst season, but it remained unclear how to relate the measured time with fade depth. The probability of occurrence P_R for such fading was given as [62]:

$$P_R = \ kd^{\alpha} \tag{2.10}$$

where d is the path length and k and α are constants. Morita later developed a frequency-dependent empirical formula for P_R, given in [63] as:

$$P_R = \ \left(\frac{f}{4}\right)^{1.2} Qd^{3.5} \tag{2.11}$$

where, Q=2.0x10-6 (over the mountains), 5.1x10-9 (over the plains),f is the frequency in GHz,

$$Q = \ 5.7X10^{-7}\sqrt{\frac{1}{h}} \tag{2.12}$$

(over sea or coastal region) and h is the average path height expressed in meters. Thus the P_R above defines the probability of outage over the hop.

In the Vigant's model (USA), the fade occurrence probability for heavy fading deep months is given by [63] :

$$P = \ C\left(\frac{f}{4}\right) d^3 10^{-5} \tag{2.13}$$

Where, d is the distance in miles, C=4 (over water and Gulf coast), C=1 (average terrain

and climate) and C=0.24 (mountains and dry climate). The equation (2.13) is multiplied by 100 so as to get the occurrence probability as a percentage.

Modified for surface roughness, C in (2.13) becomes:

C =$(2\omega/50)^{-1.3}$, for coastal areas,

C = $(\omega/50)^{-1.3}$, for average climate,

C= $(0.5\omega/50)^{-1.3}$, for dry climate.

The atmosphere is mainly characterized by temperature, pressure, humidity, and vapor pressure [54]. These parameters affect the propagation of electromagnetic waves in the lower part of the atmosphere (troposphere). To quantify this effect, an index named the radio refractive index, n given in (2.1). Thus, the knowledge of the structure of the index n is very important to the design of the communication links. In practice, the change of index n is very low and can be difficult to have an accurate measure of its variation. For this reason, it is preferable to use another index which variation will be appreciable in comparison with the variation of the index n. This index is the refractivity, denoted by N [8]. Geoclimatic factor, K resulted from the variation of refractivity in the lower atmosphere (equation (2.15) . Geoclimatic factor, K takes in to account the variability of the climate and terrain. According to the ITU-R-P-530 recommendation, the Geoclimatic factor is used to determine the worst month outage probability.

The multipath fading distribution for fade margins in the average worst month for planning could be predicted depending on recommendation ITU-R P.530-16 (2015) applying the following steps:

- Calculate the Geo-climatic factor, K;
- Compute the path inclination;
- Estimate the probability percentage of time that a certain fade depth A is exceeded in the average worst month, Pw.

Variation of refractivity gradient with height in the atmosphere results in multipath fading [52], where:

$$\frac{dN_1}{dh} \approx \frac{N_2 - N_1}{h_2 - h_1} \tag{2.14}$$

The Geo-climatic factor is given in [52], where dN_1 is the point refractivity gradient of

the atmosphere in the lowest 65 m not exceeded for 1% of a year, here N_1 and N_2 are radio refractivity values at heights h_1 and h_2 respectively [52]:

$$K = \ 10^{-4.6-0.0027d\mu_1} \tag{2.15}$$

Path inclination ξ_p, given in (2.16) can be calculated from h_e and h_r (m), above sea level and the path length d (km) where h_e and h_r (m) are transmitter and receiver antenna heights, respectively [52]:

$$|\xi_p| = \left| \frac{h_e - h_r}{d} \right| \tag{2.16}$$

The fade depth margin A (dB) at different percentages of outage probability can be determined from the equation below [17]:

$$P_w = \ Kd^{3.1}(1 + |\xi_p|)^{-1.29} f^{0.8} 10^{-0.00089h_L - A/10} \tag{2.17}$$

2.4 Atmospheric Gaseous loss

There are other contributions to atmospheric attenuation which are not dealt with in this study. Gaseous elements of the atmosphere that induce attenuation include oxygen, water vapour and carbon-dioxide. Their presence in the atmosphere results in a form of path loss called atmospheric loss; it is usually of more importance to signal transmission between 2 GHz and 100 GHz frequencies [2]. The attenuation due to gaseous concentration in the atmosphere is proportional to the specific attenuation. On a terrestrial path, this is calculated using methods in ITU-R P.530 [56].

Figure 2-2 shows the contribution of different atmospheric influences at different frequencies . Atmospheric gaseous absorption, especially water vapour and oxygen, like refraction, also vary with altitude, location and path slant angle. Their attenuation contribution can be given by [62]:

$$A = \Upsilon_a d \tag{2.18}$$

where A is the attenuation in dB, Υ_a is the atmospheric specific attenuation in dB/km, and d is the path length in kilometres. The atmospheric specific attenuation given is the

sum of contributions due to water vapour and oxygen, [33]:

$$\Upsilon_a = \Upsilon_o + \Upsilon_w \tag{2.19}$$

where Υ_o and Υ_w are specific attenuations due to oxygen and water vapour respectively. Fog and clouds attenuation is given by [33]:

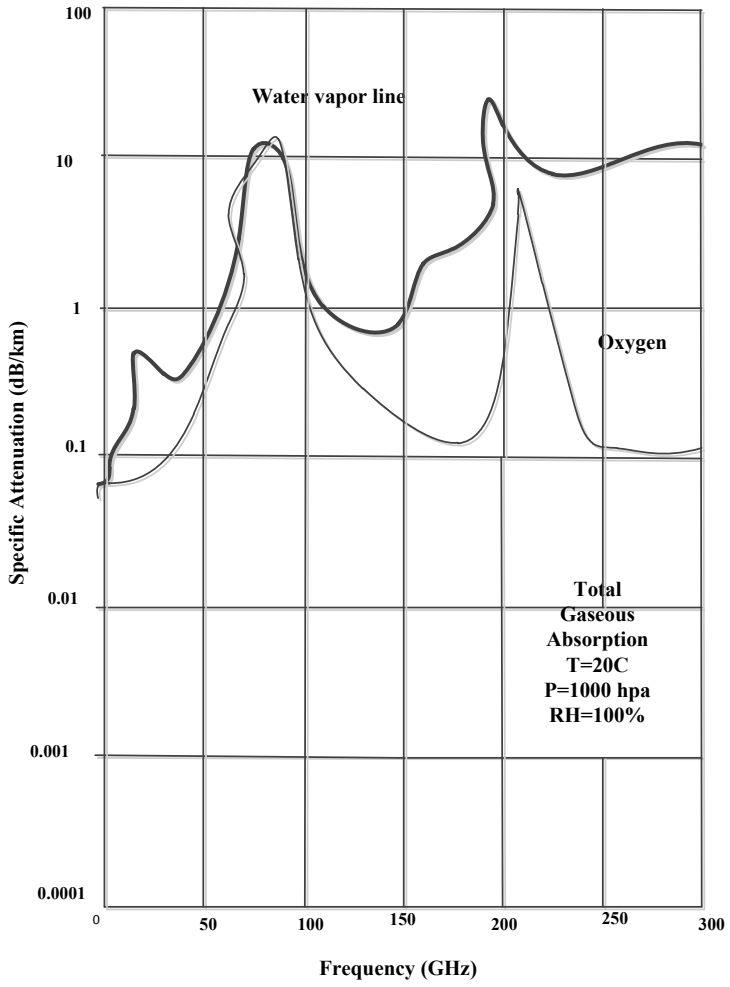

Figure 2-2: Specific attenuation from the effects of water vapour and oxygen at microwave and millimeter wave bands [2]

$$\Upsilon_c = K_l M \tag{2.20}$$

where Υ_c in (dB/km) and K_l (dB/km)/(g/m3) are the specific attenuation and the specific attenuation coeficient of the cloud respectively, and $M(g/m3)$ is the liquid water density of the cloud.

2.5 Terrestrial Link Budget and Link Reliability

Link budget is a mathematical formulation prepared to predict all parameters associated with transmit and receive powers, antenna gains, antenna misalignments, losses and other factors occurring between the transmitter and receiver of the link [8, 33]. The received signal level (RSL) and receiver sensitivity are usually very important parameters for the determination of outage probability. Due to variation of propagation phenomenon, the received signal level varies from time to time resulting in fading as given by:

$$P_r = P_t + G_{tx} + G_{rx} - FSL - L \tag{2.21}$$

Where P_t is the transmitter power output at the Antenna input. This is the amount of microwave carrier output power, usually expressed in dBm; L is losses due to the presence of atmospheric gases, vegetation, buildings, clouds and fogs; G_{tx} = Transmit Antenna gain, G_{rx} = Receive Antenna gain, FSL = Free space path loss.

$$FSL = 92.4 + 20logf + 20logD \tag{2.22}$$

where f is operating frequency in GHz and D is path length in km.

2.5.1 Fade Margin and Link Availability

Fade margin, also called fade depth is calculated by relating the received signal to the receiver sensitivity [33]. The receiver sensitivity is a threshold point below which network outage occurs. The link margin that is related to the outage probability is given in terms of the receiver sensitivity as:

$$L_m = R_p - R_s \tag{2.23}$$

where L_m is the link margin, R_p is received power and R_s receiver sensitivity.

The received power is generally influenced by the characteristics of the transmission medium. In a wireless medium, multipath fading plays a major role. When the reflected

ray arrives at the receiver at the same time with the directed ray, then, they can either add destructively or constructively producing signal attenuation or signal enhancement respectively [33]. Multipath fading, like rain fading, normally produces short-term outages, hence has the highest effect on error performance.

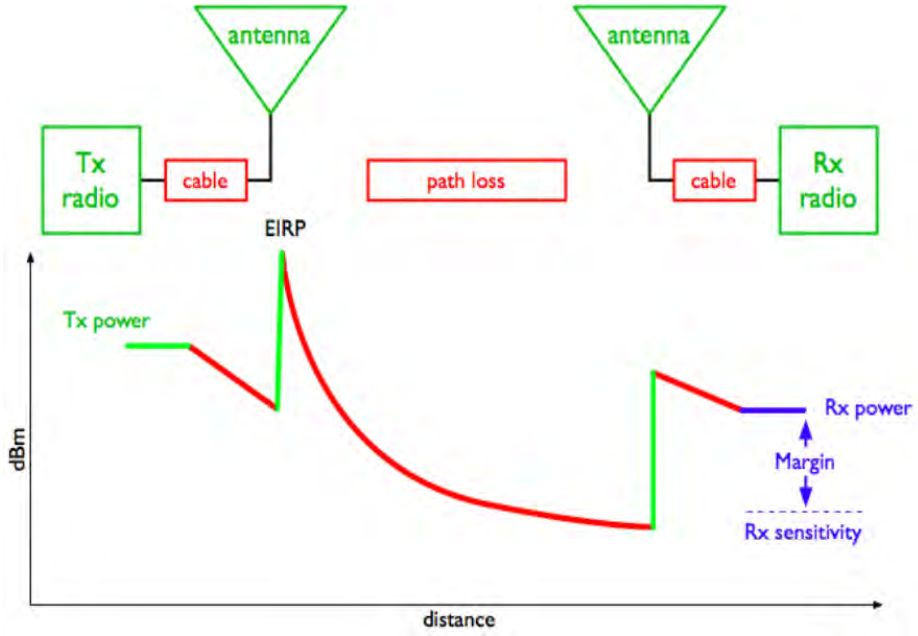

Figure 2-3: Line-of-Sight terrestrial link profile over distance [3]

2.6 Classification of Rainfall Types

Depending on the nature of cloud formation, strength of the rainfall and condensation, meteorologists have classified rainfall rate into two categories: stratiform and convective type of rainfalls [66, 67, 68]. The Stratiform rainfall is made up of small ice particles of the upper troposphere resulting in light drizzle and widespread rainfall type mainly over a large area. They extend up to 1 km across the vertical profile of the isotherm height with rain rates usually less than 10 mm/h [14]. In contrast, convective type of rainfall is produced from strong cumulonimbus clouds which are usually local and reaching up to 100 km/h [66]. Usually they result in shower and thunderstorm types of rainfall, where rainfall rates exceed 10 mm/h. Several researchers, [14, 66, 68] indicated that these types of rainfall are typically common at equatorial and tropical climates.

Furthermore, Adimula and Ajayi [69] classifies rainfall into three types: drizzle, shower

and thunderstorm. In recent rainfall campaigns in Southern African, the four-regime approach of drizzle ($<$ 5 mm/h), widespread (between 5 and 10 mm/h), shower (between 10 and 40 mm/h) and thunderstorm ($\geq 40mm/h$) has also been applied to classify rainfall [70, 71].

2.7 Rainfall Rate Integration Time

During the design, planning and implementation of terrestrial and satellite links, adequate information on rain attenuation due to rainfall is essential for the site under consideration. Rain attenuation can be predicted by collecting and analysing data over a period of time[72, 73, 74, 75]. There is a universal agreement that for accurate prediction of rainfall attenuation, rain data with lower sampling time is crucial. Consequently, recorded rainfall data at one minute or lower integration time can be applied for effective radio links design. Accordance to ITU-R [56], prediction of rain attenuation requires rainfall rate at integration time of one minute. However, one-minute integration time rain data is scarce in many regions of the world. Because of this fact, radio system engineers and designers predict rainfall attenuation using converted rainfall rate from the higher integration times available in the rainfall dataset to the ITU-R recommended one-minute integration time.

There are several methods of rainfall rate conversion developed by researchers [76, 77]. Some of the methods are dependent on regional factors. Emiliani et al. [72] divided rainfall rate conversion techniques into three: empirical, physical and analytical. ITU-R P 837.5 [4], Flavin [78] and Segal [79] employ an empirical conversion technique depending on power-law relationship. This method was used by Ajayi and Ofoche [80] to convert rainfall rate in many locations of Nigeria. Afullo and Owolawi [81] developed rainfall rate contour maps for South Africa's locations for 5-minute to one-minute integration times and this study buttressed the earlier investigations in [7]. Fashuyi et al [82], using 60-minute and one-minute integration time for Durban, developed conversion factors that could be applied by other sites in South Africa to convert their 60-minute data to their equivalent one-minute data. Similarly Owolawi, [81] developed different rainfall rate conversion methods of Hybrid, Linear, Power and Polynomial functions for conversion of 5-minute data to one-minute integration time for over 21 South African sites. .

Segal developed a model for converting rain intensity data from integration time of

minutes to equivalent one-minute rainfall rates, as given by [83]:

$$\rho_\tau(p) = \frac{R_1(P)}{R_\tau(P)} \tag{2.24}$$

where R_τ and R_1 are the rainfall rates with equal probability of exceedence P, of the two integration times [83]. The conversion factor (P) is also given by the power law [80, 84]:

$$\rho_\tau(p) = aP^b \tag{2.25}$$

The physical method uses climate elements such as average rainfall rate , annual and monthly accumulation of rainfall. The Rice-Holmberg (R-H) Model [85] is a physical method depending on the statistical mode of two rainfall types: convective and stratiform rains. The accumulation (M) is the sum of the thunderstorm accumulation (M_1) and all other types of rain (M_2), where:

$$M = M_1 + M_2 \tag{2.26}$$

The thunderstorm ratio is defined as:

$$\beta = \frac{M_1}{M} \tag{2.27}$$

The number of hours of rain at one-minute periods ($T_1(R)$) for which a surface point rainfall is exceeded is given by [78]:

$$T_1(R) = M(0.03\beta exp(-0.03R) + 0.2(1-\beta)[exp(-0.258R) + 1.86exp(-1.63R)] \tag{2.28}$$

2.8 Rainfall Rate distribution Models

Rainfall is a time-varying random process varying over different locations of the world [13]. The statistical distribution of rainfall rate is used to understand its effect on radio wave propagation. The important parameter for rain attenuation is $R_{0.01}$ obtained from cumulative distribution of rainfall rate at 0.01%of time exceedance.

2.8.1 ITU- R Global Rain Rate Zoning

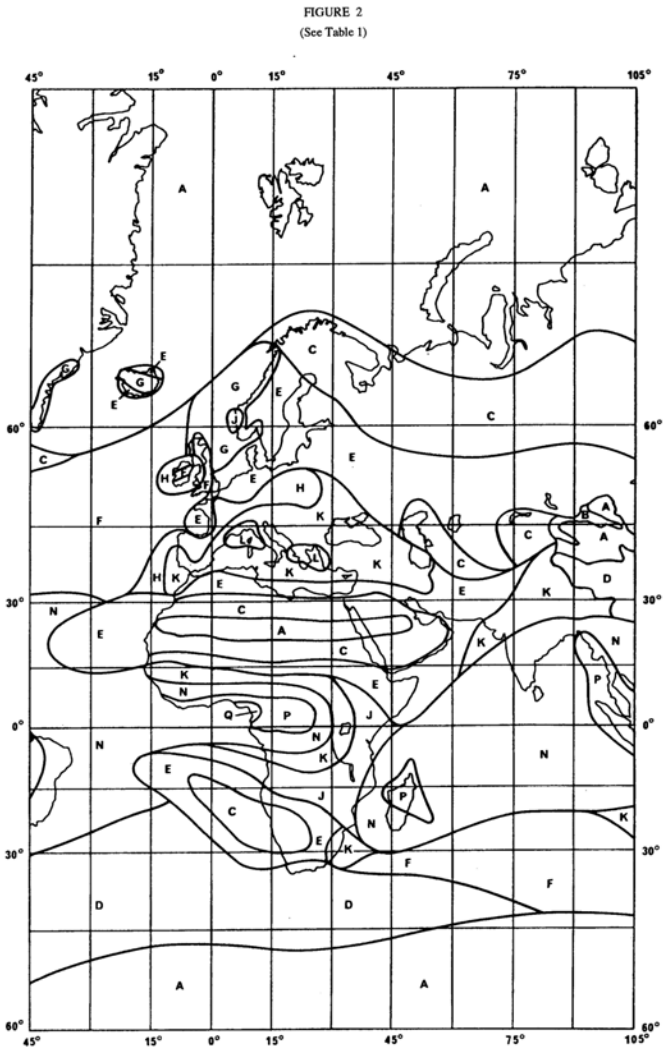

Figure 2-4: ITU-R rainfall map for Europe and Africa [4]

ITU-R P 837 developed zones of global rainfall rate depending on experimental measurements from various areas of the world [4].It classified the globe into 15 rainfall climate zones at different percentages of time exceedance. Accordingly, the important parameters for the

Table 2.2: Average monthly variation of refractivity for three years

Percentage of time	A	B	C	D	E	F	G	H	J	K	L	M	N	P	Q
1.0	< 0.1	0.5	0.7	2.1	0.6	1.7	3	2	8	1.5	2	4	5	12	24
0.3	0.8	2	2.8	4.5	2.4	4.5	7	4	13	4.2	7	11	15	34	49
0.1	< 2	3	5	8	6	8	12	10	20	12	15	22	35	65	72
0.03	5	6	9	13	12	15	20	18	28	23	33	40	65	105	96
0.01	8	12	15	19	22	28	30	32	35	42	60	63	95	145	115
0.003	14	21	26	29	41	54	45	55	45	70	105	95	140	200	142
0.001	22	32	42	42	70	78	65	83	55	100	150	120	180	250	170

determination of rainfall rate for the location under consideration at any percentage of exceedance are longitude and latitude. Using ITU-R P 837-1 recommendation, Ethiopia has four rainfall climate zones namely, C, D, E, and J, as observed in the Figure 2.4. However, the ITU-R classifications are not necessarily sufficient designations [13]. From this work, the rainfall rate values at different percentages of time for various locations of Ethiopia do not correspond to ITU-R classifications.

2.8.2 Crane's Global Rain Rate Zoning

Crane [30] categorized the earth into eight zones, designated A to H with varying amounts of dryness to wetness. Label H is the tropical wet while A implies arctic dry. Using measured datasets, there were differences in rainfall rate at lower percentages of exceedence that leads to formation of more designations. D zone was then classified into D1- D3, where D1 and D3 stand for driest and wettest seasons respectively. Additionally, the world map gave further designations of B region such as B1 and B2.

Figure 2.5 illustrates Crane's global rainfall climatic map for Europe and Africa, where Ethiopia falls under D region.

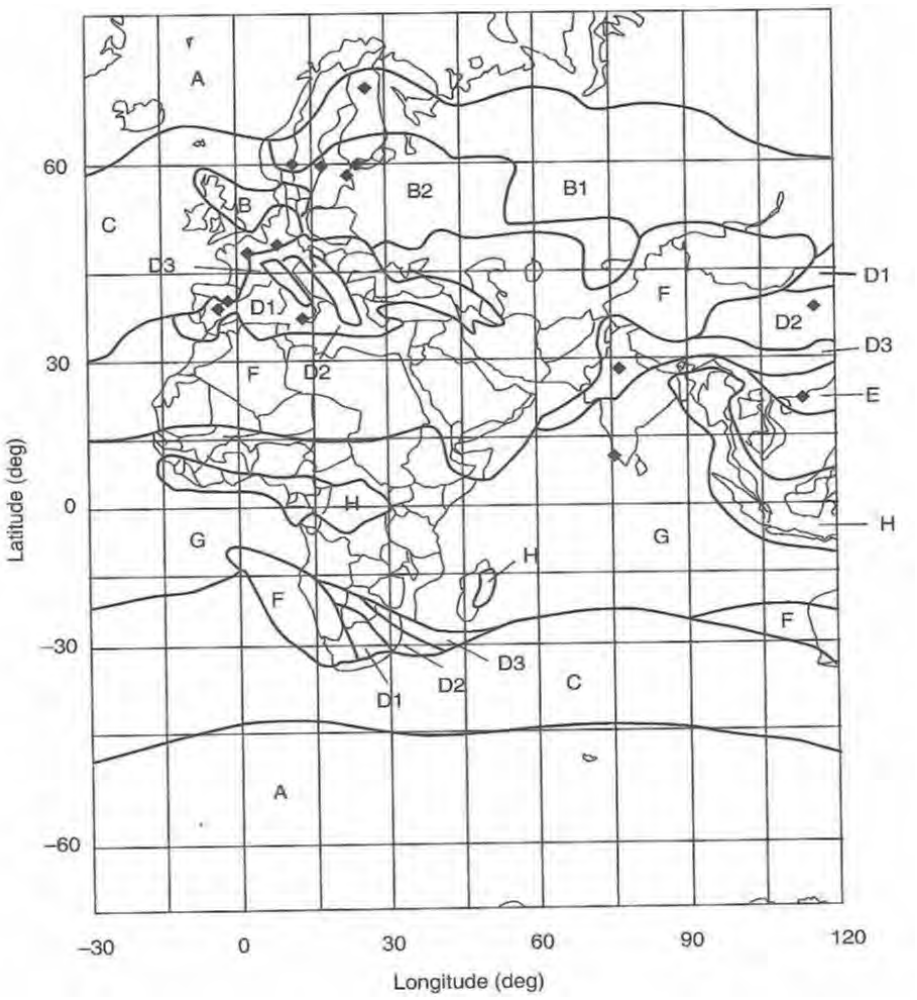

Figure 2-5: Global Crane rain climatic regions for Europe and Africa [5]

2.9 Stochastic Modeling of Time Series Rainfall Rate and Rain Attenuation

A Markov chain is one type of stochastic process named after Andrei Markov who studied the transitions between vowels and consonants in a poem in the early 20th century. In the Markov chain process the probability of the given condition at the present time is possible to be inferred from information about the previous conditions. A Markov chain denotes a system of elements switching from one state to another over time. Many natural processes are reflected as Markov processes [86]. In fact, the transition probability matrix is a tool for characterizing the Markov process. Each element of the matrix denotes probability of

transiting from a specific state to another state.

The understanding of basic probability theory and stochastic process of rainfall is crucial to applying Markov chains on rainfall attenuation studies. Alasseur et al. generated two-level rain rate samples using the Markov model based on its previous time series [87]. First level is two sates i.e rain event and no-rain events. The second level is N-state Markov chain that considers rain rate intensities from previous time samples. The models produce good statistical agreements between simulated rain samples and experimental dataset.

Recently, the queueing theory approach has become an interesting tool to express the fundamental time-domain characteristics of rainfall rate by analyzing rain spikes as a generating queueing process [42, 88, 89]. In that approach, queueing schemes are a representation of processes where activities within a stated period of time keep fractal properties with self-similar behaviour [87, 90, 91, 92]. Alonge and Afullo [93, 94], proposed a well-defined queuing arrangement of a rainfall process by determining the queue parameters such as service time, inter-arrival time and overlap time for Durban (subtropical), South Africa and Butare (equatorial), Rwanda from distrometer measurements. These two sites are places of intense rainfall where the rainfall fading is significant over terrestrial and earth space communication systems operating at microwave and millimetre bands. The rainfall rate spike service time represents the total duration of a spike in a rainfall event, the inter-arrival time is the time difference between the arrivals of two consecutive spikes and the overlap time is the intercept time between starting and stopping of two successive spikes [93, 94].

2.10 Chapter Summary

In this chapter, clear-air multipath fading, diffraction fading, rainfall attenuation and other atmospheric gaseous effect on wireless links have been presented. The stochastic process of rainfall have also been discussed. Generally, rainfall fading is the main cause of communication impairment at microwave and millimeteric wave bands. The next chapter will discuss clear-air multipath fading from radio climatological parameters.

Chapter 3

Prediction of Clear-Air Multipath Fading Due to Radio Climatological Parameters for Microwave Links in Ethiopia

3.1 Introduction

Wireless communications operating at microwave and millimeteric frequencies are getting vast interest due to their high capacity for transmitting voice,video and high bandwidth data [95, 10] . Over wireless networks, atmospheric elements such as humidity, temperature and pressure are not uniform due to the variation of refractivity index along the propagation path [13, 29, 55, 96, 97]. Radio wave transmission in the troposphere is affected by attenuation due to diffraction fading, multipath fading, rain attenuation and atmospheric gasses, [98]. Under clear-air, LOS radio propagation, multipath fading is a major cause of impairment. Multipath fading occurs when the same signal travels along numerous paths and reaches the receiver at different times. Planning of terrestrial LOS radio link design for typical wireless networks considers the transmitter,the receiver the terrain and atmosphere surrounding the links. The path length,frequency of operation, Geo-climatic factor, and the elevations of transmitter and receiver, are very important parameters for the determination of clear-air multipath fading.

Prediction of climatological effects on electromagnetic wave propagations may be done for the average worst month [61]. The International Telecommunication Union (ITU), through Recommendation P 530-15 [13], provides basic LOS link design assumptions based on propagation prediction methods which are not suitable for tropical regions. It is, therefore, imperative that for these regions, experimentally determined parameters are obtained to modify or refine these propagation prediction methods.

In this chapter, the refractivity and refractivity gradient are calculated using three year atmospheric data obtained from National Meteorological Agency (NMA) of Ethiopia. Point refractivity which is not exceeded for 1% of the time, at 100 m above the ground level, is estimated for four sites in Ethiopia: Addis Ababa ($9.01^0N, 38.44^0E$), Diredawa ($9.35^0N, 4151^0E$ Jimma ($7.34^0N, 34.3^0E$), and Mekele ($13.29^0N, 39.28^0E$). The Geo-climatic factor K is calculated from the point refractivity using ITU-R P 530-15 [13] model for the four locations, as well as the probability that a fade depth occurs. In addition, outage probability is determined for the four sites based on the above Geo-climatic factors for the corresponding worst months of the regions, frequency of operations, and link distances.

3.2 Mathematical Methods

3.2.1 ITU-R Model for Clear-air Radio Wave Propagation

In wireless links at higher carrier frequencies, atmospheric elements (temperature, pressure, humidity) vary along the propagation path. These elements can be related to atmospheric refractivity N as from (3.1), where n and N are refractive index and refractivity of the atmosphere respectively and also T (K), P (hpa) are temperature and pressure while e is the water vapor pressure [8, 99].

$$N = (n-1)10^6 = \frac{77.6}{T}[P + 4810\frac{e}{T}] \tag{3.1}$$

for air temperature t (^0C) and relative humidity $H(\%)$, the water vapour pressure,e is by [100]:

$$e = \frac{6.1121H}{100} exp\left(\frac{17.502t}{t + 240.97}\right) \tag{3.2}$$

Variation of refractive gradient with height in the atmosphere results in multipath fading [101], where:

$$\frac{dN}{dh} = \frac{N_2 - N_1}{h_2 - h_1} \cong \Delta N_1 \tag{3.3}$$

If h_1 and h_2 are in the lowest 100 m above the ground level.

The Geo-climatic factor given in [10], where dN_1 is the point refractivity gradient of the atmosphere in the lowest 100 m not exceeded for 1 % of a year:

$$K = 10^{-4.6-0.0027dN_1} \tag{3.4}$$

The path inclination (ξ_p), is given in (3.5) can be calculated from h_e and h_r (m), above sea level and the path length d (km) where h_e and h_r are transmitter and receiver antenna heights respectively [13]:

$$|\xi_p| = \left| \frac{h_e - h_r}{d} \right| \tag{3.5}$$

The fade depth margin A (dB) at different percentages of outage probability, is calculated as [55].

$$P_w = \ Kd^{3.1}(1 + |\xi_p|)^{-1.29} f^{0.8} 10^{-0.00089h_L - A/10} \tag{3.6}$$

3.3 Experiments and Data Processing

Radio-climatic data used in this study was obtained from Ethiopian National Meteorological Agency (NMA), recorded over a period of three years (2013 - 2016). The raw data has primary parameters of pressure, temperature and humidity. Processing the primary data resulted in secondary parameters of: refractivity gradient, point refractivity gradient and Geo-climatic factors. From these parameters fade depth, outage probability and multipath fading distribution are estimated.

3.4 Results and Discussions

Under clear-air conditions, terrestrial LOS link design,planning and performance analysis it is crucial to consider an appropriate fade depth and occurrence probability outage for multipath fading. Determination of multipath fading indirectly depends on atmospheric parameters such as temperature, pressure and relative humidity.

3.4.1 Refractivity, Point Refractivity Gradient and Geo-climatic Factor Analysis

From the recorded average value of relative humidity, temperature and pressure at ground level and at 100 m above ground level using equation (3.1), the refractivity is calculated. The refractivity gradient at 100 m above the ground level is determined using equation (3.3). Then, the Geo-climatic factor for all months of the year is computed using equation (3.4). The results are given in Tables 3.1, 3.2, and 3.3 for refractivity, point refractivity and Geo-climatic factor, respectively, for the four locations considered in study.

From Table 3.1 and Figure 3.1, it is observed that the maximum refractivity values for Addis Ababa, Jimma and Mekele are obtained in August at 270.76, 307.29, and 286.1 respectively. This is due to high water vapour content because of the fact that high rainfall and humidity in August. In Diredawa, the maximum refractivity is recorded in June at 316.47, whereas the minimum values in Diredawa and Jimma are in December because of high temperature in December. The lowest recorded value in Addis Ababa is in February at 237.96 while in May for Mekele at 261.86. Thus, comparing the four sites, Jimma and Diredawa experience higher refractivity values than Mekele and Addis Ababa. This is could be because of lower elevations for the former sites that results in high average values of humidity.

Table 3.1: Average monthly variation of refractivity for between 2013 and 2016

	Refractivity, N-units			
Months	Addis Ababa	Diredawa	Jimma	Mekele
Jan	245.6715	293.61	290.97	268.05
Feb	237.9599	290.21	295.63	269.66
Mar	245.2907	310.28	289.61	270.3
Apr	252.6078	308.76	293.62	269.19
May	256.6403	301.95	297.25	261.86
Jun	258.9719	316.48	302.43	274.67
Jul	270.0154	313.57	288.48	280.95
Aug	270.7572	308.46	307.29	286.11
Sep	265.7492	303.41	300.45	272.47
Oct	248.5699	307.69	298.15	270.14
Nov	245.5126	290.94	298.64	275.41
Dec	239.2466	284.03	285.82	269.86
Oct	248.5699	307.69	298.15	270.14

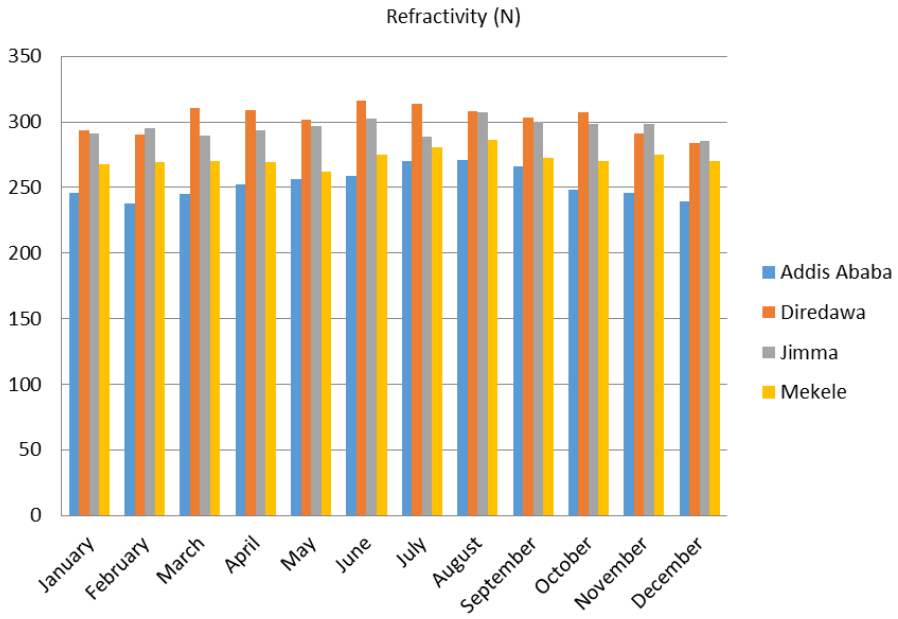

Figure 3-1: Monthly average values of refractivity for four locations

Table 3.2: Average monthly point refractivity gradient variation for three years(2013 - 2016)

	Point Refractivity Gradient,$dN1$			
Months	Addis Ababa	Diredawa	Jimma	Mekele
Jan	-278.20	-660.22	-674.16	-597.22
Feb	-159.56	-626.19	-745.82	-622.06
Mar	-272.34	-826.90	-653.19	-631.78
Apr	-384.92	-811.75	-714.97	-614.79
May	-446.95	-743.63	-770.73	-501.98
Jun	-482.82	-888.83	-850.38	-699.11
Jul	-652.72	-859.81	-635.84	-795.64
Aug	-664.17	-808.75	-925.21	-874.99
Sep	-587.10	-758.23	-820.02	-665.18
Oct	-322.79	-800.99	-784.68	-629.45
Nov	-275.76	-633.51	-792.17	-710.44
Dec	-179.36	-564.45	-595.01	-625.13
Jan	-278.20	-660.22	-674.16	-597.22

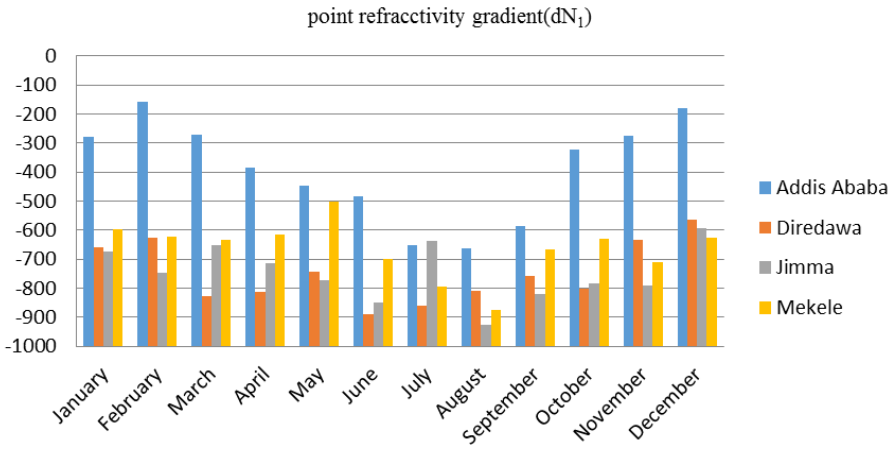

Figure 3-2: Monthly average values of point refractivity gradient at 100 m above ground level not exceeded 1 % of annual average for four sites

Table 3.2 and Figure 3.2 show the monthly variation of average point refractivity gradient,ΔN_1 in the lowest 100 m above the ground not exceeding 1% of the average year for the four locations from three years collected data. It is observed that the worst values of point refractivity gradient occur in August for Addis Ababa, Jimma and Mekele at -664.136, -925.21 and -875 respectively. This is because of high rainfall in the month of August at these different parts of Ethiopia. For Dirredawa the worst month is in June.

Table 3.3: average Geo-climatic factor for different months between 2013 and 2016

	Geo-climatic factor, K			
Months	Addis Ababa	Diredawa	Jimma	Mekele
Jan	0.000141627	0.001523	0.00166	0.001029
Feb	6.77357E-05	0.001232	0.002592	0.001201
Mar	0.000136562	0.004292	0.001457	0.001276
Apr	0.00027496	0.003906	0.00214	0.001148
May	0.000404365	0.002557	0.003027	0.000569
Jun	0.000505385	0.006307	0.004266	0.001939
Jul	0.001453292	0.005266	0.001309	0.003534
Aug	0.001560151	0.003834	0.004308	0.003787
Sep	0.000966368	0.0028	0.004112	0.00157
Oct	0.00018687	0.003653	0.003301	0.001257
Nov	0.000139491	0.00129	0.003458	0.002081
Dec	7.6606E-05	0.000839	0.001015	0.001224

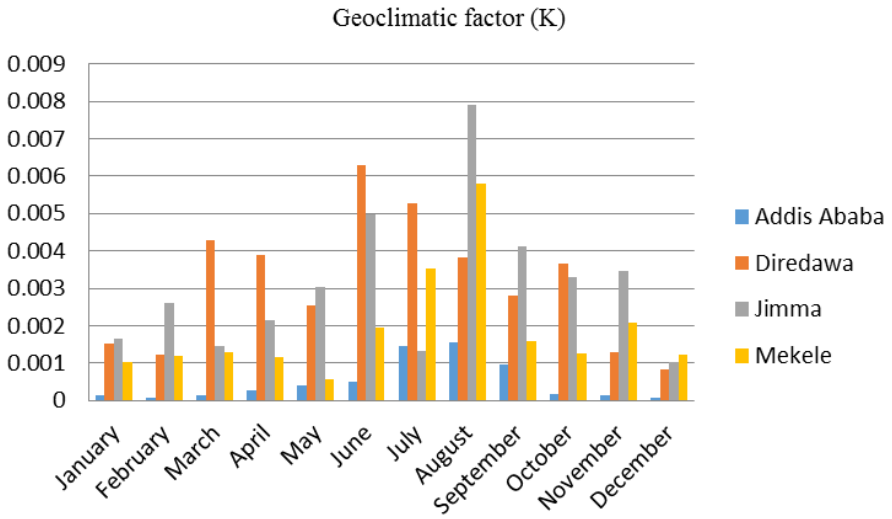

Figure 3-3: Monthly average values of geo-climatic factors for four sites

From Table 3.3 and Figure 3.3, it is seen that the Geo-climatic factor (K) for the worst month (which means the month with the highest value of K) is 0.00156 in the month of August in Addis Ababa. In Diredawa, the highest value of K is 0.006307 in June. In Jimma, the worst month Geo-climatic factor is in August with value of 0.004308. Finally in Mekele, the highest value of K is 0.003787 also in August. In general, for designing LOS radio networks, the important value for propagation planning is the worst month. Therefore,

comparing the four locations the worst month value of K is maximum in Mekele followed by Jimma, Diredawa, and finally, Addis Ababa.

3.4.2 Contour Mapping of Geo-climatic Factor (K) Distribution in Ethiopia

In Table 3.3, the Geo-climatic factors for four locations in Ethiopia are determined from collected meteorological data. However, there is requirement to predict K for all locations in Ethiopia. Applying the spatial interpolation methods, the unknown K values all over the country are predicted. The standard spatial interpolation techniques are: kriging, thin-plate spline, multiqudric, inverse distance weighting (IDW), and bi-linear. From the above spatial interpolation methods, IDW is the easiest and executes best [102, 103] and, therefore, IDW is applied in this work. It considers that close points weigh more to interpolated values than the far observations (this is to say that the influence of known data points are inversely proportional to the distance from the unknown sites that is being predicted). IDW mathematical expression is given by [104]:

$$Z_m = \sum_{i=1}^{n} \omega_n Z_n \tag{3.7}$$

$$\omega_n = \left[\frac{\frac{1}{(d_n)^{\beta}}}{\sum_{n=1}^{N} (\frac{1}{(d_n)}^{\beta})} \right] \tag{3.8}$$

$$\sum_{i=1}^{n} \omega_n = 1 \tag{3.9}$$

$$d_n = \sqrt{(x - x_n)}^2 + (y - y_n)^2 \tag{3.10}$$

Here, Z_m is the predicted value at point m, Z_n is the observed value at the data point n, ω_n is the weight allocated to the sample points, N indicates the number of sample points, d_n is the distance between m and n, β is the power parameter and $(x; y)$ are the coordinates of the interpolation point and $(x_n; y_m)$ are the coordinates of the sample points.

Two types of software are applied, namely, MATLAB and PAST version 2.17C. PAST is an open software package used for statistical data analysis and modelling functions. Spatial interpolation of data was conducted using PAST while contour map plotting was done in

MATLAB. Figure 3.4 presents the proposed worst month Geo-climatic distribution contour map of Ethiopia using the ITU-R model.

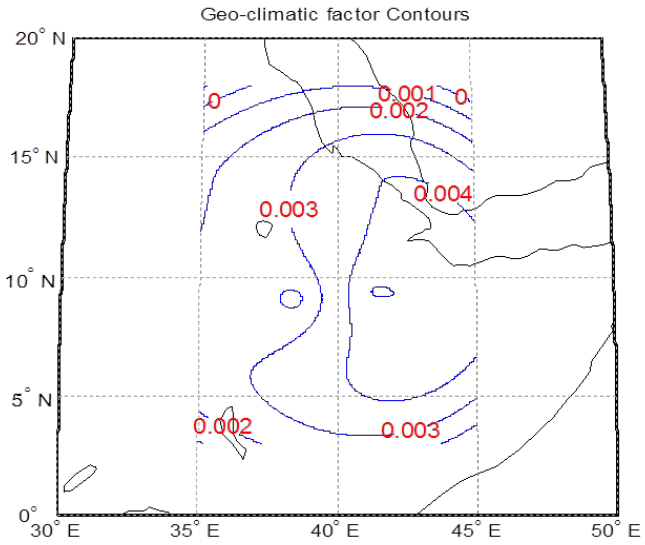

Figure 3-4: Contour map of worst month Geoclimatic factor for Ethiopia

3.4.3 Outage Probability and Fade Depth Analysis using ITU-R Model

Understanding the fading phenomenon is crucial for planning, designing and performance analysis, of wireless networks at microwave and millimeteric bands [12]. In this chapter, design parameters (link distance,frequency, longitude,latitude, elevation, antenna height) of the existing networks are obtained from Ethio-telecom for four LOS links: Addis Diredawa-Kulibi west,Ababa-Furi, Jimma-Mujja, Mosobo-Mekele as seen in Table 3.4. Geo-climatic factor K is computed from (3.4) using the NMA data and path inclination is calculated applying (3.5). Using ITU-R P 530-16 model fade depth and percentage of time of outage probability distribution are calculated.

Figure 3.5 presents the fade depth for various percentages of outage probability for the links in Addis Ababa, Diredawa, Mekele and Jimma using ITU-R P530.16 model. Accordingly, the Diredawa link gives the highest value of fade margin followed by Jimma, Mekele and Addis Ababa.

Table 3.4: Fade depth prediction parameters for four locations

Links	Distance (km)	Frequency (GHz)	Geo-climatic (K)	Path inclination
Addis Ababa-Furi	16.42	11	0.00156	0.024665
Diredawa-Kulubiwest	17.15	11	0.006307	0.01973
Mosobo-Mekele	8.97	6	0.005787	0.05302
Jimma-mujja	13.34	13	0.007908	0.0025952

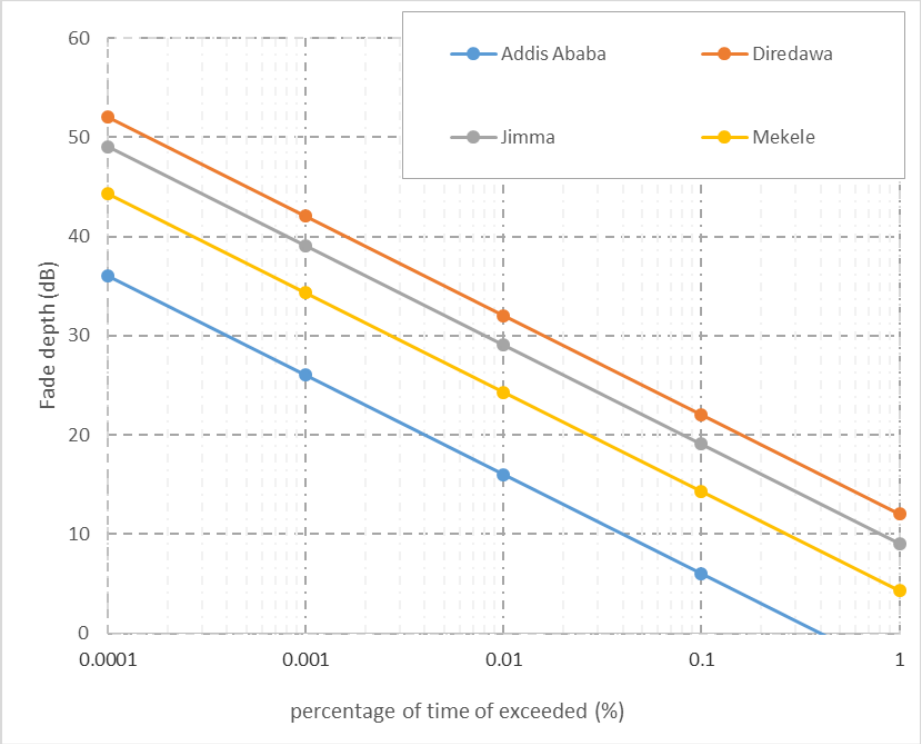

Figure 3-5: Percentage of time fade depth A exceeded in the average worst month for four sites in Ethiopia

Table 3.5: Monthly variations of fade depth (dB) at 0.01% of outage probability for four locations in Ethiopia

Months	Addis Ababa	Diredawa	Jimma	Mekele
Jan	5.59317	25.85042	16.79498	22.26541
Feb	2.389885	24.92952	17.46626	24.20067
Mar	5.435008	30.35001	17.72933	21.69892
Apr	8.474404	29.94074	17.27024	23.36846
May	10.14944	28.10072	14.22195	24.87445
Jun	11.11793	32.02165	19.5466	27.02439
Jul	15.70524	31.23823	22.15349	21.23372
Aug	16.01338	29.85994	24.29536	29.04499
Sep	13.93313	28.495	18.62982	26.20486
Oct	6.797105	29.64991	17.66418	25.25078
Nov	5.527171	25.12931	19.85355	25.45257
Dec	2.924337	23.26104	17.54864	20.12898

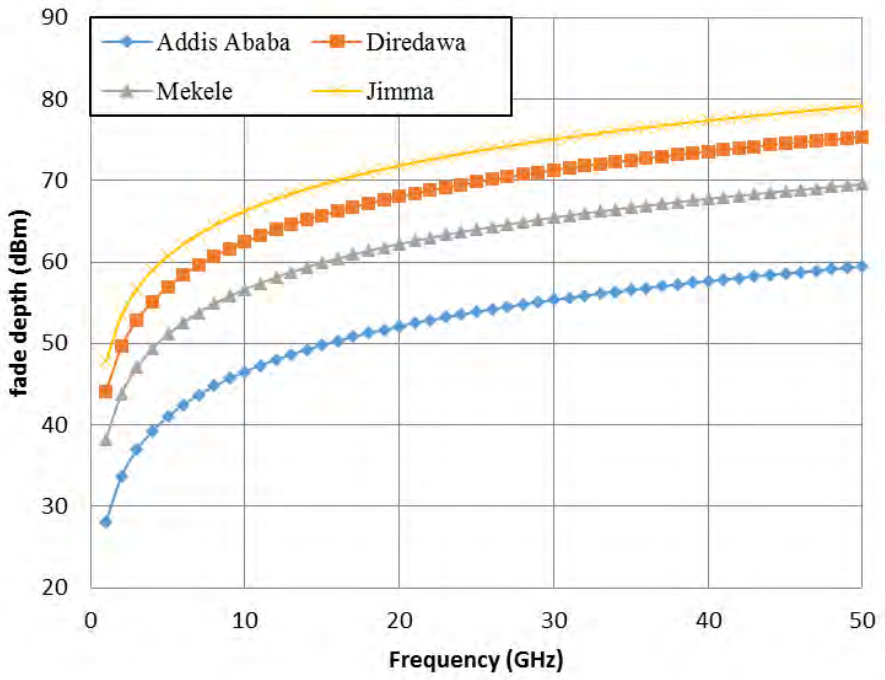

Figure 3-6: Fade depth at 0.01% of time exceedance against varying frequency with fixed link distance

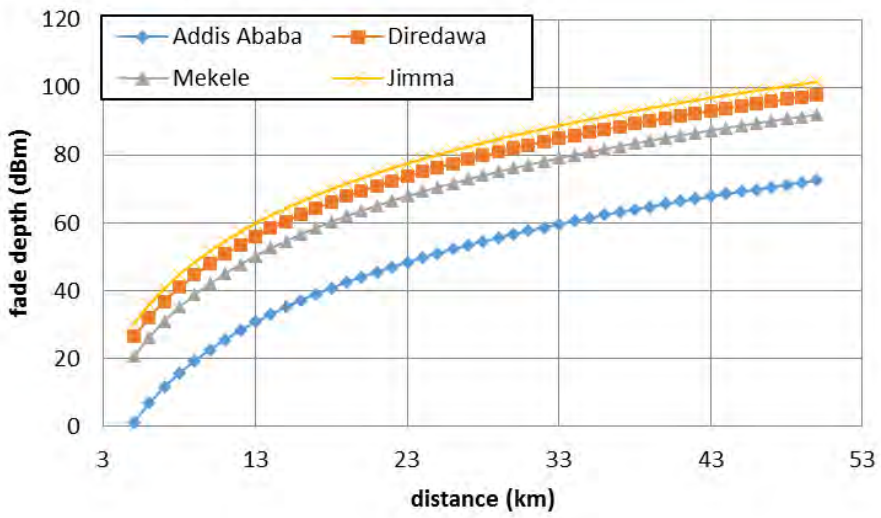

Figure 3-7: Fade depth against different path length at 0.01% outage probability with constant operating frequency for four locations

Table 3.5. shows the fade depth at 0.01% of the time of exceedance for propagation frequencies and hop distance with the link parameters applied for Figure 3.5, for the four sites. It is observed that the fade depth varies monthly and is at maximum in August for Addis Ababa, Jimma and Mekele sites, and in June for Diredawa.

Finally, we determined the fade depth exceeded value for 0.01% of time against frequency and link distances for the four locations using equations (3.6) and parameters from Table 3.4,with the plots given in Figure 3.6 and 3.7. Figure 3.6 presents the fade depth exceeded versus operating frequencies at 0.01% probability of exceedeence with link distances fixed at 16 km. It is observed from the figure that the Addis Ababa link gives the lowest fade depth due to lower Geo-climatic factor value while, Jimma gives high fade depth value mainly due to lower altitude of the link location. Generally, the fade depth increases as operation frequency increase sharply up to 10 GHz then followed by a more gradual increment.

Applying the same link parameters from Table 3.4, Figure 3.7 shows fade depth against varying link distances at probability exceeded for 0.01% of the time. The fade depth variation was determined at a fixed frequency of 11 GHz for link distance varying from 3 km to 50 km. It is observed from the figure that once again Addis Ababa link gives the lowest fade depth due to lower Geo-climatic factor values, while Jimma link gives high fade depth value

mainly due to lower altitude of the link location. It is also seen that fade depth increases with increasing path length.

3.5 Chapter Summary

In this chapter, clear-air multipath fading due to radioclimatological parameters in Ethiopian locations has been examined. The maximum refractivity, point refractivity and Geo-climatic factor in the lowest 100 m above the ground level not exceeding 1% of the average year has been determined for the locations of Addis Ababa, Jimma and Mekele occur in the month of August. From the different values of point refractivity gradient, the Geo-climatic factor, K, for the various regions has been estimated . It is seen that the Geo-climatic factor, which caters for climatic and geographical conditions in multipath fading distribution, varies with the time of the year and locations. The outage probability at different percentage of time exceedance in Ethiopia was obtained for four links using the ITU-R model. In this next chapter, the effect of rainfall distribution on wireless radio propagation over Ethiopia will be discussed.

Chapter 4

Rainfall Rate and Attenuation Performance Analysis at Microwave And Millimeter Bands for the Design of Terrestrial Line-Of-Sight Radio Links in Ethiopia

4.1 Introduction

The fast growth in wireless networks has led to the saturation of the lower frequency bands (1-10 GHz).This reality has shifted emphasis to the higher frequency spectrum, especially in the region 30-100 GHz. However, atmospheric effects, especially rain, are a dominant cause of signal degradation at microwave and millimetre bands, which leads to network outages. Rain attenuation is noticeable from propagation frequencies above 10 GHz in the temperate zone, while in tropical climate its effect is felt from 7 GHz [105]. When a microwave or millimetre wave signal travels through a rainy medium, the signal strength drastically weakens owing to the effect of absorption and scattering by rain drops on its amplitude and phase components [51]. In addition, rain droplets alter the polarization of the transmitted signal, resulting in depolarization effects at the receiver. Thus current microwave transmission network design needs detailed knowledge of rainfall attenuation, depolarization, and fades depth to meet the

quality and reliability specifications for optimum system capacity [106][3]. In practice, the parameters of rainfall rate and raindrop size are investigated to improve the understanding of rainfall effects over wireless communications [107].

The study of radio wave propagation in the microwave and millimetre bands is of immense interest to both the International Telecommunications Union (ITU-R) and the International Union of Radio Science (URSI). The ITU-R, through recommendations P530-15 [13] and P618-11 [108] , provide basic Line-of-Sight (LOS) link design assumptions based on propagation prediction methods which are seldom suitable for tropical regions. It is, therefore, imperative for these regions to determine the parameters experimentally with a view to modifying the ITU-R propagation prediction methods. Many researchers have studied the clear-air and rain effects on radio links in Southern Africa [107, 109, 110, 82, 111, 112], Nigeria [73], and other tropical countries such as Malaysia [113] and Bangladesh [114]. However, many tropical and equatorial African regions have not been adequately studied.

As a case in point there have been no investigative studies on rainfall attenuation effects at microwave and millimetre bands in Ethiopia. In chapter 3, the clear-air radio-climatological parameters effect on radio wave propagation over wireless networks in Ethiopia was investigated. In this chapter,the influence of rainfall on terrestrial line of sight links in different Ethiopian locations is investigated in the following way: 15 minute sampling time rain rate ($R_{15}min$), cumulative distribution is computed, giving the rainfall rate versus the percentage of time the indicated rainfall was exceeded in a year for several regions of Ethiopia based on data obtained from National Meteorological Agency (NMA) of Ethiopia. As one-minute integrated rainfall data is not available for most locations in Ethiopia, the measured rainfall rate was converted from higher integration time (15 minutes in this case) to one-minute integration time, using the Rice-Holmberg (R-H) method [85]. These rainfall rate distributions were developed for ten Ethiopian locations, namaly: Addis Ababa, Adama, Arbaminch, Bahirdar, Diredawa, Dubti, Jimma, Kombolcha, Mekele and Negelle Borenna. Thereafter, a general conversion factor for the rest of the country's locations is proposed. In addition, contour maps for rainfall rate and fade margin are developed and analysed for sites throughout Ethiopia. Based on ITU-R recommendation in [13], the specific rain attenuation for frequency range of 1 - 300 GHz is determined in this thesis. Moreover, path attenuation of rainfall rate versus operation frequencies for different path lengths are estimated. Finally, regarding rainfall attenuation, it is noted that Sami Sharif [115] has done the closest work

over Sudan, bordering western Ethiopia.

4.2 Geography and Climate of Ethiopia

Geographically, Ethiopia is located between latitudes 3^0N to 18^0N, and longitudes 33^0E to 48^0E, with an altitude variation from 100 meters below sea level to over 4000 metres above sea level. It is surrounded by Eritrea to the north, Djibouti to the north-east, Somalia to the east and south-east, Kenya to the south, and Sudan to the west, as shown in Figure 4-1. Ethiopia is generally a country of plateaus, with the Great Rift Valley separating the western and eastern highlands. The highlands slowly slope to the lowlands of Sudan to the west and Somalia to the east.

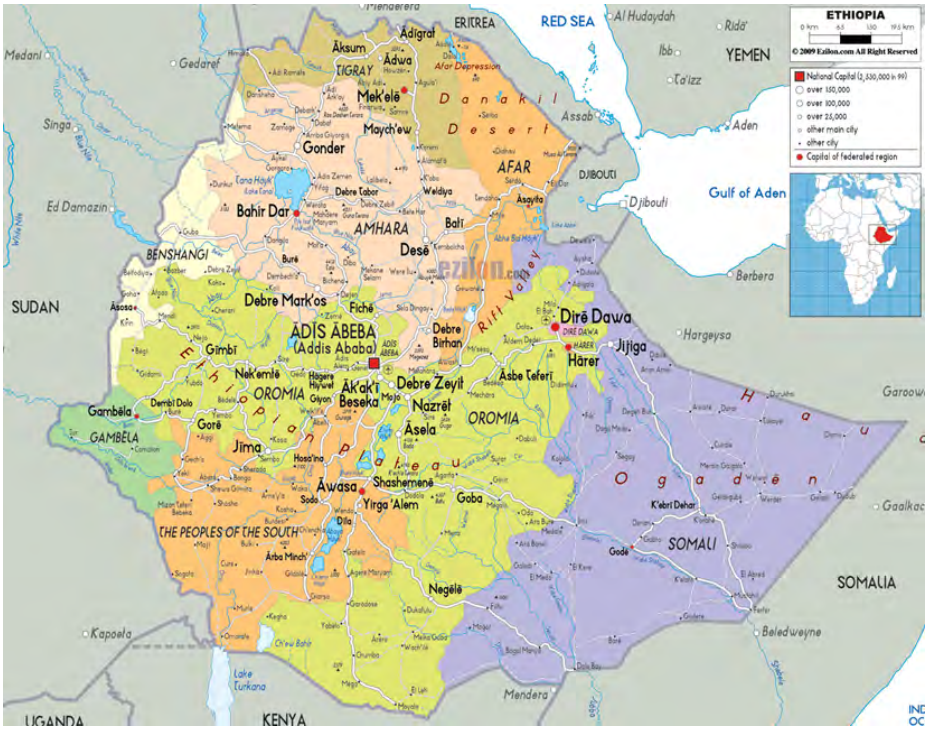

Figure 4-1: Map of Ethiopia

The climate of the Ethiopian highlands is temperate, and of the lowlands is arid [116]. Over Ethiopia, the climatic variations tend to depend on unique features of the area. The classification of the climate by Koppen (proposed in 1931), which is based on geographical elevation, was found useful in this case [117]. Thus, the three main climate classifications in Ethiopia are Class A (As, Aw (tropical), Am) climates of lowlands, varying from semi-

Table 4.1: Locations and their Climate in Ethiopia

Locations	$Lat.(^{O}N)$	$Long.(^{O}E)$	Accum. M(mm)	$KoppenClass$
Addis Ababa	9.02	38.45	1089	Cwb
Adama	8.33	39.17	904.2.46626	Aw
Arbaminch	6.03	37.33	820	Aw
Bahirdar	11.35	37.23	1480	Cwb
DireDawa	9.58	42.32	729.8	BSh
Dubti	11.73	41.08	300	Bwh
Jimma	7.40	36.49	1414	Cfb
Kombolcha	11.09	39.74	1139	Cwb
Negele	5.33	39.58	550	Aw
Mekele	13.28	39.32	601	Bsh

humid to semi-arid surrounds the highlands; Class B (BWh (hot-arid), BSh (hot-semi arid) and BSk) climate in the Afar-Triangle and the Somali Region; and class C (Cwb (warm temperate), Cfb (warm temperate), Cwc) climates in the highlands, ranging from warm to cool mountains with semi-humid to humid characteristics.

4.3 Rain Measurement and Data Processing

The cumulative distribution of rainfall rate (R_p) presents the rain intensity versus percentage of the time (over one year) (p) the indicated rain rate is exceeded. ITU-R [118] requires calculation of $R_{0.01}$ mm/h to predict the attenuation due to rain. $R_{0.01}$ occurs at 0.01% of the time exceedance, which can be read from the ITU-R map [118] or obtained from long-term local measurements. The parameter relies on the integration time of the rainfall measuring devices used. According to [85] and [119], the preferred integration time is one minute. Since one-minute rainfall data is unavailable in Ethiopia, converting from higher integration times to one-minute integration time is therefore required. Therefore Section 4.3.1 covers measurement and data processing; while section 4.3.2 covers 15 minute integration time rainfall distribution.

4.3.1 Rain Measurements and Data Processing

Different devices are available to record rainfall. The NMA of Ethiopia uses two techniques to collect rain data, namely, it applies networks of rain gauges to measure rainfall intensity every 24 hours, and automated rain gauges to record rainfall intensity per 15 minute. The

gauges meet the World Meteorological Organization standards. For the purpose of this chapter, three years raw rainfall data collected by NMA comprising rainy and non-rainy (zero value) days is considered. Only the rain intensities with values different from zero were sorted out and processed, and then the appropriate mathematical formulation was used to calculate the required parameters.

4.3.2 15- Minute Rainfall Rate Distribution in Ethiopia

The cumulative rainfall rate distribution for ten locations in Ethiopia is calculated and plotted based on the data from NMA of Ethiopia at 15 minute integration time. Figure 4-2 shows rain rate distribution for ten main sites of Ethiopia versus percentage of exceedance of time of the year for the 15 minute sampling rate. From Figure 4-2 and Table 4.2 the maximum value of rain rate $R_{0.01}$ (R at 0.01%) is 23.6 mm/h observed at Bahirdar, while the minimum value of $R_{0.01}$ is 8.5 mm/h, recorded at Dubti.

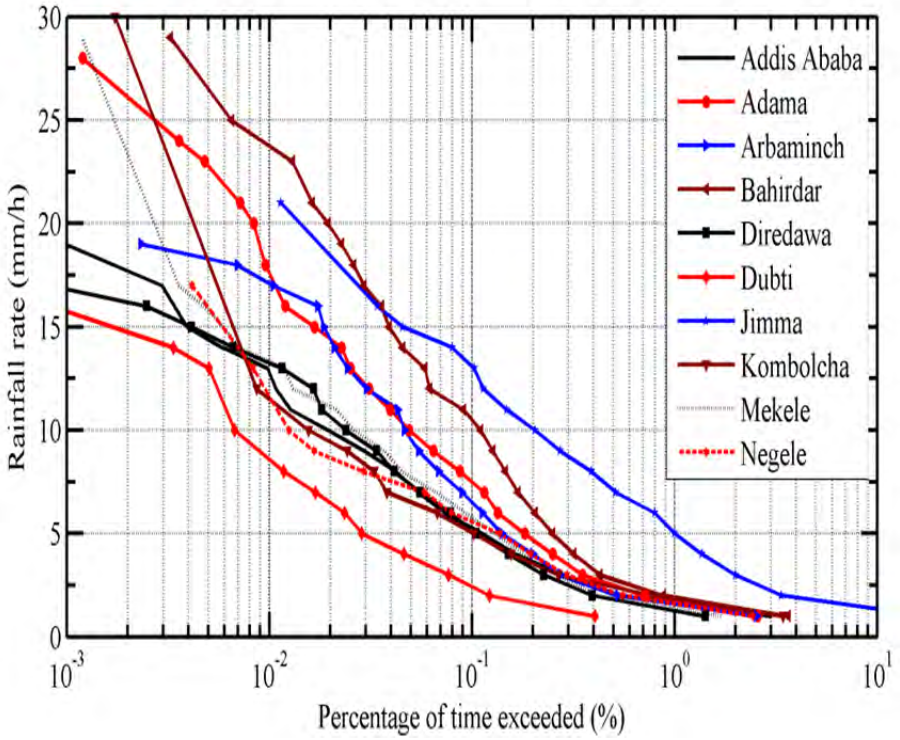

Figure 4-2: Cumulative rain rate distribution at 15 minute sampling rate in Ethiopia

Table 4.2: $R_{15}min(mm/h)$ for 99%, 99.9%,and 99.99% avaliability

Locations	Rain rate 1%	values at 1%,0.1% 0.1%	and 0.01% of time 0.01%
Addis Ababa	1.5	5.5	13
Adama	1.8	7.5	18
Arbaminch	1.7	6.5	17
Bahirdar	2.3	10.5	23.6
DireDawa	1.3	5	13.5
Dubti	0.2	2.5	8.5
Jimma	2.2	13	21.5
Kombolcha	5	11	20.5
Negele	1.3	5.6	11
Mekele	1.4	5.8	13.5

4.3.3 Derivation of One Minute Rainfall Rate Value using Chebil Model

In the absence of comparable one minute rainfall rate data for any of the Ethiopian locations, it is important that only values at 0.01% are compared with one-minute rainfall values from Chebil model [120] and from ITU-R 837.6 [118] From the Chebil's model described in (1), $R_{0.01}$ at 1 minute time is estimated from long term mean annual rain fall (M) using known power low-relationship.

$$R_{0.01} = \alpha M^{\beta} \tag{4.1}$$

α and β are regression coefficients. According to Chebil model, the typical values of regression coefficients α and β for Ethiopian location are 12.2903 and 0.2 respectively as obtained from the map in [85]. This model has been reported to provide better estimation than ITU-R P837.5 in tropical climate [121]. From Figure 4-3, it is found that at 0.01% exceedance or 99.99% availability, the rainfall conversion rates over the investigated Ethiopian locations are given in (4.2) and (4.3) according to ITU-R and Chebil models respectively.

$$R_{1min(0.01)} = 15.781 R_{15min}^{0.4155} \tag{4.2}$$

$$R_{1min(0.01)} = 12.616 R_{15min}^{0.5031} \tag{4.3}$$

The coefficients of determination (R^2) are found to be 0.600 and 0.837 for ITU-R and

Table 4.3: $R_{0.01}$ of ITU-R and Chebil models for different sites

Locations	M (mm)	R0.01-CHEBIL(mm/h)	R0.01- ITU-R (mm/h)
Addis Ababa	1089	57.24	54
Adama	904.2	54.94	56
Arbaminch	820	53.78	50
Bahirdar	1480	61.24	57
DireDawa	729.8	52.42	50
Dubti	300	43.10	45
Jimma	1414	60.63	64
Kombolcha	1139	57.8	48
Negele	550	49.25	48
Mekele	601	50.22	52

Chebil models respectively. This gives a 4 mm/h average difference between the converted values of estimation. These results tend to agree with ITU-R and Chebil models. For future work one minute data are needed to discuss the actual results.

4.4 Modeling of One-minute Rainfall Rate Cumulative Distribution

There are many rain-rate distribution models for one-minute integration time. Some of these models include the Rice-Holmberg (R-H) model [85], the Kitami model [122], the Moupfouma model [123], and the Global ITU-R model [118]. The R-H method is based on the thunderstorm ratio and the average annual precipitation as the two vital components for predicting the rainfall rate from the local rainfall dataset. The components can either be obtained from the predicted number of thunderstorm days or maps presented in [119], the highest monthly rainfall, and the long-term average annual precipitation, The Kitami technique was developed by Ito and Hosoya [122], and it depends on two regional climatic parameters such as the average annual precipitation and the thunderstorm ratio. Moupfouma's methods, proposed by Moupfouma and Martin, provide an easy approach to the estimation of rainfall rate distribution for both tropical and temperate climates. Considering the variability of the rainfall rate estimations, the R-H model has been determined to give a much better performance than others [124].

4.4.1 Rice Holmberg Rainfall Distribution Model

In this work, the Rice-Holmberg model is used to determine one-minute rainfall rate cumulative distribution (CD) from local meteorological data to generate the two main parameters of distribution prediction, which are the average annual accumulated rainfall data (M), and the thunderstorm ratio β. The average rainfall accumulation (M) is the sum of the thunderstorm accumulation (M_1) and all other rain (M_2) [78], where:

$$M = M_1 + M_2 \tag{4.4}$$

The thunderstorm ratio is defined as:

$$\beta = \frac{M_1}{M} \tag{4.5}$$

The number of hours of rain at one-minute periods (T1(R)) for which a surface point rainfall is exceeded is given by [78]:

$$T_1(R) = M(0.03\beta exp(-0.03R) + 0.2(1-\beta)[exp(-0.258R) + 1.86exp(-1.63R)] \tag{4.6}$$

Hence, the percentage of time of an average year during which one-minute average rainfall rates exceed is

$$P(\%) = \frac{T_1(R)}{87.66} \tag{4.7}$$

In this chapter, the parameter M is obtained from rainfall data, whereas β is obtained from the map in [85], which is 0.2 for Ethiopia.

Table 4.4: $R_{15}min(mm/h)$ for 99%, 99.9%,and 99.99% avaliability

Locations	Rain rate values at 0.1%,0.01% and 0.001% of time in a year 0.1% 0.01% 0.001%		
Addis Ababa	14	64	140
Adama	12	60	138
Arbaminch	11.5	58	134
Bahirdar	17	76	155
DireDawa	10.5	53	130
Dubti	8	28	100
Jimma	16	73	152
Kombolcha	13.5	63.5	142
Negele	10	44	120
Mekele	10.2	46.5	123

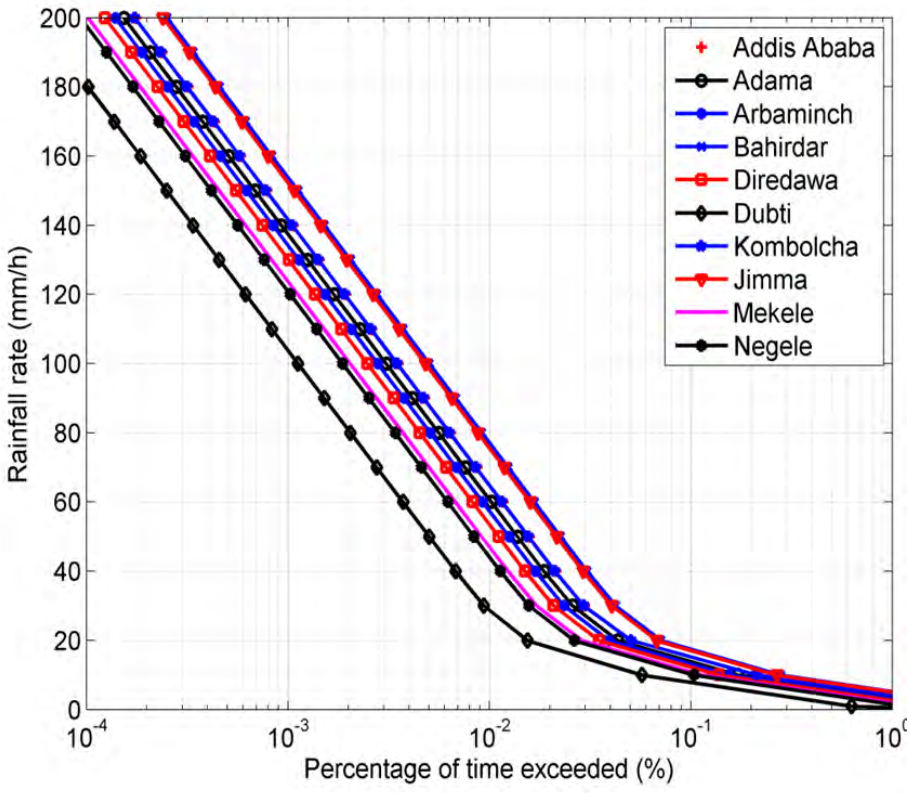

Figure 4-3: R-H rainfall rate cumulative distribution at one minute integration time in Ethiopia

Figure 4-3 shows the calculated R-H one minute integration time of rain rate distribution versus percentage of time exceedance for ten locations in Ethiopia. From the figure, the

maximum rain rate (R) at 0.001%, 0.01%, and 0.1% of exceedance of time is in Bahirdar, while the minimum is recorded in Dubti with the values listed in Table 4.4.

The 15-minute rain intensity data for Ethiopian locations were obtained from the NMA of Ethiopia for a period of three years. The rainfall rate conversion from higher integration time to a smaller integration time has been developed by many researchers [111, 119, 123]. ITU-R P 837.6 also presents the power-law empirical conversion method for some countries and regional maps exist showing regional values for $R_{0.01}$. Flavin and Segal approaches in [78, 83, 84] are also based on power-law conversion methods. Segal developed conversion factors for converting rain intensity data with higher integration time to equivalent one-minute rainfall rates, as given by [83]:

$$\rho_\tau(p) = \frac{R_1(P)}{R_\tau(P)} \tag{4.8}$$

where R_τ and R_1 are the rainfall rates with equal probability of exceedence P, of the two integration times [83]. The conversion factor (P) is also given by the power law [84]:

$$\rho_\tau(p) = aP^b \tag{4.9}$$

where P is the probability of occurrence, and a and b are the regression coefficients derived from the measured rainfall data. From Table 4.5, the general conversion factor for Ethiopia is given by

$$R_1(P)_{=}1.199R_{15}(P)^{1.4805} \tag{4.10}$$

Figure 4-5 shows the conversion factor graph for only two locations (Adama and Jimma) with their corresponding regression and correlation coefficients.

Table 4.5: Values for regression and correlation coefficients for conversion factors

Locations	τ	a	b	R^2
Addis Ababa	1	1.44	1.507	0.945
Adama	1	0.919	1.435	0.991
Arbaminch	1	0.926	1.435	0.962
Bahirdar	1	1.088	1.316	0.976
DireDawa	1	0.906	1.619	0.965
Dubti	1	8.263	0.738	0.817
Jimma	1	1.182	1.593	0.981
Kombolcha	1	1.492	1.441	0.958
Negele	1	1.12	1.245	0.964
Mekele	1	0.964	1.498	0.979

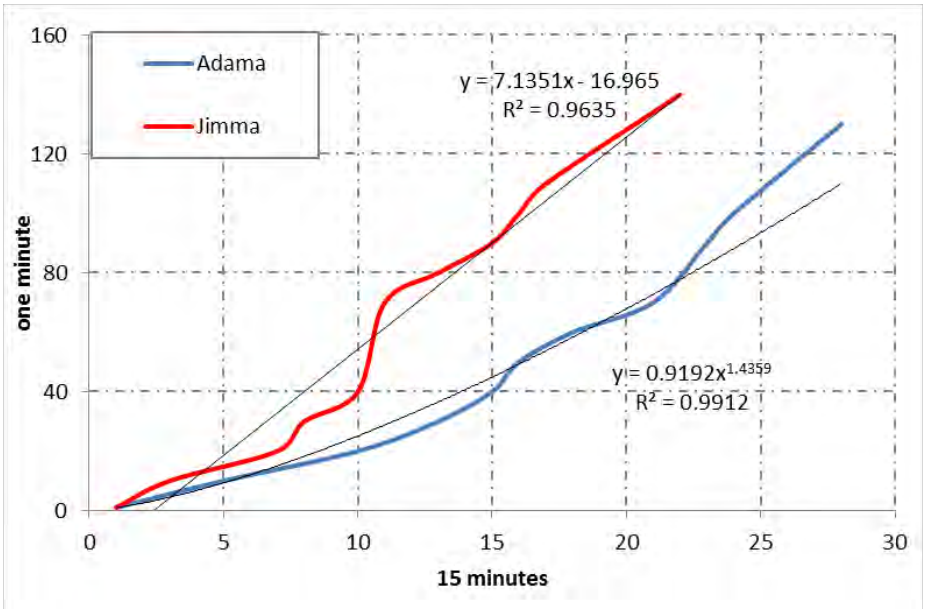

Figure 4-4: 15-minute to 1-minute Rain-rate conversion for Adama and Jimma

4.4.2 Contour Mapping of Rainfall Rate Distribution for Ethiopia

In this study, the rain rates at 0.01% of time exceedance is calculated from available data for ten stations in Ethiopia. However, there is need to determine $R_{0.01}$ for all locations in the country. Using spatial interpolation techniques, unknown points all over Ethiopia are estimated. There are a number of spatial interpolation methods, such as kriging, inverse distance weighting (IDW), thin-plate spline, multiqudric, and bi-linear.

From the above spatial interpolation techniques, IDW is the simplest and performs best

[102, 112] and, thus, IDW is used in this work. IDW considers that the nearby values weight more to the interpolated points than the distance observations (that means the contribution of known data points are inversely proportional to the distance from the unknown location that is being predicted). The IDW expression is given by [104]:

$$Z_m = \sum_{i=1}^{n} \omega_n Z_n \tag{4.11}$$

$$\omega_n = \left[(\frac{1}{(d_n)^\beta}) / \sum_{n=1}^{N} (\frac{1}{(d_n)}^\beta) \right] \tag{4.12}$$

$$\sum_{i=1}^{n} \omega_n = 1 \tag{4.13}$$

$$d_n = \sqrt{(x - x_n)}^2 + (y - y_n)^2 \tag{4.14}$$

Here Z_m is the predicted value at point m, Z_n is the observed value at the data point n, ω_n is the weight allocated to the sample points, N indicates the number of sample points, d_n is the distance between m and n, β is the power parameter and (x; y) are the coordinates of the interpolation point and (xn; ym) are the coordinates of the sample points.

Two different types of software are used, namely, PAST version 2.17C, and MATLAB. PAST is a free software tool and it is a package used for statistical data analysis, plotting and modelling functions. Interpolation of data was done using PAST and plotting of contour maps was carried out in MATLAB. Figure 4-5 shows the proposed rainfall rate distribution contour map of Ethiopia of $R_{0.01}$ using the R-H model. It is seen from the figure that the western and central high lands part of Ethiopia experience higher rainfall rate distribution than the eastern low lands as expected.

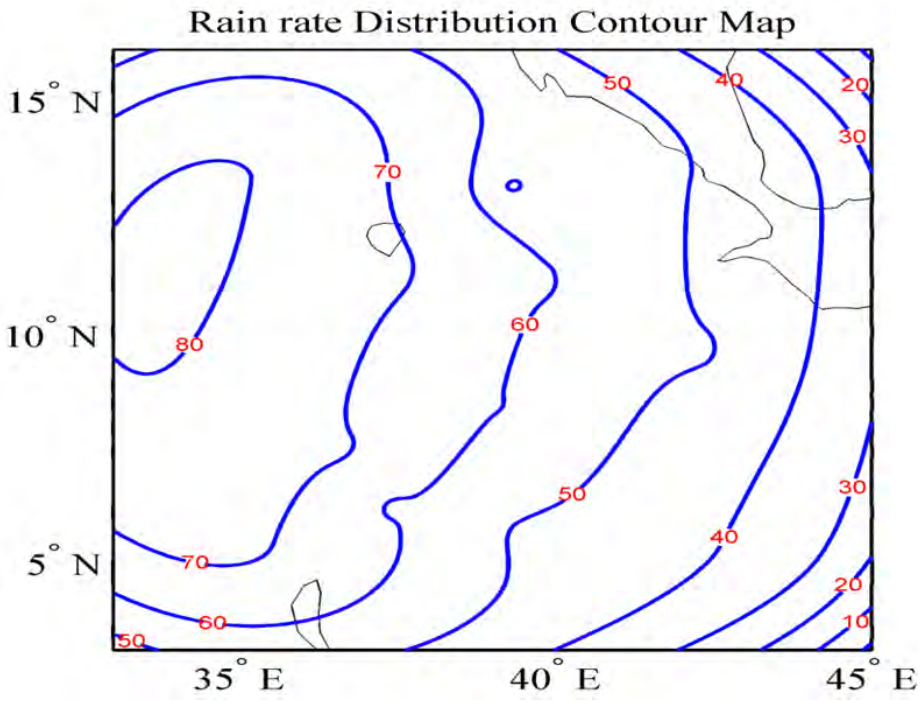

Figure 4-5: Contour map of rain rate using R-H model at 0.01% for Ethiopia

4.5 Determination of Rain Attenuation over Ethiopia

Rainfall that occurs over terrestrial radio links induces attenuation because of the electromagnetic wave scattering and absorption by rain drop particles. In order to characterize rain attenuation, ITU-R (530-15) proposed a rainfall attenuation prediction model. Therefore, Section 4.5.1 discusses the specific attenuation while Section 4.5.2 presents total rain attenuation for varying path length and frequency.

4.5.1 Determination of Specific Rain Attenuation of Rainfall

The attenuation due to rain for terrestrial radio links is based on $R_{0.01}$, signal polarization, propagation frequency, and path length. The first step is to determine the specific rain attenuation - that is, rain attenuation per kilometre in a rainy medium. In this thesis, the value of $R_{0.01}$ is computed using R-H model as shown in Table 3. However, if local data is not available, $R_{0.01}$ can be estimated from the ITU-R map in [118]. The specific attenuation (dB/km) is given by [125]:

$$\Upsilon_R = kR_{0.01}^{\alpha} \tag{4.15}$$

Here Υ_R is specific attenuation, K and α are the regression coefficients which are determined as a function of frequency as given in [125]for horizontal and vertical polarization.

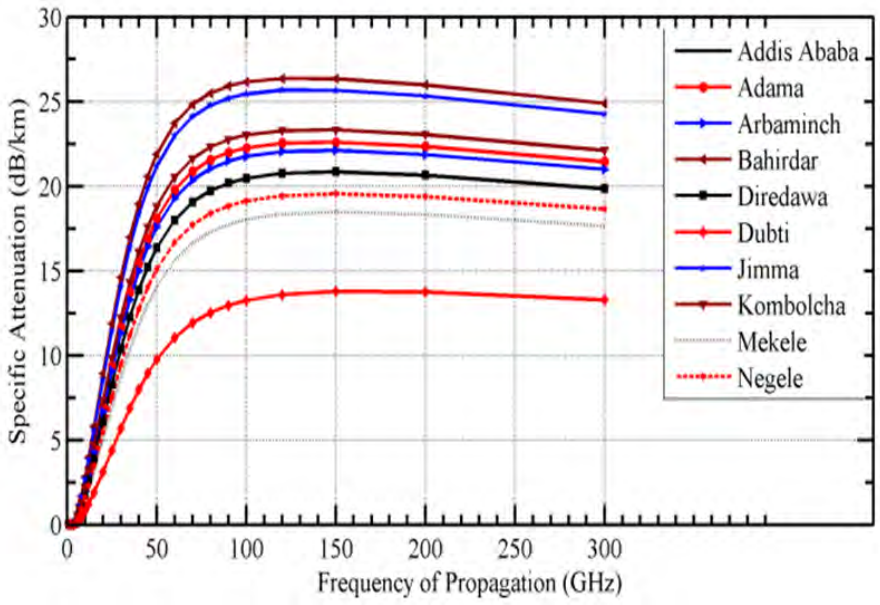

Figure 4-6: Specific rain attenuation for Ethiopia versus frequency for horizontal polarization

Figures 4-6 and 4.7 show the calculated distribution of specific attenuation of rain versus frequency for ten locations in Ethiopia, namely: Addis Ababa, Adama, Arbaminch, Bahirdar, Diredawa, Dubti, Jimma, Kombolcha, Mekele and Negele Borena. In fact, these are typical locations that represent most parts of the country. Figure 4-6 shows the specific rain attenuation for horizontal polarization for the ten locations; while Figure 4-7 is for vertical polarization. Figuger 4-6 shows the fast increase of specific attenuation for frequency ranges up to 50 GHz, then a more gradual increment from 50 to 100 GHz. These values then remain practically constant for frequencies up to 150 GHz. Finally, it slowly decreases for the rest of propagation frequency. It is seen from Figure 4.6 that the maximum specific attenuation of 22 dB is observed in Bahirdar, while the minimum of 10 dB is estimated in Dubti at 50 GHz. From Figure 4.7, the highest specific rain attenuation of 20 dB is observed in Bahirdar, while the lowest (8 dB) is observed in Dubti at the frequency of 50 GHz. From Figure 4-6 and 4-7 it is also seen the specific rain attenuation for horizontal polarization is higher than for

vertical polarization, because of the fact that the raindrops have a non-spherical shape with flattened base and therefore, the horizontally polarized waves are attenuated more than the vertically polarized waves.

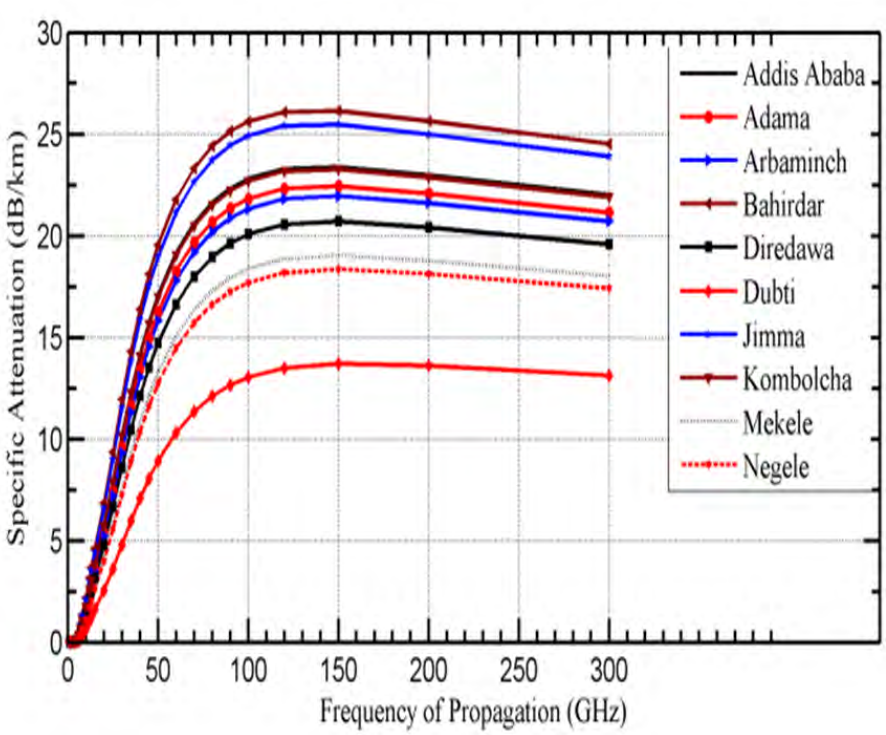

Figure 4-7: Specific rain attenuation for Ethiopia versus frequency for vertical polarization

4.5.2 Determination of Rainfall Attenuation

According to the ITU-R model [5], the prediction of rainfall attenuation involves the following five steps: Step 1: Determination of the rain rate ($R_{0.01}$), as seen in Table 4.4 and Figure 4-3. Step 2: Computation of specific attenuation (dB/km), as given equation (4.15) above. Step 3: Calculation of the effective path length (deff) of the link which can be computed by multiplying the actual path length (d) with the distance factor r, where r is given by [5]:

$$r = \frac{1}{0.477 d^{0.633} R_0.01^{0.073\alpha} f^{0.123} - 10.579(1 - exp(-0.024))} \tag{4.16}$$

where f (GHz) is the frequency and $\alpha$is the exponent in the specific attenuation model from Step 2. Maximum recommended r is 2.5, so if the denominator of equation (4.16) is less than 0.4, use r = 2.5. Step 4: An estimate of the path attenuation exceeded for 0.01%

of the time is given by:

$$A_{0.01} = \Upsilon_R d_{eff} = \Upsilon_R dr \tag{4.17}$$

Step 5: The attenuation exceeded for other percentages of time p in the range 0.001% to 1% may be deduced from the following power law:

$$\frac{A_P}{A_{0.01}} = C_1 P^{-C_2 - C_3 log_{10} P} \tag{4.18}$$

$$C_1 = (0.07^{C_0})[0.12^{1-C_0}] \tag{4.19}$$

$$C_2 = 0.855C_0 + 0.546(1 - C_0) \tag{4.20}$$

$$C_3 = 0.139C_0 + 0.043(1 - C_0) \tag{4.21}$$

where:

$$C_0 = \begin{cases} 0.12 + 0.4[log_{10}(\frac{f}{10})^{0.8}], & f \geq 100GHz \\ 0.12, & otherwise \end{cases} \tag{4.22}$$

The prediction procedure outlined above is considered to be valid in all parts of the world at least for frequencies up to 100 GHz and path lengths up to 60 km [5].

Figures 4-8 and 4-9 show the rain attenuation versus link path length for horizontal and vertical polarizations for ten sites in Ethiopia over different distances. From these graphs, the rain attenuation rises sharply for the first 20 km, then increases less sharply from 20 km to 40 km and finally the attenuation settles almost to a constant. As the distance increases, the rain attenuation becomes non-uniform because of the fact that for large actual path lengths, the effective path length remains fixed. As seen in Figure 4-8 with horizontal polarization at distance of 20 km, the maximum rain attenuation is observed at Bahirdar at 41 dB, while the minimum is at Dubti at 16.2 dB. For vertical polarization (Figure 4-9) similar distribution of rain attenuation is observed: the highest value is 35 dB in Bahirdar, and lowest value is 14.5 dB in Dubti at 20 km. Comparing the two graphs, vertical polarization has lower rain attenuation than horizontal polarization, as already stated.

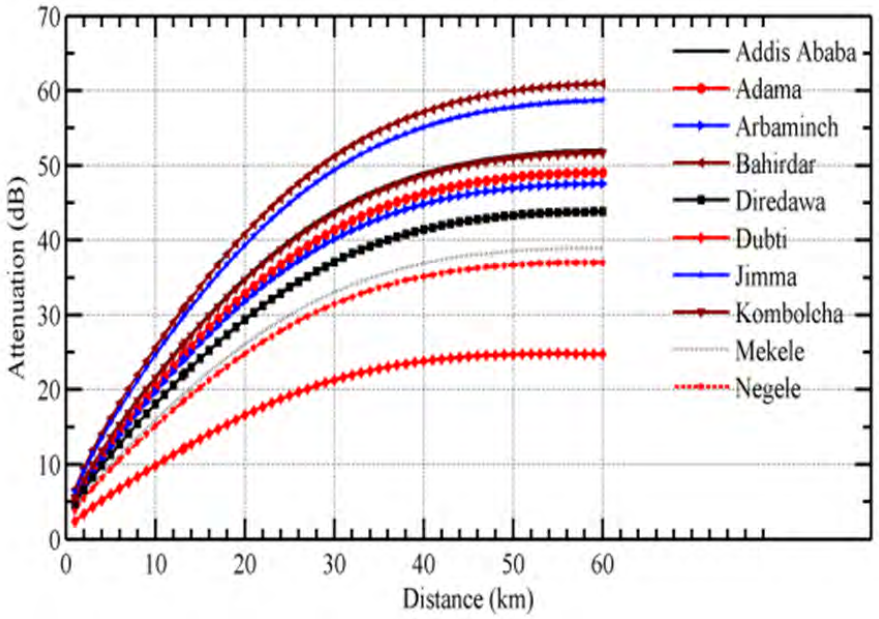

Figure 4-8: Attenuation versus distance at 13 GHz for Horizontal Polarization

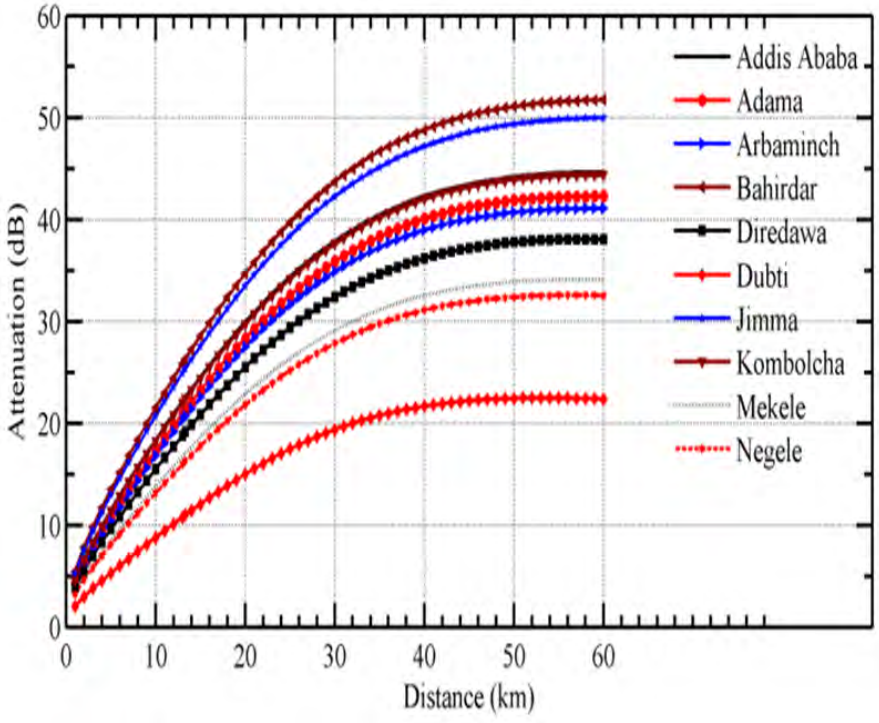

Figure 4-9: Attenuation versus distance at 13 GHz for vertical Polarization

Rainfall occurs some times of the year with varying rates from time to time, hence the rain fade margin needed to compensate for rain attenuation varies with time. Figures 4-10 and 4-11 show the fade depth at various percentages of time. Figure 4-10 gives the attenuation values for horizontal polarization at different percentages of time at 13 GHz and 13.34 km path length. At 0.01% of the time (99.99% availability), the maximum fade depth is 31.14 dB as observed in Bahirdar while the minimum is 12.25 dB recorded in Dubti. For vertical polarization (Figure 4-10) similar distribution of rain fade is observed: the highest value is 26.25 dB in Bahirdar, and the lowest value is 10.97 dB in Dubti for the same path length and operating frequency. Comparing the two graphs, vertical polarization has 14% lower rain attenuation than horizontal polarization.

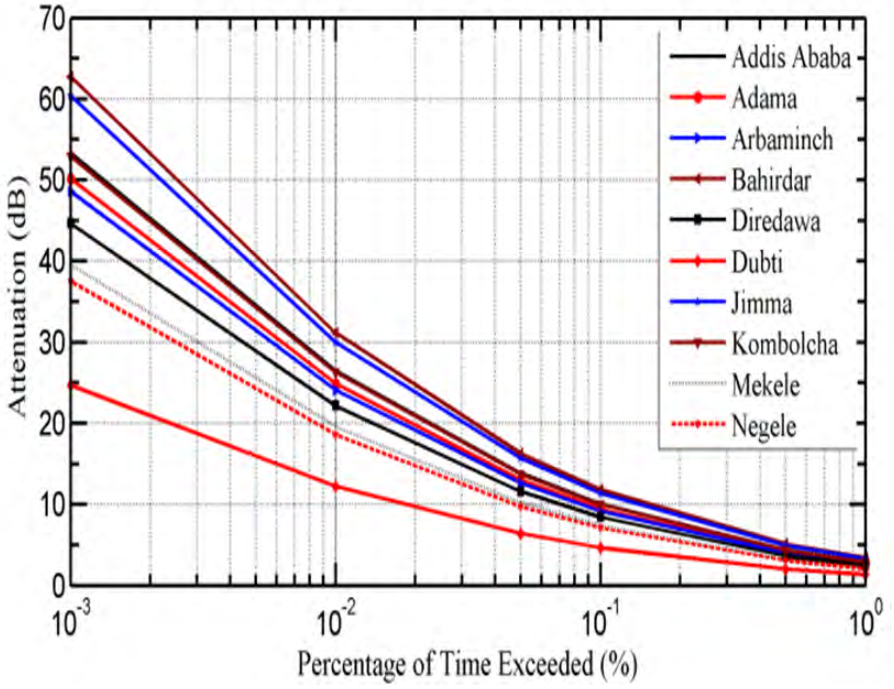

Figure 4-10: Attenuation against exceedance for 13.34 km path distance and 13GHz propagation frequency in horizontal Polarization

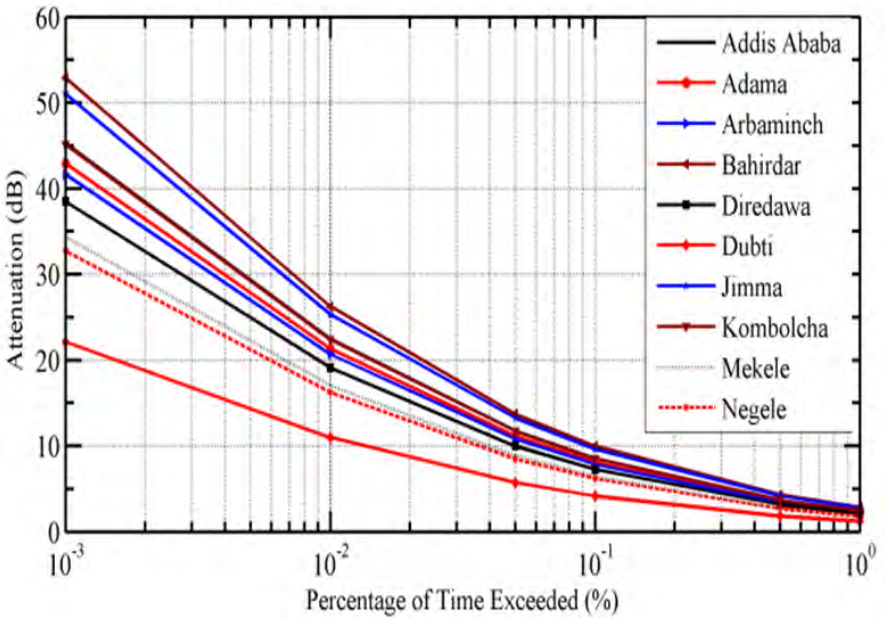

Figure 4-11: Attenuation against exceedance for 13.34 km path distance and 13GHz propagation frequency in vertical Polarization

From the rain attenuation distribution plots shown in Figures 4-10 and 4-11 above, fade margin values are determined at different percentages of time of the year for the ten geographical locations. Tables 4.6 and 4.7 give the required fade margins at 13 GHz and 13.34-km path length for the ten geographical locations in Ethiopia. The reference link availabilities are 99.999%, 99.99%, 99.9% and 99%. As seen from Tables 4.6 and 4.7, the rain fade decreases as availability reduces from 99.999% to 99%.

Figures 4-12 and 4-13 show rainfall fade margin contour maps for horizontal and vertical polarization, respectively. As seen from the maps, the fade margin decreases as we move from the western to the eastern part of the country, and horizontal polarization requires a higher fade margin than vertical polarization.

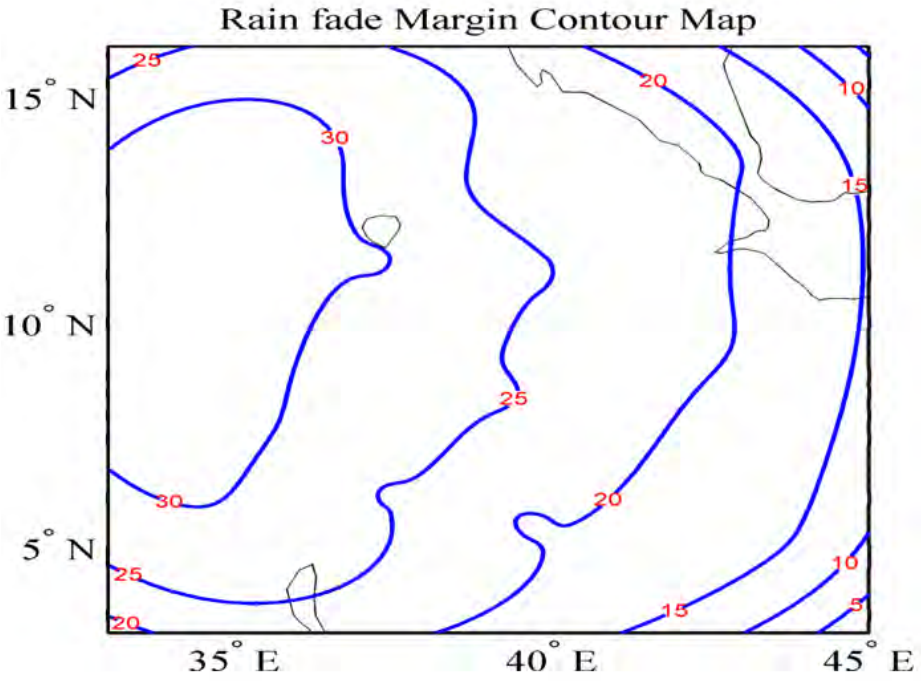

Figure 4-12: Contour map of rain fade using R-H model at 0.01% horizontal Polarization

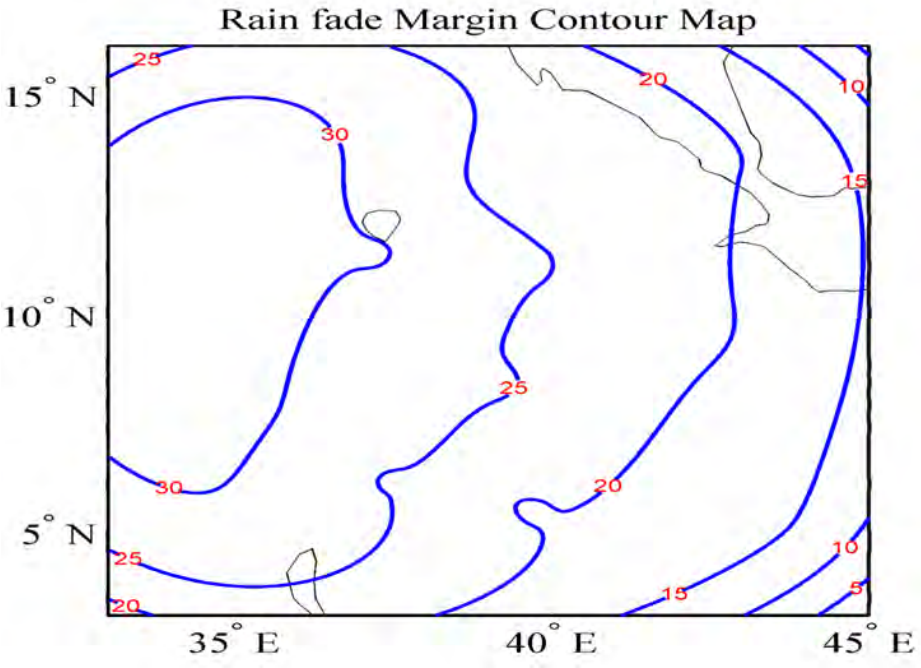

Figure 4-13: Contour map of rain fade using R-H model at 0.01% vertical Polarization

Table 4.6: Rain fade margin at propagation frequency of 13 GHz and path length of 13.34 km in horizontal polarization for 10 locations in Ethiopia

Locations	Fade margin 99.999%	at different 99.99%	percentage of 99.9%	availability (dB) 99%
Adama	50.17	24.90	9.46	2.75
Addis Ababa	53.32	26.46	10.1	2.92
Arbaminch	48.59	24.12	9.16	2.67
Bahirdar	62.75	31.14	11.83	3.44
DireDawa	44.64	22.16	8.42	2.45
Dubti	24.68	12.25	4.65	1.35
Jimma	60.39	29.97	11.39	3.31
Kombolcha	52.93	26.27	9.98	2.90
Negele	37.5	18.61	7.07	2.06
Mekele	39.49	19.60	7.44	2.17

Table 4.7: Rain fade margin at propagation frequency of 13 GHz and path length of 13.34 km in vertical polarization for 10 locations in Ethiopia

Locations	Fade margin 99.999%	at different 99.99%	percentage of 99.9%	availability (dB) 99%
Adama	45.28	22.47	8.54	2.48
Addis Ababa	42.93	21.30	8.09	2.35
Arbaminch	41.66	20.68	7.86	2.29
Bahirdar	52.89	26.25	9.97	2.90
DireDawa	38.49	19.10	7.26	2.11
Dubti	22.14	10.99	4.17	1.21
Jimma	51.04	25.33	9.63	2.80
Kombolcha	45.12	22.39	8.51	2.47
Negele	32.72	16.24	6.17	1.79
Mekele	34.33	17.04	6.47	1.88

4.6 Chapter Summary

In this chapter, rainfall rate distributions for ten geographical locations in Ethiopia are determined at 15-minute sampling rain rate. Chebil model is used to calculate R0.01 at One minute integration time.The R-H model is also then used to convert the local measurement of annual rainfall accummulation into one-minute integration time rain rate distribution at different percentage of exceedance. Also, rainfall rate and fade margin contour maps at 0.01% exceedance are developed for Ethiopia. Using the ITU-R model, specific rain attenuation and total rain attenuation for terrestrial Line-of-Sight links in Ethiopia are predicted for varying frequencies and distances. It is found that the attenuation for shorter link paths is more affected by rainfall than longer distance due to non-uniformity of rain distribution over the link. In descending order, the attenuation of rainfall rate is the highest in the north west and lowest in the south east regions of Ethiopia. In the next chapter, the stochastic model is applied for the characterization and generation of rainfall process over wireless links.

Chapter 5

Rainfall Characterization and Generation from Markov Chains for Rain Fade Modeling over Wireless Links in Ethiopia

5.1 Introduction

In the previous chapter, rainfall rate distribution at different integration times and rainfall rate attenuation over various radio links in Ethiopia were investigated from a different perspective.The understanding of stochastic mechanism behind time-varying rainfall process is an important topic. Therefore, this chapter deals with the time series rainfall process effects over wireless networks by employing the Markov chain model and queueing theory approach. To understand a rain fade process, it is firstly important to understand the underlying behaviour of rainfall over wireless links. With regard to this, several authors have described rainfall as being unstable in time and space, particularly at high rainfall rate areas such as tropical, equatorial and subtropical regions [80, 42, 88, 89, 93, 94] . Therefore, studying the fundamental characteristics of rainfall rate is very important in dealing with effect of rainfall on wireless networks.

Stochastic modelling of rainfall is a challenging task due to its strong variability in time and space [129]. Different approaches have been adopted by researchers for time-

varying characterization of rainfall processes [42, 88, 89, 93, 94] . In [93], Markov chain was applied to model stochastic processes by primarily taking into consideration the state, time index and statistical dependency of the random process. In [126], daily occurrence of rain events were analysed by fitting a two-state, first-order Markov chain. In [90], a multi-state Markov chain model was applied to generate daily rainfall data. In [87], a model for rainfall intensity based on a two-level Markov chain with the states of the chains being connected by a transition probability matrix was studied. In [127], rainfall attenuation in the time domain was generated using N-state Markov chains for microwave networks in Hungary. Heder and Bitos [92] developed a semi-Markov model for land mobile satellite channel and classified the received signal into three Markov states: open air, shadowing, and blocking which were in turn used for statistical improvement of channel modelling. In [88],Alonge and Afullo developed transition matrices for a four regimes of rainfall rate threshold using Markovian assumptions in Durban, South Africa. In [128], the hidden Markov chain was used to generate 3-state rainfall rate, but failed to consider individual spike durations. In these past efforts, researchers explicitly applied Markov chains to model rainfall data; however, they failed to consider sojourn times of rainfall rate spikes - which of course is crucial to rain fade duration analysis. Therefore, rainfall spike duration (sojourn time) and the variability of rainfall spike characteristics within a regime at one minute integration time of rain rate are very important for the prediction of wireless network outages at microwave and millimeteric wave bands, and are thus a crucial focus of the current chapter.

Alonge and Afullo [42, 88, 89], in their studies at Durban (subtropical), South Africa and Butare (equatorial), Rwanda, proposed the required queue parameters describing rainfall process as service, inter-arrival and overlap times, using distrometer measurements. These two sites experience different levels of intense rainfall, which results in different rainfall fading levels over terrestrial and earth-space communication systems, operating at microwave and millimetre bands. By definition, rainfall rate spike service time represents the total duration of a spike in a rainfall event, the inter-arrival time is the time difference between the arrivals of two consecutive spikes, and the overlap time, is the intercept time between starting and stopping of two successive spikes [42, 88, 89]. In their work, they established that the service time of rain spikes is Erlang-distributed given by [42, 88, 89]:

$$f(t_s, k, \mu_s) = \frac{(k\mu_s)t_s^k exp(-k\mu_s t_s)}{\Gamma(k)}[min]^{-1} \; for \; t_s > 0; \forall \Re \tag{5.1}$$

where, μ_s is the average service rate, t_s is the average service time and k is the numberof exponential stages in the queue process. Similarly, the inter-arrival time of spikes is exponentially-distributed and is given by [42, 89, 93]:

$$f(t_a, \lambda_a) = \lambda_a exp(-\lambda_a t_a)[min]^{-1} \; for \; t_a > 0; \forall \Re \tag{5.2}$$

where, λ_a is the average inter-arrival rate and t_a is the average arrival time.

The queueing theory mainly interprets the characteristics of rainfall processes as a catenation of several overlapping rain spikes, which are successively generated in the time domain, resulting in typical event durations. When applied to synthesize rainfall events, the generated time series from queueing theory approach has proved to preserve the original distribution of the rainfall measurements over radio links with significant accuracy [93, 94]. Therefore, since the queueing theory approach is a special case of a Markov chain process, it is proposed to examine the behaviour of rainfall as a Markov chain with transition probability matrices.

In this current effort, we thus explore the relationship between the stochastic properties of rainfall processes and Markov chain model. Firstly, based on experimental measurements from a Davis Vantage weather station installed at Jimma $(7.06670^0, 36.083330^0)$, Ethiopia - a location of intense rainfall - rainfall rate measurements are classified into four distinct rainfall rate regimes: drizzle $(1mm/h \leq R < 5mm/h)$, widespread $(5mm/h \leq R < 10mm/h)$, shower $(10mm/h \leq R < 40mm/h)$, and thunderstorm $(R \geq 40mm/h)$. Using Markov chain approach, transition probability matrices describing rain spikes "jumps" in these regimes are determined. The sojourn times of rainfall spikes attributed to each of the proposed rainfall regimes are estimated and fitted to an appropriate statistical distribution. Secondly, an attempt is made to develop algorithms which are implemented with MATLAB to generate rainfall time series events from the principal elements of the proposed Markov chain model. Furthermore, queueing parameters already discussed in [42, 88, 89, 93, 94] are also obtained for this location and the resulting queue parameters are similarly applied to generate rainfall rate time series for an annual cycle at the same location.A comparison of rainfall rate time series generated from the proposed Markov chain model and semi-Markovian queue approach are then compared with the actual measurements via error analysis.

5.2 Markovian Concepts for Stochastic Rainfall Time Series

Throughout this chapter, a rainfall rate spike is assumed to be a single stochastic unit of the Markov chain process. Basically, three parameters will suffice to characterize this stochastic process: random variable, state spaces and the time index. Since rainfall attenuation is a time-variant process, it is reasonable to assume that Markov chains and queueing discipline could well characterize the behaviour of any rainfall process [87, 90, 127, 92] . A Markov chain is a type of a stochastic process characterized by three important elements: states, transition probability matrix and steady state vector. Depending on the time-varying process under study, the states of the Markov chain are defined by random variables [129, 130, 131, 132, 133]

5.2.1 Statistical Assumptions for Spike Characterization in a Markovian Process

In this presentation, the following assumptions are made for the characterization of rainfall process in a Markov chain model:

A. All rainfall events can be classified into four rainfall rate regimes with each regime assumed to be a state space of a Markov chain. The four states of rainfall rate are defined as:

$$X = \{D, W, S, T\} \tag{5.3}$$

where, D is drizzle, W is widespread, S shower and $T$is for thunderstorm regimes of the spikes.

B. A rain event consists of rain spikes which have a definite sojourn time beyound which they undergo transition in the time domain. The sojourn time of a spike is a random variable of the Markov chain varying within a given state space and may be related to the amplitude of the spike. The sequence of spikes is denoted according to the peak amplitude of each spike given by:

$$x = x_0, x_1, ...x_n \tag{5.4}$$

where x is the spike of rainfall and n is time index. In a more fashionable way, we could consider a random variable, $x_{(n+1)}$, at time $n + 1$ liable to be dependent on its current

probability, x_n, at time, n. Thus, the transition probability from one regime to another is based on a conditional probability relation. For a Markov process, its future probabilistic state depends only on most its current state. How the process arrives at that state is irrelevant [129]. Thus, the conditional probability of a spike going from state i to state j in a time interval is a homogeneous time Markov chain process described by:

$$P(X_{n+1} = j/X_n = i) = P_{ij} \forall i, j \tag{5.5}$$

where P_{ij} is the transition probability $X_n = i$, represents the spike, X in regime, i, at the current time index, n, and $X_{n+1} = j$, represents spike, X , is in a regime, j, at the next time index, $n + 1$. Given the spike's current regime, the next spike regime will be conditionally independent of the past.

From Markov property it can be presented that given the current spike's regime, the next spike's regime is conditionally independent of the past. This statement is seen in Figure 5-1 that gives that the system can move from one state to another or continues remaining in the same regime. Figure 5-1 shows the spikes of rainfall rate remains changing within shower regime for the first 17 minutes and then switches to thunderstorm state. Figure 5-1 also show the spike's queue parameters such as service, inter-arrival and overlap time of spikes. The inter-arrival time, t_a, is defined as the time variation between the arrivals of two successive rain clouds/spikes at the identified reference point. The service time, t_s may be defined as the real duration of the spike. The other parameter, is overlap time t_o , known as the intercept time between a 'dying' spike and arriving spike. Overlapping spikes can be seen as a major factor accommodating the regeneration of detectable.

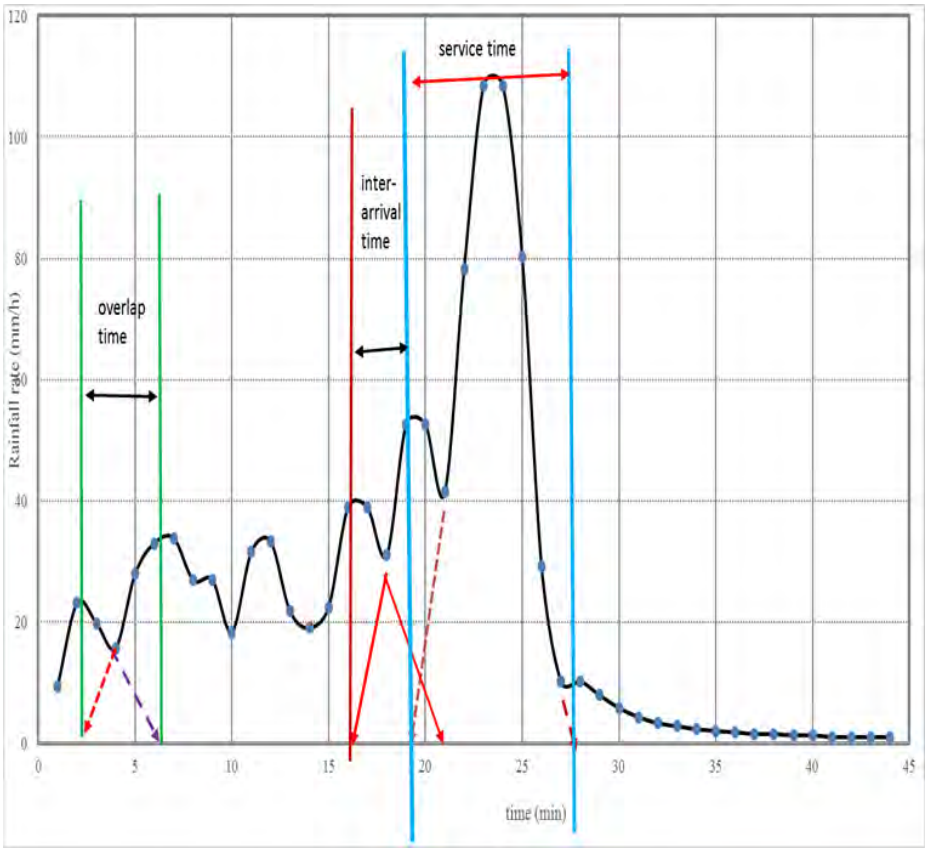

Figure 5-1: Rainfall rate against time in minute on September 3, 2015 at jimma

C. Each spike exists in an event for specified period of time, τ_i, before transiting to another regime. τ_i is defined as sojourn time of spike and subscript ðİŚŨ implies the regimes (or states).

$$\tau_i = \tau_D, \tau_W, \tau_S, \tau_T \tag{5.6}$$

Figure 5-2. explains the details of the sojourn time; where we depict a simple path of four rainfall rate regimes namely: drizzle (D), widespread (W), shower (S) and thunderstorm (T) to show the duration of spikes in a Markov chain. Figure 5-2 shows that the process starts from regime D at time $t = 0$, stays there for an amount of time τ_D, makes an instantaneous state change to state S at time T_1, stays there for τ_S amount of time, makes an instantaneous state change to state W at time T_2, and so on.

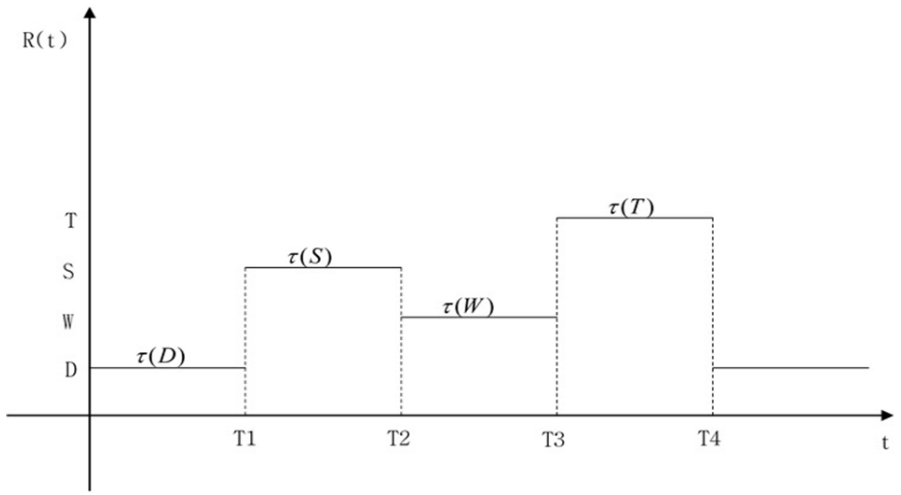

Figure 5-2: Transition pattern between rain spikes of different rain rate peaks in a typical rain event

Since τ_i denotes the sojourn time of rainfall rate spike in state i before transiting to a different regime, the amount of τ_i, the time in which the spike spent in one regime before the transition is also a random process. Therefore, the sojourn time could be characterized from a probability distribution point of view. In this work, the sojourn time distribution of rainfall rate spike is determined statistically from experimental dataset for the four rainfall regimes.

D. The transition probability is bounded within $0 \leq P_{ij} \leq 1$ such that, i, j, $1, , s_n$. Each element in P_{ij} implies the probability of switching from a state, i, to state, j, or remain in the same state. All elements of the matrix are greater than or equal to zero. The general state transition matrix available for $n \times n$ matrix is thus given:

$$P_{ij} = \begin{bmatrix} P_{11} & . & . & P_{1n} \\ . & . & . & . \\ . & . & . & . \\ P_{n1} & . & . & P_{nn} \end{bmatrix} i, j \in n$$

In this work, the values of n are 2, 3 and 4 respectively for widespread, shower and thunderstorm events. i.e for widespread events the transition of the spike is between drizzle and widespread regimes. For shower event, the jumping of spike is among drizzle, widespread and shower rainfall rate regimes and for thunderstorm event the transition of the spike is

among the four rainfall rate regimes.

The state transition matrix available for widespread events is thus given:

$$P_{widespread} = \begin{bmatrix} P_{DD} & P_{DW} \\ P_{WD} & P_{WW} \end{bmatrix}$$

where $P_{DD}, P_{DW}, P_{WD}, P_{WW}$, are the transition probabilities of drizzle (D), and Widespread (W) spikes. The state transition matrix available for shower events is thus given:

$$P_{shower} = \begin{bmatrix} P_{DD} & P_{DW} & P_{DS} \\ P_{WD} & P_{WW} & P_{WS} \\ P_{SD} & P_{SW} & P_{SS} \end{bmatrix}$$

where $P_{DD}, P_{DW}, P_{DS}, P_{WD}, P_{WW}, P_{WS}, P_{SD}, P_{SW}, P_{SS}$ are the transition probabilities of drizzle (D), Widespread (W) and shower (S) spikes. For thunderstorm events P is given by

$$P_{thunderstorm} = \begin{bmatrix} P_{DD} & P_{DW} & P_{DS} & P_{DT} \\ P_{WD} & P_{WW} & P_{WS} & P_{WT} \\ P_{SD} & P_{SW} & P_{SS} & P_{ST} \\ P_{TD} & P_{TW} & P_{TS} & P_{TT} \end{bmatrix}$$

where $P_{DD}, P_{DW}, P_{DS}, P_{DT}, P_{WD}, P_{WW}, P_{WS}, P_{WT}, P_{SD}, P_{SW}, P_{SS}, P_{ST}, P_{TD}, P_{TW}, P_{TS}, P_{TT}$, are the transition probabilities of drizzle (D), widespread (W), shower (S) and thunderstorm (T) spikes.

A transition probability matrix could be expressed as a transition diagram. Each node 0 shows a regime of the Markov chain indicating with a text inside; an arrow links state i with j if a transition exists and the probability transition P_{ij} is written on that linking arrow, even if the transition is to the same state [134]. The diagram is also used to present the model definitions; it is easy to see in this diagram the possible jumps between regimes depending on the probability. Figures 5-3, 5-4, 5.5 present the transition probability diagram for a shower and thunderstorm events of Markov chain with its transition matrix.

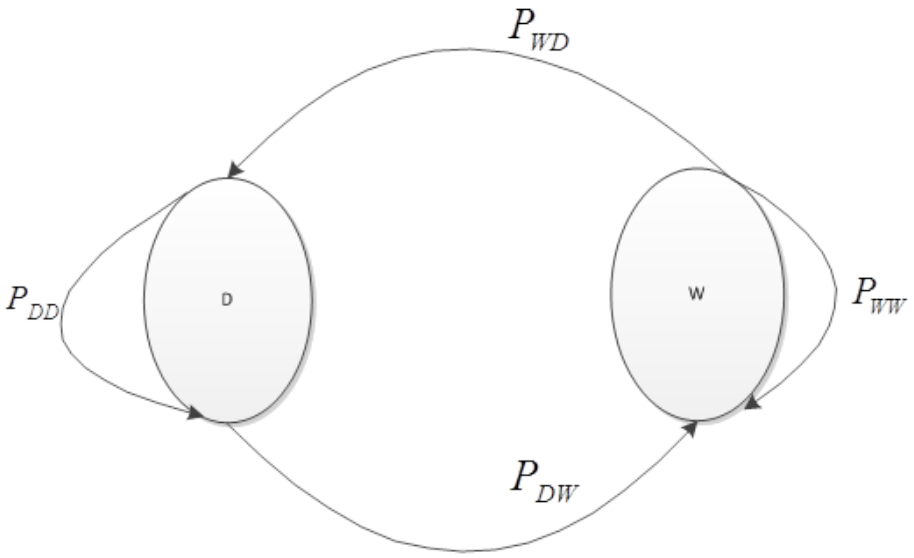

Figure 5-3: State transition diagrams for spikes of rainfall in widespread

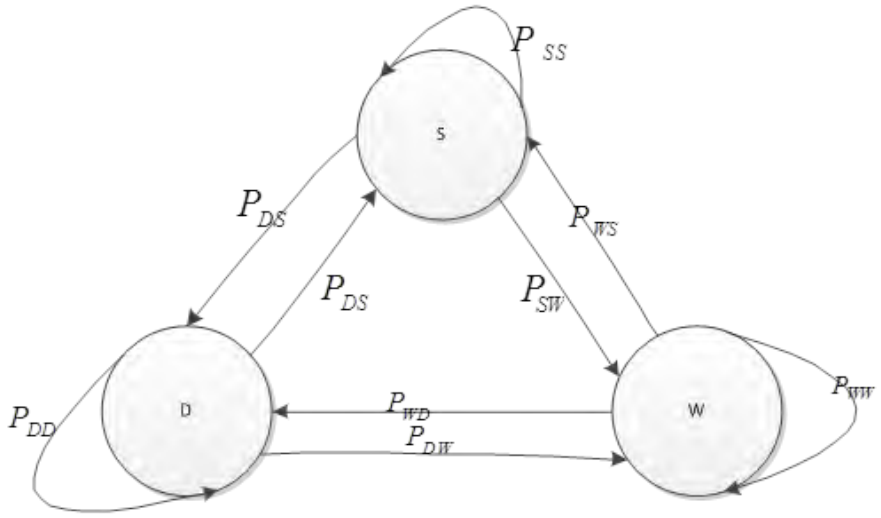

Figure 5-4: State transition diagrams for spikes of rainfall in shower

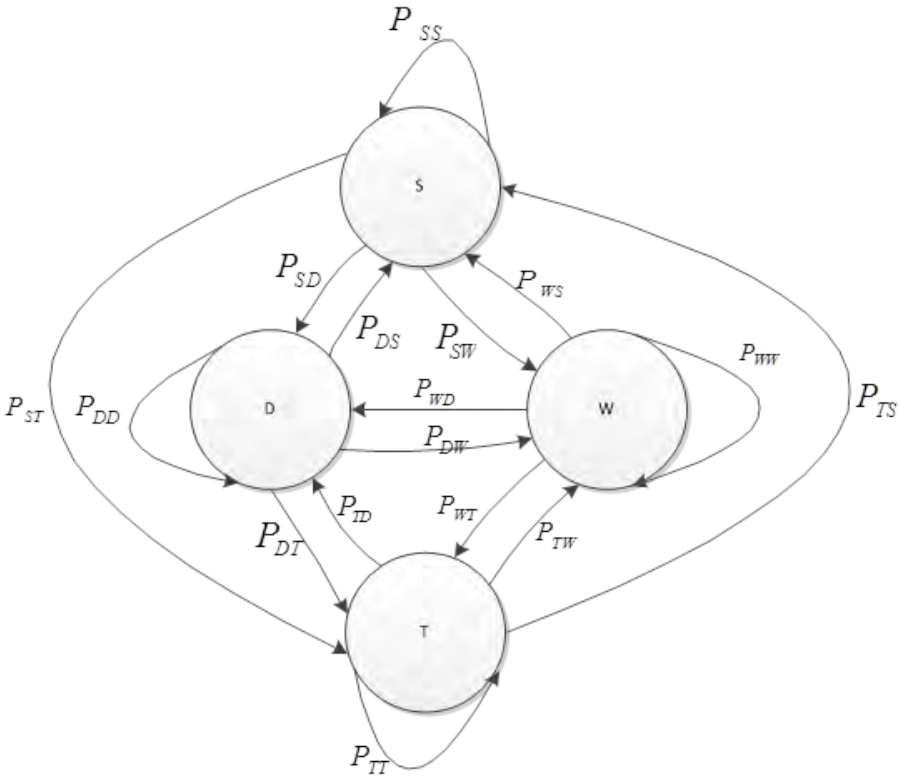

Figure 5-5: State transition diagrams for spikes of rainfall in thunderstorm

E. The other essential parameter of the Markov chains is the vector π of steady-state, which shows the total occurring percentage of the state in the chain. This vector is equivalent to the kth-power of P i.e., P^K. Steady-state behaviour of a Markov chain can be formulated as (5.7). This is given in [135]:

$$[\pi_1, ...\pi_n] = [\pi_1, ...\pi_n] \begin{bmatrix} P_{11} & . & . & P_{1n} \\ . & . & . & . \\ . & . & . & . \\ P_{n1} & . & . & P_{nn} \end{bmatrix}$$

where, π_i, is the steady state probability for n states, whereas the sum of elements within this probability vector at steady state must be unity:

$$\sum_{i=1}^{n} \pi_i = 1 \tag{5.7}$$

5.2.2 Model Calibration

In this thesis, two statistical tools analysed namely; the root-mean-square error ($RMSE$) and χ^2 statistics are applied to test the goodness-of-fit for the proposed model with respect to the actual measurements. The following relationships will therefore suffice for this purpose:

$$RMSE = \left[\frac{1}{N}\sum_{i=1}^{N}(E_i - F_i)^2\right]^{\frac{1}{2}} \tag{5.8}$$

$$\chi^2 = \sum_{i=1}^{N}\frac{(E_i - F_i)^2}{E_i} \tag{5.9}$$

where E_i is the dataset from measurement and F_i is the proposed model dataset for number of sample size, N.

5.3 Measurements and data processing

Measurements for this study were obtained from an experimental setup located at the Jimma Institute of Technology of Jimma University ($7.6670^0, 36.83330^0$), in the Oromia region, Ethiopia. This location is at the South-Western part of Ethiopia, about 350 km away from the capital city Addis Ababa. Jimma has an average annual rainfall accumulation of around 1400 mm and is categorized, according to Koppen climatic classification, as class Cfb (warm temperate) [136, 137]. Beginning from August 2015, in-situ rainfall rate measurement began at this site using David Vantage Vue weather station, and is currently ongoing. This equipment consists of an outdoor unit, a wireless Integrated Sensor Suite (ISS), that collects rainfall data at one minute integration time (every 60 seconds), using collector-type tipping spoon which has a resolution of 0.2mm per tip shown in Figure 5.6. It also records other environmental parameters such as: temperature, pressure, relative humidity, wind speed and wind direction. The precision of the device is 1% litre/h with capacity to record rainfall rate bounds between 2 mm/h and 400 mm/h. For raw data harvesting, the data logger lodged on a personal computer is connected to the ISS via wireless antenna systems, through a USB interface.

Figure 5-6: The indoor console and the outdoor ISS units of the Davis Vantage Vue electronic weather station at Jimma University

To process this data, extracted rainfall measurements are processed and categorized into four rainfall bounds according to the following regimes: drizzle ($1mm/h \leq R < 5mm/h$), widespread ($5mm/h \leq R < 10mm/h$), shower ($10mm/h \leq R < 40mm/h$) and thunderstorm ($R \geq 40mm/h$). Data processing for sojourn time is done by plotting graphs of rainfall rate against time for 117 rainfall events as shown in Table 5.1. From these graphs, the duration of each spike is estimated by identifying its onset and completion of individual spikes in the time domain; these durations correspond to the spike sojourn time. This process is repeated for all rain events recorded at Jimma. However, extra time values resulting from overlapping spikes were computed using Newton's divided difference method as suggested in [5] . Table 5.1, shows the measured rainfall statistics obtained from the location. It is observed that of the total 12 months duration of measurement in Jimma, drizzle events account for 5.13% of rainfall occurrence; while widespread 11.11% occurrence, for shower 34.18% and for thunderstorm 49.57%. This suggests Jimma as a location where intense rainfall events are experienced, at least 50% of the time. Overall, rainfall events at this location consist of a large spectrum of shower and thunderstorm rainfall events, with a few occasions of drizzle and widespread events.

Table 5.1: Summary of Rainfall Rate Events Recorded over Measurement Period

Regimes	No of events	No of spikes	Rainy time(min)	accuml (mm)
drizzle	6	10	670	30.32
widespread	13	31	1001	66.52
shower	40	124	2046	182.19
thunderstorm	58	241	4408	903.5
Total	117	406	8125	1182.23

5.4 Results and discussion from sojourn time

5.4.1 Sojourn Time Distribution of Rainfall Rate Spikes

In theory, the duration of a rainfall spike in any regime can be correlated with the fade duration - which implies that longer spike duration (sojourn time) may lead to longer fade duration. Therefore, it is very important to understand the distribution of the sojourn time of rainfall spikes in each rainfall regime as it is essential component for analysing fade duration and outage frequency in wireless networks. From experimental measurements in Jimma, the Probability Density Function (PDF) of the sojourn time is statistically determined for the four rainfall regimes. Depending on the values of coefficients of variation (CV) for each state, the exponential or Erlang-k probability distributions is decided as the better fit model of the sojourn time distribution modelling of rain spikes. However, as seen in the Table 5.2, consistent values of CV being less than 1 strongly suggest that Erlang-k distribution is the more predictable model fit. From Table 5.2, it is observed that the mean sojourn time of rainfall decreases from drizzle to thunderstorm regimes. This implies that the spike spends more time in the drizzle regime before switching to any other state. For radio links, it should be noted that rain fade will depend on the spike sojourn time and the peak amplitude attained by the spike in a regime. For Erlang-k distribution, the required number of exponential stages, k, for different regimes is derived in [93] as:

$$K = round\left[\left(\frac{maxf(t_{soj}, k, \epsilon_{soj})}{0.4488\epsilon_{soj}}\right)^{2.11}\right] \tag{5.10}$$

where $f(t_{soj}, k, \epsilon_{soj})$ is the PDF and ϵ_{soj} is the sojourn rate, both obtained from measurements at Jimma.

Results obtained from (5.10) show different values of k for different spike sojourn distribution from drizzle to thunderstorm regimes. Additionally, it is observed that the average-

Table 5.2: Fitted Distributions and Parameters for Spike sojourn time for Different Rain Regimes

Rainfall regimes	Sojourn time	CV	Models	$RMSE$	χ^2	DF	SL
Drizzle	19.95	0.41	Erlang(k=5)	0.0166	0.0655	14	23.685
			Exponential	0.02202	0.17	14	23.685
Widespread	9.37	0.486	Erlang(k=5)	0.0128	0.166	20	31.41
			Exponential	0.0218	0.495	20	31.41
Shower	15.52	0.573	Erlang(k=3)	0.0068	0.045	19	30.144
			Exponential	0.0137	0.0882	19	30.144
Thunderstorm	12.33	0.578	Erlang(k=4)	0.0067	0.0072	15	24.996
			Exponential	0.0206	0.15	15	24.996

sojourn time decreases with increasing rainfall rate from drizzle to thunderstorm regimes. This implies that in Jimma the spike duration in a given state decreases as the peaks of the rainfall rate increases. The spike stays for an average time of 19.95 min, 19.37 min, 15.52 min and 12.33 minutes in drizzle, widespread, shower and thunderstorm states, respectively, before switching to other regimes. The sojourn rate increases progressively in ascending order with the spike's state. The transition from one regime to another is defined by the transitional probability matrix.

Figures 5-7, 5-8, 5-9, 5-10, show sojourn time distributions obtained for the four rainfall rate regimes in Jimma. Stating from Table 5.2, the suitability of exponential and Erlang-k probability distributions are compared in modelling the sojourn time using error analysis. Results from error analysis, show that, the Erlang-k model is a better fit for all rainfall regimes (from drizzle to thunderstorm) as it has lower $RMSE$and χ^2compared to the exponential distribution. The assumption taken for sojourn time distribution in this work therefore depends on the elastic shape profile of basic phase-like Erlang-k distribution.

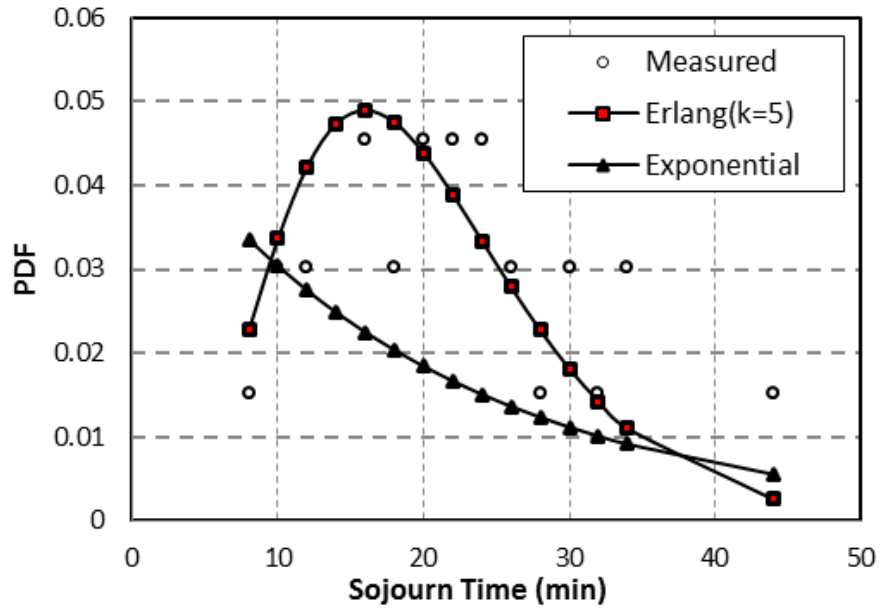

Figure 5-7: Probability Density Function (PDF) for Sojourn time of rainfall spikes in drizzle rainfall rate regimes at Jimma

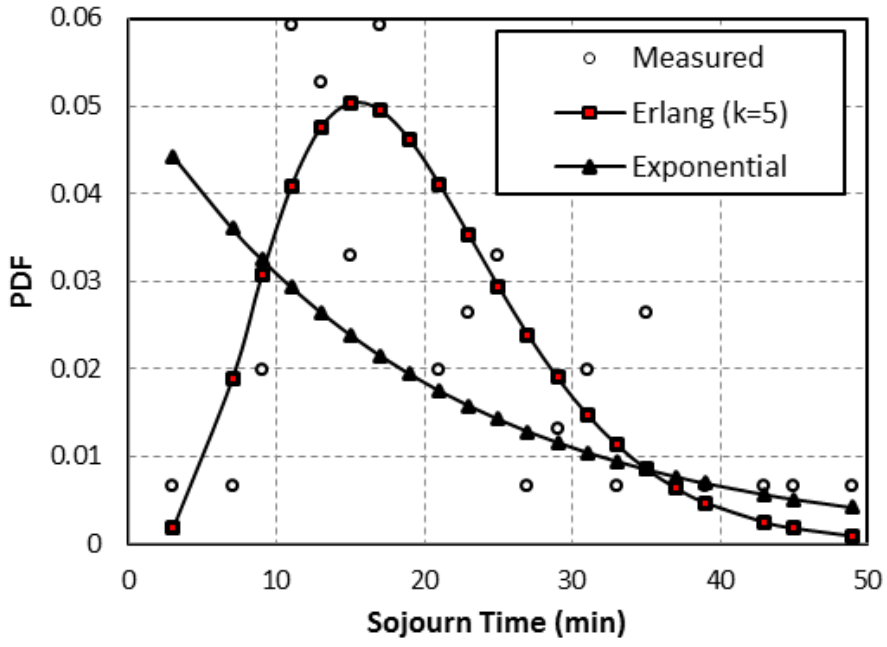

Figure 5-8: Probability Density Function (PDF) for Sojourn time of rainfall spikes in widespread rainfall rate regimes at Jimma

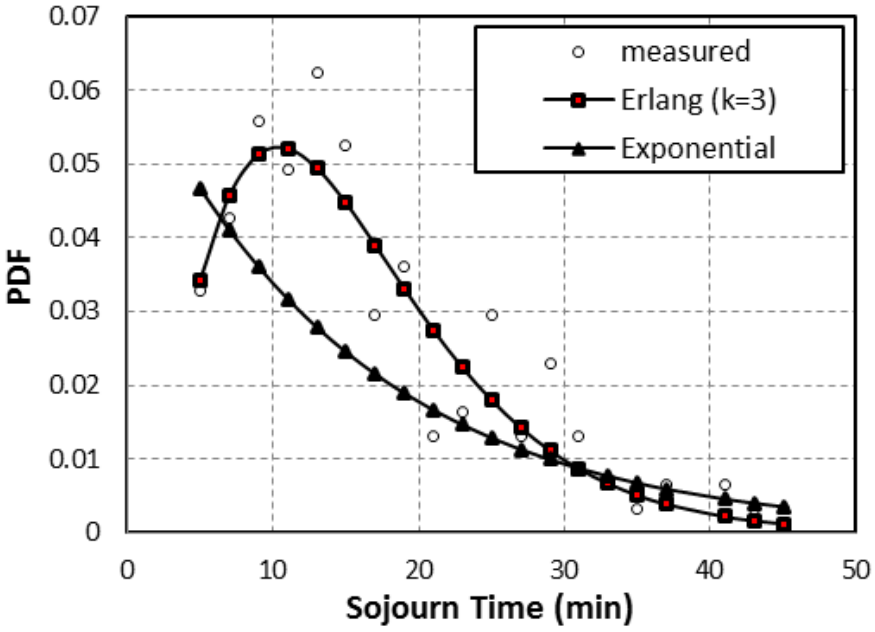

Figure 5-9: Probability Density Function (PDF) for Sojourn time of rainfall spikes in shower rainfall rate regimes at Jimma

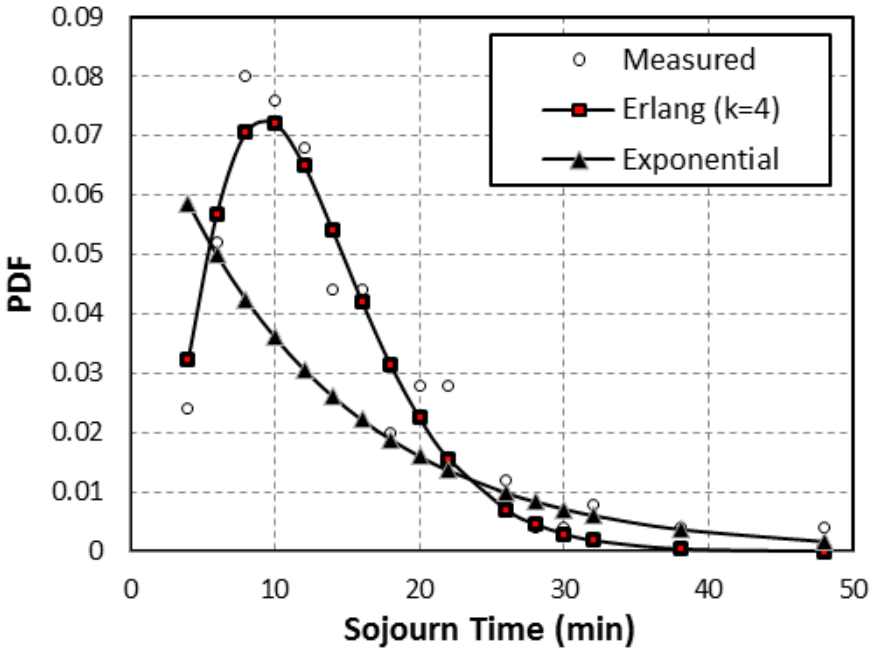

Figure 5-10: Probability Density Function (PDF) for Sojourn time of rainfall spikes in thunderstorm rainfall rate regimes at Jimma

5.4.2 Relationship between Sojourn Time and Peak Rainfall Rate in Jimma

In this work, it is observed that the average sojourn time and corresponding average peak rainfall rate are related by a power-law relationship given by:

$$T_{soj} = aR_P^b[min]^{-1} \tag{5.11}$$

where T_{soj} is the sojourn time, R_P is the peak rainfall rate while a and b are coefficients of the power law relationship as shown in Figure 5-11. The coefficients are a = 25.015 and b = -0.167, which implies a negative power-law relationship.

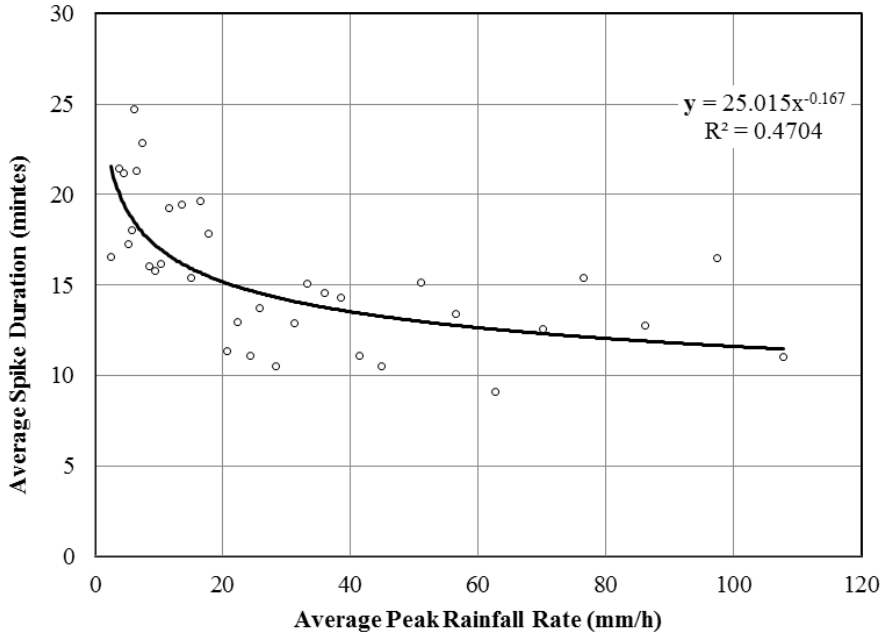

Figure 5-11: Relationship between the average spike duration and peak rainfall rate observed at Jimma

5.4.3 Transition Probability Matrices and State Vectors for Rainfall Spikes in Different Regimes

Transition matrix for drizzle events is excluded because it undergoes no transition between states; hence, it will always remain in a drizzle state. For the limiting distribution, which is the steady state vector of transiting spikes within different rainfall events, their vectors

are presented hereafter.The limiting distribution values are obtained at n iterations (as discussed in 5.2.1) where $n = 5$, $n = 28$ and n= 19 for widespread, shower, and thunderstorm events, respectively. It is observed for widespread events at steady state, the probability of drizzle and widespread spikes are 35.71% and 64.28 % respectively. For shower event at steady state, the probability of drizzle, widespread and shower spikes are 10.09%, 40.13% and 49.76% respectively. The occurrence probability for rainfall rate spike in thunderstorm events are 4.67 % for drizzle, 13.79 % for widespread, 34.92 % for shower and 46.6 % for thunderstorm, respectively. For all rain events, the occurrence probability increases from drizzle to widespread spike in widespread event, drizzle spikes to shower spikes in shower events, and from drizzle to thunderstorm spikes in thunderstorm rainfall rate events. A drizzle event can only generate drizzle spikes and hence, will continually maintain one state which is drizzle.

The state transition matrix available for widespread events is given as:

$$P_{widespread} = \begin{bmatrix} 0.4 & 0.6 \\ 0.3333 & 0.6667 \end{bmatrix}$$

with widespread steady state vector = [0.3571 0.6428]

The state transition matrix available for shower events is given as:

$$P_{shower} = \begin{bmatrix} 0.2857 & 0.57143 & 0.14287 \\ 0.10526 & 0.658 & 0.23684 \\ 0.06 & 0.16 & 0.78 \end{bmatrix}$$

with shower steady state vector = [0.1009 0.4013 0.4976]

The state transition matrix available for thunderstorm events is given as:

$$P_{thunderstorm} = \begin{bmatrix} 0.25 & 0.25 & 0.375 & 0.125 \\ 0.058 & 0.471 & 0.235 & 0.235 \\ 0.048 & 0.161 & 0.484 & 0.306 \\ 0.0215 & 0.01 & 0.28 & 0.69 \end{bmatrix}$$

with thunderstorm steady state vector = [0.0467 0.1379 0.3492 0.466]

5.5 Generation of Rainfall Events from Markov Chain Model

So far in this work, the transition probability matrices representing spike jumps for different rainfall regimes as well as the average sojourn time for each rainfall regime, have been determined from measurements in Jimma. Understandably, the application of rainfall time series concept in Markov chain models could assist in the synthesis of the random behaviour of rainfall events. In this section, rainfall rate events are generated in MATLAB accordingly. Finally, the accuracy of the proposed Markov chain synthesis, alongside the queue synthesis approach, is compared with rainfall measurements from the rain gauge.

The following steps are applied in the generation and implementing of the Markovian chain code in

(a) Firstly, four ranges of random natural numbers between 0- 5, 5- 10, 10-40, 40- 150 are generated to allocate spike slots for peak rainfall rates according to drizzle, widespread, shower and thunderstorm rainfall events respectively. Secondly, generate a random number between 0 and 1. A chain length is chosen corresponding to the rainy minutes in a rain regime.

(b) The transition matrix for a particular rainfall event is used to determined spike transitions within a designated rain event. This process generates spike slots by using some of sort random walk process in which probabilities in step (a) are compared with the desired transition matrix.

(c) On generating peak rainfall rate series from step (b), (5.11) is used to determine the average sojourn time for each spike in a typical event. Each spike will therefore be assigned a constant peak rain rate throughout its lifespan as seen in Figures 5-12, 5-13, 5-14, 5-15.

For generating other rainfall events, similar procedures are applied. On implementing the Markovian schedule in MATLAB:, a total of 7360 minutes of rainfall rate samples were generated of which drizzle, widespread, shower and thunderstorm regime accounts for 313, 639, 2321, and 4087 rainfall samples respectively. For validation of the model, the rainfall rate data of 8125 minutes recorded via David vantage vue at one minute integration time in Jimma University over 2015 and 2016 was used as a reference point. Since a Markov chain allows the transition of rainfall spike from one regime to another over time, it is shown in Figures 5-12, 5-13, 5-14, 5-15, that decision of spikes switching from one regime to another,are informed by the behaviour of the underlying transition probability matrix. Figures 5-12,

5-13, 5-14, 5-15 presents typical Markov-generated samples for drizzle, widespread, shower and thunderstorm rainfall events for 15 spikes resulting in different event durations due to their perspective sojourn time.

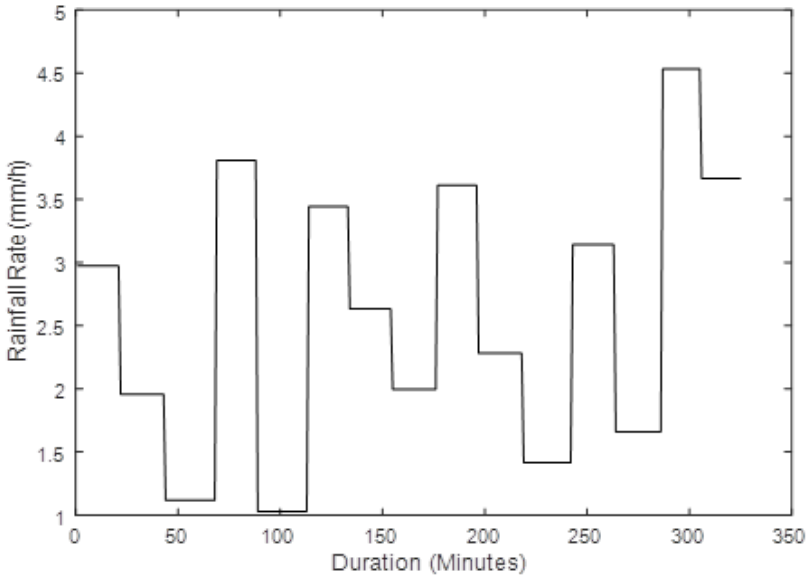

Figure 5-12: Synthetically generated drizzle rainfall events from Markov chain model

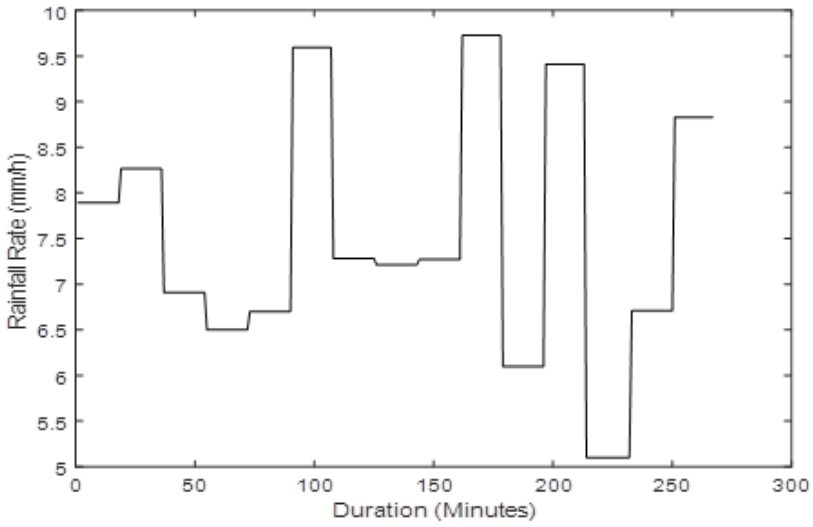

Figure 5-13: Synthetically generated widespread rainfall events from Markov chain model

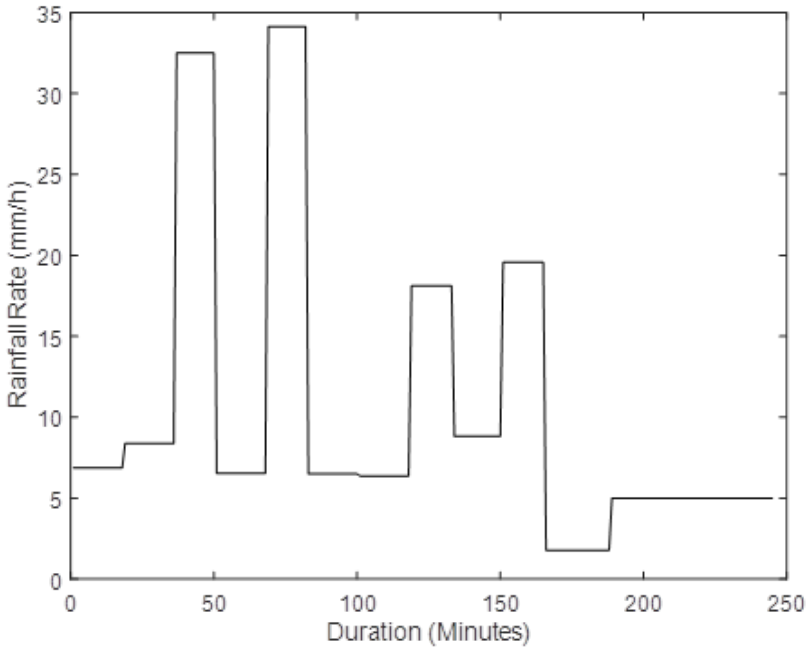

Figure 5-14: Synthetically generated shower rainfall events from Markov chain model

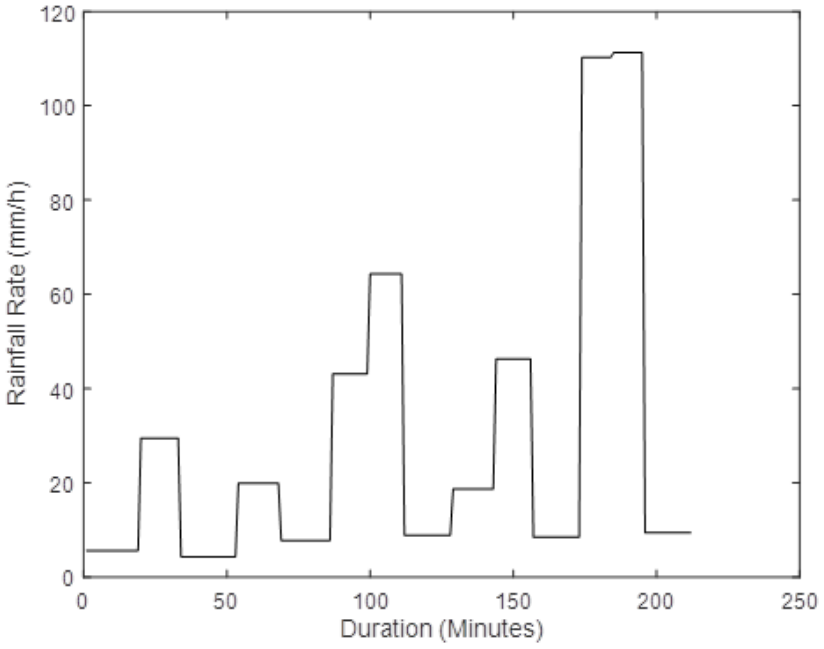

Figure 5-15: Synthetically generated thunderstorm rainfall events from Markov chain model

5.6 Results from Queueing Theory Technique: Service, Inter-arrival and Overlap Time Distributions

Based on previous works by Alonge and Afullo [42, 88, 89], a well-defined queueing paradigm is similarly proposed to describe queue characteristics of rainfall events at Jimma, Ethiopia. Queue parameters describing the underlying process of time-varying rainfall are obtained namely; service time, inter-arrival time and overlap time from the actual rainfall measurements. Also, Table 5.3 and 5.4 generally present appropriate fitting models for different rainfall regimes in Jimma. Based on earlier results on queueing theory approach at Durban and Butare, it is similarly established in our current result that Erlang-k distribution is a better fit to spike service time dataset for all regimes, compared to exponential distribution. This can be confirmed from the lower values of $RMSE$ and χ^2 estimated from the model. Table 5.3 also shows that the average service rate tends to decrease with increasing rainfall regime events. Similarly, both inter-arrival time and overlap time distributions are found to be exponentially and Erlang-k distributed, respectively, with least values of $RMSE$ and χ^2. It is shown in Table 5.4 that the average inter-arrival rate tends to increase with the rainfall regime from shower to thunderstorm regime. In all cases, $RMSE$ and χ^2 statistical tests between measured and modelled results are found to be within the acceptable limits. It is evident that the underlying rainfall process at Jimma follows a semi-Markovian pattern as observed in earlier works at Durban and Butare.

5.6.1 Service Distribution of Rainfall Spikes in Jimma

The service time distribution is assumed to follow the Erlang-k with the values of k selected depending on the model probability density function that results in minimum error with respect to the measured probability density function of rainfall rate spike's service time. Therefore, the selected integer k values for shower event is 3 while it is 4 in thunderstorm rainfall rate events. Figures 5.16, 5.17, 5.18, 5.19 and Table 5.3 show that the average service time increases with decreasing rainfall rate events 18.53 minute for shower and 14.485 minute for thunderstorm and the service rate is the inverse of average service time. Applying $RMSE$ and χ^2 for the two rainfall events DF and SL are in accepted regions. In Table 5.3, there are n=22 and n=20 time categories into which the occurrences have been grouped for shower and thunderstorm events of service time respectively. The degrees of freedom (DF)

being equal to n - 1, that is 21 and 19 for events of shower and thunderstorm service times respectively.

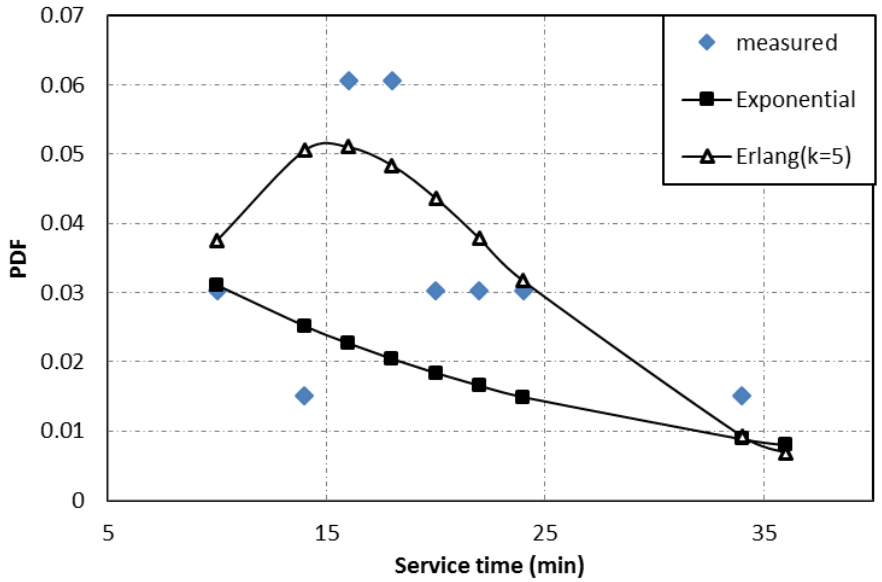

Figure 5-16: Probability density function (PDF) graph for service time of rainfall spikes in drizzle rainfall event

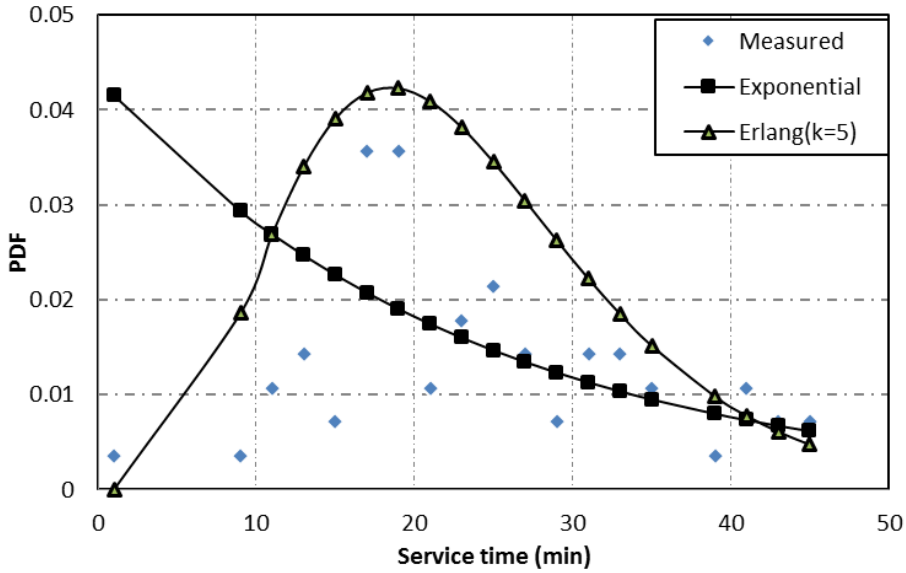

Figure 5-17: Probability density function (PDF) graph for service time of rainfall spikes in widespread rainfall event

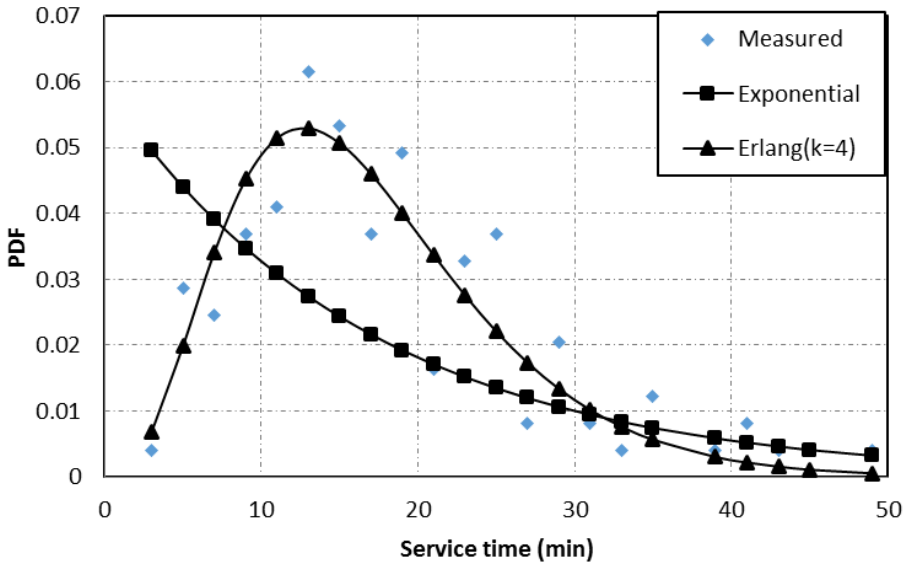

Figure 5-18: Probability density function (PDF) graph for service time of rainfall spikes in shower rainfall event

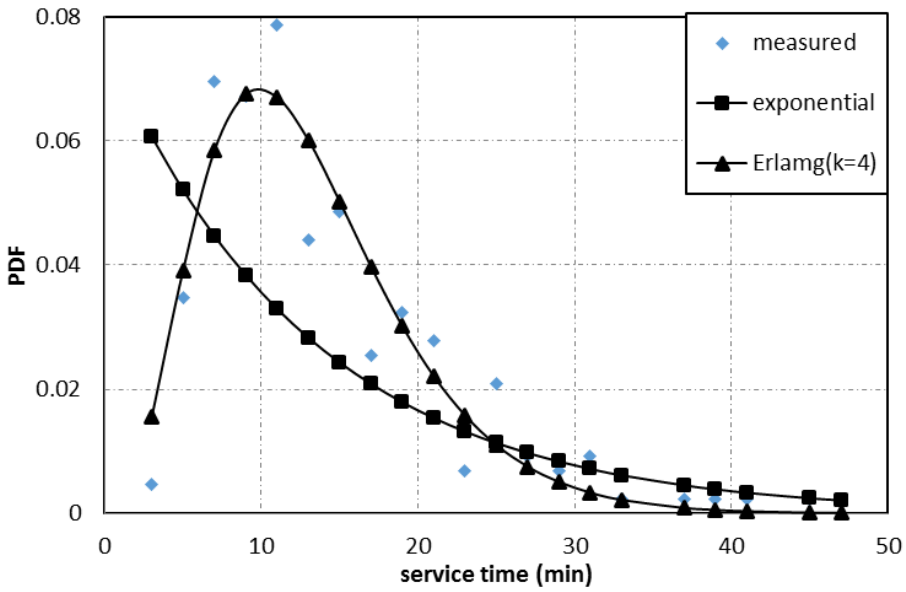

Figure 5-19: Probability density function (PDF) graph for service time of rainfall spikes in thunderstorm rainfall event

Table 5.3: Service time parameters for probability density function (pdf) of the proposed models

Rainfall regimes	Rate parameter	Models	$RMSE$	χ^2	DF	SL
Drizzle	0.0525	Erlang(k=5)	0.0275	0.122	9	16.919
		Exponential	0.0305	0.141	9	16.919
Widespread	0.0434	Erlang(k=5)	0.0184	0.1805	19	30.144
		Exponential	0.0226	0.2695	19	30.144
Shower	0.059	Erlang(k=4)	0.008	0.074	21	32.671
		Exponential	0.0175	0.62	21	32.671
Thunderstorm	0.0762	Erlang(k=4)	0.0074	0.0735	19	30.144
		Exponential	0.029	0.62	19	30.144

Table 5.4: Inter-arrival time parameters for probability density function (pdf) of the proposed models

Rainfall regimes	Rate parameter	Models	$RMSE$	χ^2	DF	SL
Drizzle	0.0645	Erlang(k=3)	0.0195	0.0833	9	16.919
		Exponential	0.0364	0.147	9	16.919
Widespread	0.0434	Erlang(k=3)	0.01586	0.1986	19	30.144
		Exponential	0.0223	0.31	19	30.144
Shower	0.0919	Erlang(k=3)	0.0142	0.0059	20	31.14
		Exponential	0.0123	0.0456	20	31.14
Thunderstorm	0.1017	Erlang(k=5)	0.012	0.0609	19	30.144
		Exponential	0.0193	0.1041	19	30.144

5.6.2 Inter-arrival Time Distribution of Rainfall Spikes in Jimma

The inter-arrival time t_a, of spike is the time difference between two successive rainfall rate spikes at the point of time reference as shown in the Figures 5.20, 5.21, 5.23, 5.24. Average inter-arrival time is obtained from measured data are 15.49, 19.6, 11.54 and 9.6 minutes for drizzle, widespread, shower and thunderstorm events respectively. It shows that the average inter-arrival rate increases with the rainfall rate spikes from widespread to thunderstorm. The distribution of drizzle, widespread and shower inter-arrival time are characterized by Erlang-k model using $RMSE$ and χ^2 statistical fitness test between measured and models while exponential is fit thunderstorm events. Statistical results found in the acceptable limits as seen in the Table 5.4 and Figures 5.20, 5.21, 5.23, 5.24.

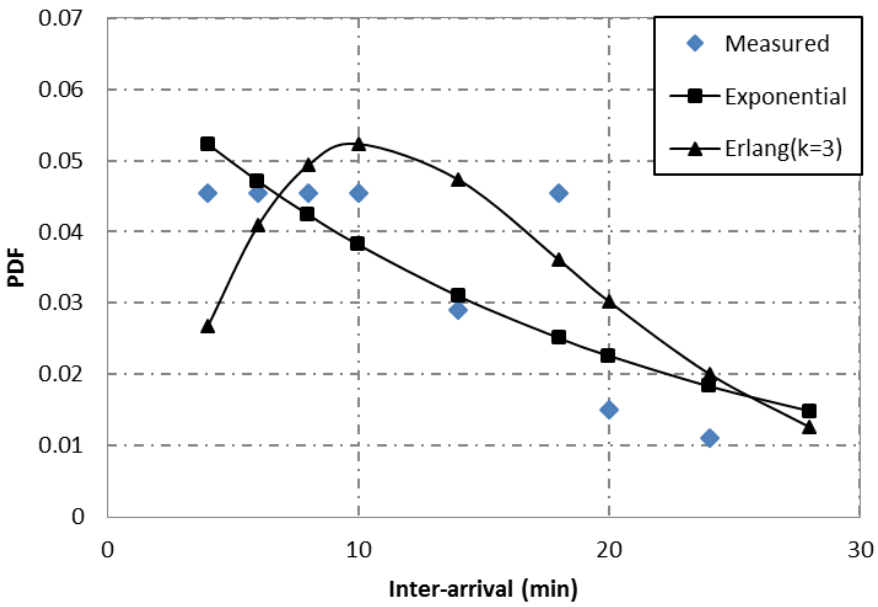

Figure 5-20: Proposed inter-arrival time distribution for drizzle rainfall event

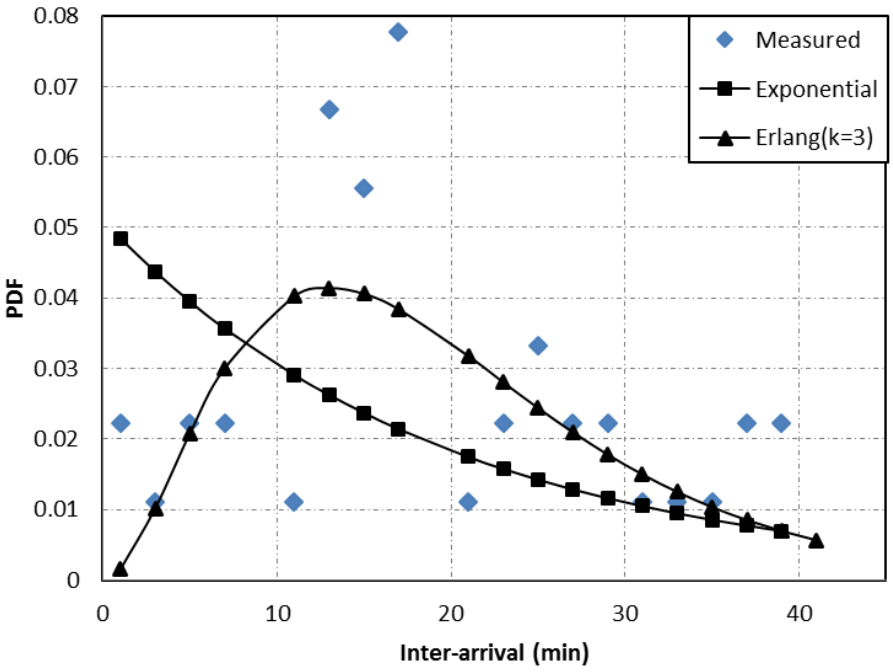

Figure 5-21: Proposed inter-arrival time distribution for widespread rainfall event

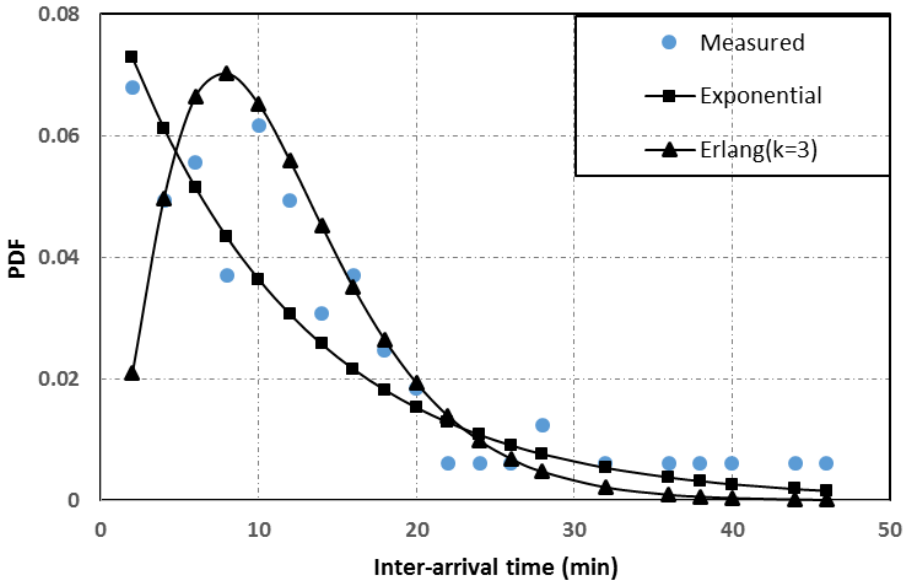

Figure 5-22: Proposed inter-arrival time distribution for shower rainfall event

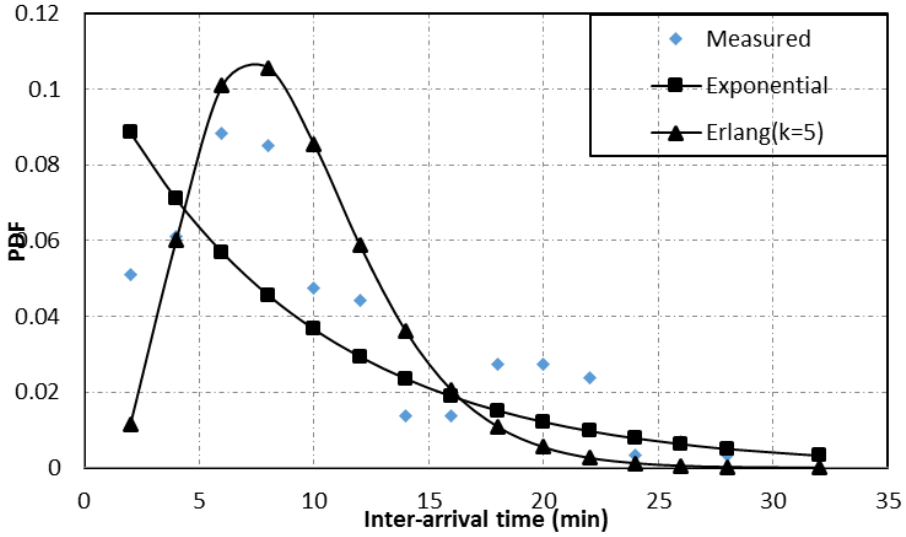

Figure 5-23: Proposed inter-arrival time distribution for thunderstorm rainfall eventt

5.6.3 Overlap Time Distribution of Rain Spikes at Jimma

The overlap time is the intercept time between the stopping (departing) of one rainfall rate spike and arriving of the consecutive spike as seen in Figure 5.1. The mean overlaps time for spike shower rainfall rate events is less than that of thunderstorm spike. Based on the CV

Table 5.5: Fitted parameters of exponential and Erlang- k probability distribution of spike overlap time in Jimma

Rainfall regimes	Rate parameter	Models	$RMSE$	χ^2	DF	SL
Drizzle	0.1613	Erlang(k=3)	0.0766	0.1678	4	9.488
		Exponential	0.0947	0.2115	4	9.488
Widespread	0.096	Erlang(k=3)	0.0159	0.1986	16	26.296
		Exponential	0.0226	0.2694	16	26.296
Shower	0.122	Erlang(k=3)	0.0125	0.048	11	19.675
		Exponential	0.031	0.24	11	19.675
Thunderstorm	0.127	Erlang(k=5)	0.0167	0.157	15	24.996
		Exponential	0.013	0.105	15	24.996

values both Erlang -k and exponential models are applied as seen in the table 5.5. The table shows Erlang k model is the best fit for the spikes of shower events where as the exponential model results in minimum error for thunderstorm spike. However, applying $RMSE$ and χ^2 for the two models the results are seen to be within the acceptable error limits.

5.6.4 Determination of Number of Servers in a Queue Systems at Jimma Ethiopia

Average time, T, is a time in which a spike spent in a system is equal to the sum of waiting time and service time [14]. Since there is no waiting time in the rainfall rate spike scenario, then the average number of spikes N in steady state is given as [128].

$$N = \lambda T \tag{5.12}$$

Where λ is an average inter-arrival rate and T is a time in which a spike is spent in a system (spike duration) that is exactly equal to sojourn time (service time) of spike.

$$T = W + t_s \tag{5.13}$$

$$T = t_s = \frac{1}{\mu} \tag{5.14}$$

where, W is the waiting time, t_s is the service time and $\frac{1}{\mu}$ is the service rate of the queue system. From the average number of spikes, the utilization rho is given by [128], (15.15, 15.16)

Table 5.6: Utilization factor and number of queue servers for the four rain events

Regimes	Utilization factor	Average number of spikes	Number of servers
drizzle	0.63	1.7	1.95
widespread	0.7045	2.92	1.98
shower	0.79	3.74	1.971
thunderstorm	0.81	4.205	1.9

$$\rho = \frac{N}{N+1} \tag{5.15}$$

$$\rho = \frac{\lambda}{m\mu} \tag{5.16}$$

Where, m is the number of servers in a queue system calculated from the above equation

5.6.5 Generation of Rainfall Events from Queue Models

To generate rainfall events, different queue parameters defined in [42, 89, 93] are obtained for four rainfall regimes in Jimma. The queue algorithm proposed by [93, 94] is then implemented in MATLAB for a total of 117 measured rainfall events recorded in Jimma over a period of 12 months. The percentage of occurrences for these regimes are as follows: drizzle (5.128%), widespread (11.11%), shower (34.18%), and thunderstorm (49.57%). These statistics are thereafter used as inputs for the queue model. In this work, a total of 6494 minutes of which 3220, 2220, 722, and 333 minutes are of thunderstorm, shower, widespread and drizzle rainfall events respectively, are generated from the queue model.

5.7 Validation and Comparison of Semi-markovian and Queueing Theory Models from Rainfall Time Series Synthesis

In addition to the MATLAB: implementation procedures described under 5.5 and 5.6, synthetic rainfall time series were carefully examined to determine their capability to preserve statistical properties and its parent dataset. This is achieved by evaluating the applicability of Markov chain and queue theory approaches for rainfall event generation. In this perspective, the two most important statistical representations used to verify these approaches are the Probability Density Function (PDF) and time exceedance distribution.

Table 5.7: Power-law coefficients for the relationship between number of spikes and event duration

Regimes	Markov model			Queue model		
	a	b	R^2	a	b	R^2
Drizzle	20.614	1.0074	0.9995	21.005	1.0079	0.995
Widespread	17.614	1.0034	0.9999	18.494	0.9996	0.9958
Shower	16.899	1.0259	0.9995	15.458	0.9774	0.9954
Thunderstorm	14.536	1.0391	0.9991	14.536	0.9459	0.9995

5.7.1 Relationship between Spike Numbers with Event Duration

While generating rainfall events from Markov chain and queueing theory models, it is observed that the number of generated rainfall spikes and rain event duration show strong relationship. Statistical analysis from generated rainfall data indeed confirms a positive power-law relationship exists which is given by:

$$T = a\beta^b[minutes] \tag{5.17}$$

where T is the average rain event duration in minutes, while β represents number of generated spikes within a specified event. Power-law coefficients, a and b, required in (5.17) are given in Table 5.7 from data sets obtained from Markov-generated and queue-generated rainfall events in Jimma. These results are the aftermath of the convergence of event duration statistics resulting from multiple simulations for several number of rain spikes. Results from the coefficients in Table 5.7 imply that outputs of rain event durations from Markov chain and queueing theory are closely related for drizzle and widespread events. However, for shower and thunderstorm events, Markov chain estimates for event duration are higher, compared to estimates from the queue process.

5.7.2 Comparison of PDFs Generated from Markov and Queue models with Actual Measurements

The PDF of any stochastic model provides adequate information rooted in the data by assessing frequency distribution and general statistical parameters such as mean and standard deviation. Thus, PDFs of rainfall rate time series from rain events over a period of one year (at 1 minute integration time) from measurements are compared with that generated from rainfall events using Markov chain and queue approaches for model validation.

Figure 5.24 shows the PDF of actual data and synthesized rainfall time series from Markov and queue models at Jimma. It is seen that the Markov and queue models PDF are closer statistical fits to the measured PDF. The consistency of these models with the actual measurements can be checked by considering the PDF parameters such as mean and standard deviations. The mean of measured, Markov model and queue models are: 10.28, 12.16 and 12.954 respectively, while their standard deviations are 19.4, 20.52 and 18.41 respectively. These validate the accuracy of these models by giving a reasonable representation of the rainfall measurements.

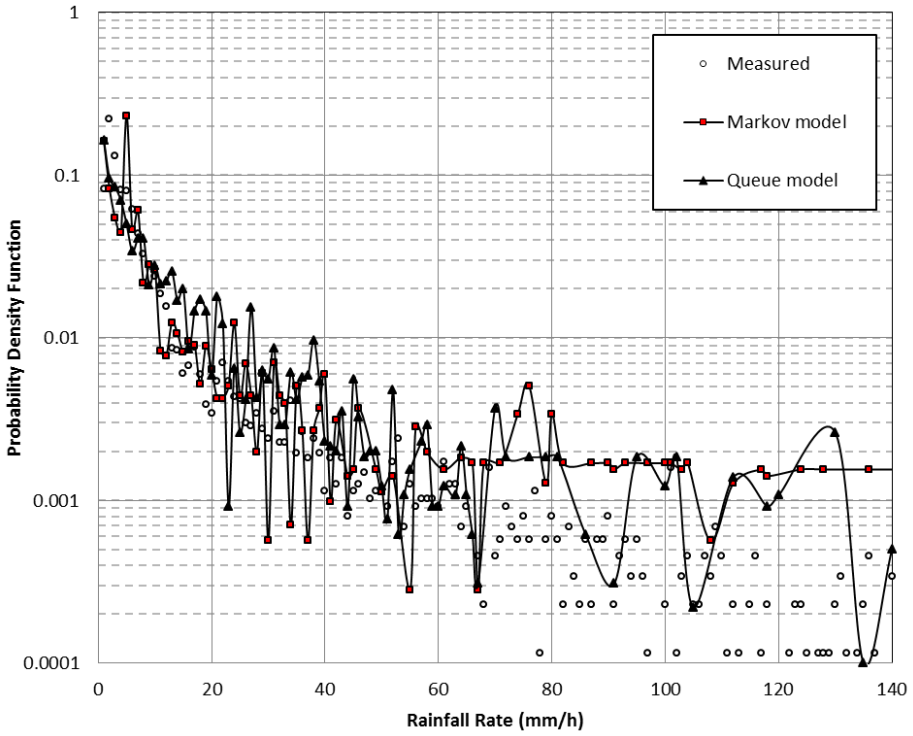

Figure 5-24: Comparison of the rainfall rate Probability Density Functions (PDFs) of data obtained from the proposed model and the actual measurements

5.7.3 Comparison of Queue and Markov Generated Rainfall Exceedance Distribution with Actual Measurements

Rainfall events vary throughout seasonal cycles leading to varying performance of communication systems on a yearly basis. Therefore, knowledge of rainfall rate exceedance distribution is a necessity for evaluating rain fade margin because it provides ample information on

the requirements needed for compensating time-varying rain attenuation at different availability indices. Therefore, graphical results in Figure 5.25 show the comparison of rainfall rate exceedance distributions between actual measurements at Jimma and the proposed Markov chain and queue models.

In Figure 5.25, rainfall exceedence curve for Markov model agrees with actual measurements for rain rates up to 60 mm/h. However, exceedance values obtained from queue generated are slightly higher than the actual measurements for rain rates up 35 mm/h. Generally, it is observed that there is good agreement with exceedance curve values from the proposed Markov-generated and queue-generated models with actual data distribution at 99.9% availability (0.1% outage probability) as seen in the Table 6. For instance, rainfall rate at 99.99% availability or 0.01% exceedance time ($R_{0.01}$) are found to be 122 mm/h, 119 mm/h and 124.5 mm/h for measured, Markov-generated and queue-generated respectively. At 99.9%, rain rate found to be 41 mm/h, 40.5 mm/h and 39 mm/h for measured, Markov generated and queue-generated respectively. Prediction from queue and Markov models are almost equal as the actual measurement of rainfall rate availability in Table 5.8.

Table 5.9 presents error analysis, resulting from comparison between the actual measurement and synthetic rainfall time series for PDF and rainfall exceedance curves, using $RMSE$ and χ^2 statistical tools. Overall error analysis shows that the performance of both queue and Markov chain models in rainfall synthesis compare well to the measured dataset. $RMSE$ values from PDF distributions are found to be 0.0215 and 0.0304 for Markov and queue models, respectively. Likewise, χ^2values are seen to be 0.644 and 0.6521 for Markov and queue models respectively.$RMSE$ values from percentage of time exceedance distributions are found to be 0.06954 and 0.0998 for Markov and queue models respectively, while calculated χ^2values are 0.58 and 0.78 respectively. The degree of freedom and significance level also affirm that both models are within acceptable ranges. From the foregoing, it is obvious that results obtained from both models are close and give a good representation of measured rainfall distributions at Jimma. However, the Markov approach proposed in this work presents an improvement (in terms of accuracy) over the queue approach, in replicating and predicting the time domain characteristics of random rain events over radio links at this location.

Table 5.8: Comparison of Rainfall Rate Exceedence Percentages from Actual Measurement and the Proposed Models at Jimma

% Exceedance	Rainfall Rate (mm/h)		
	Measured	Proposed Markov	Queue
0.01	122	119	124.5
0.1	41	40.5	39
1	4	3	2

Table 5.9: Error analysis of rainfall events from Markov chain and queueing models

Models	Rain Rate	Exceedance	PDF		DF	SL
	$RMSE$	χ^2	$RMSE$	χ^2	DF	SL
Markov Model*	0.06954	0.58	0.0214	0.644	62	81.381
Queue Model	0.099	0.782	0.0303	0.6521	62	81.381

*Proposed Markov model gives lower $RMSE$ and χ^2 values for rain rate exceedance and PDF

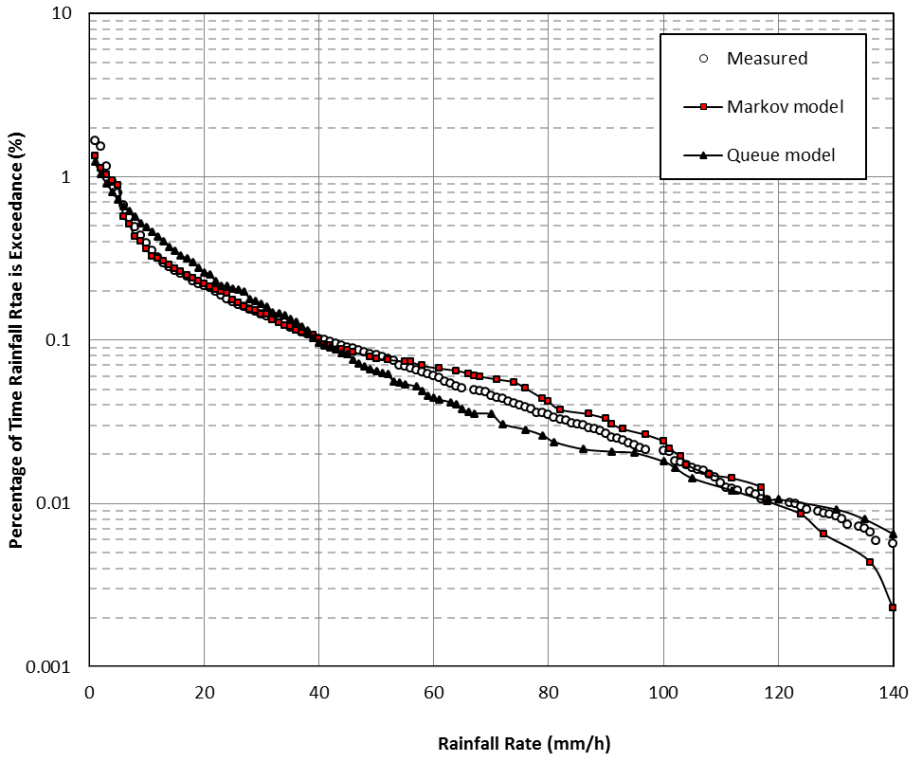

Figure 5-25: Comparison of Exceedence Distribution Curves of Rainfall Rate from the Proposed Model, Queue Model and Actual Measurement

5.8 Chapter Summary

In this chapter, Markov chain and queue models for the dynamic behaviour of rainfall rate spikes characterization for four rainfall regimes at Jimma, Ethiopia were presented. Rainfall time series data at one minute integration time have been classified into four rainfall regimes and the probability transition matrices of the regimes have been formed and seen to be ergodic. Steady state vectors show the percentage of occurrence probability of rainfall spikes increases (from drizzle to thunderstorm) regimes. From statistical measurements, the sojourn time of rainfall spike follows Erlang-k probability distribution. The MATLAB implementation of the synthetic generation of time series rainfall events from transition probability matrices, state vector and sojourn time has been developed. The principal queue parameters for the same location have been determined and the rainfall events are also generated from queueing theory model. The comparison of the actual measured and generated rainfall shows a good preservation of statistical characteristics. In the next chapter, the combined effect of clear-air and precipitation over radio links is investigated from received signal measurements.

Chapter 6

Attenuation Measurements from Received Signal Level of Terrestrial Line-of-Sight Link

6.1 Introduction

In the previous chapters, clear air and precipitation effects over wireless links were investigated, and rainfall and clear air radioclimatological parameters were derived. Attenuation of radio wave propagation can be empirically described from raindrop size, rainfall rate distribution, clear air radioclimatological parameters along the link, or from signal level measurements [14, 15, 138]. From several parameters contributing to a reliable radio network communication system, the outage probability (link availability) due to rainfall or multipath fading is a significant factor [139]. This is due to their strong influence on the fade margin required for line-of-sight link to perform satisfactory [140, 141]. If link is free from any obstruction or the diffraction fading , the fade depth depends on the amount of time in which radio network is unavailable during an average year [140].

In this chapter, an analysis of received signal level measurements for the terrestrial LOS link in between Addis Ababa and Furi is undertaken in collaboration with Ethiotelecom. At the carrier frequency of 11 GHz and link distance of 16.42 km, measurements were taken over a span of 10 months between the years 2015 and 2016 (June, July, August, September, October, November, December, January, February and March) with vertical

polarization. Measurements were based on the existing terrestrial link between Addis Ababa ($9.01^0N, 38.44^0E$) as the receiving site and Furi ($8.5258^0N, 38.41^0E$) as the transmitting station.

Different types of kernel density estimation have been applied to analyze the distribution of the measured signal level dataset. Monthly, seasonally, and yearly fade exceedance probabilities at different percentages of time for the link were analyzed. Finally, fade margin and outage probability from measured signal level and measured atmospheric parameters presented in chapter 3 were statistically compared.

6.2 Description of the link profile

The terrestrial Line-of-Sight like was between Addis Ababa at an azimuthal angle of 203.920 with an altitude of 2401 m above sea level and Furi at an azimuthal angle of 23.910 with altitude of 2842 m above sea level. The link is vertically polarized at operating frequency of 11 GHz. The height provides enough clearance as seen the path profile of Figure 6.1 for radio propagation network.

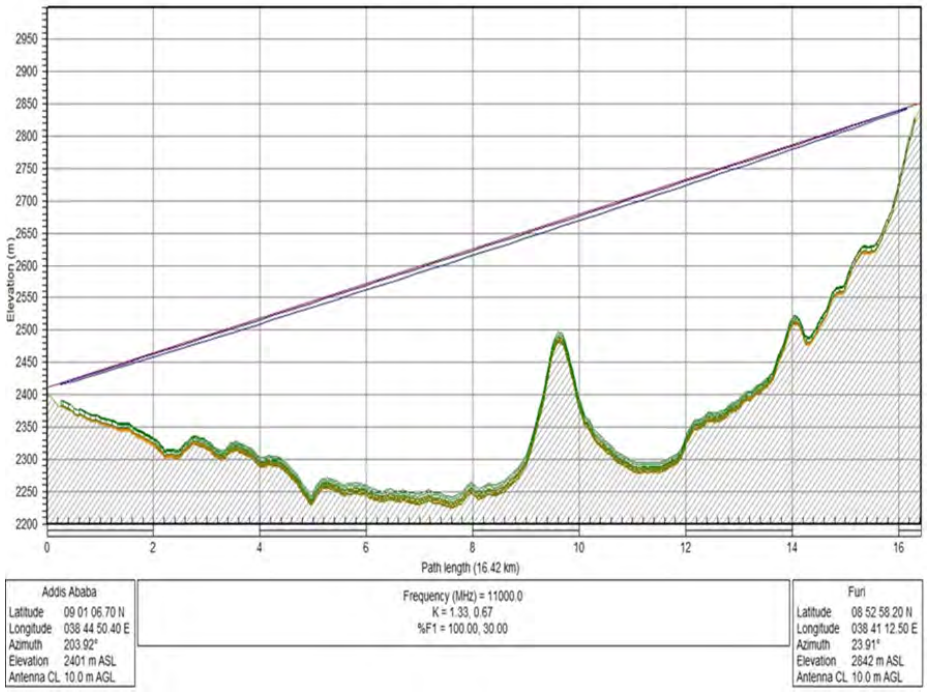

Figure 6-1: Path profile for 16.42 km terrestrial line-of- sight link between Furi and Addis Ababa

Table 6.1: link parameters for terrestrial line of sight networks

Parameters		link
	Addis Ababa	Furi
Elevation (m)	2401	2842
Latitude	09.01067^0N	08.52582^0N
Longitude	038.44504^0E	038.41125^0E
Antenna height(m)	10	10
Antenna gain (dBi)	42	42
Tx line unit loss(dB/100)	4.53	4.53
Tx line loss (dB)	0.91	0.91
Frequency(MHz)	11000	11000
Circuit branching loss (dB)	6.8	6.8
True azmuth (0)	203.92	23.91
Vertical angle	1.48	-1.59
Link distance (km)	16.42	
Free space loss (dB)	139.6	
Rx threshold level (dBm)	-76.2	
Effective frequency spacing (MHz)	21.7	
Atmospheric absorption loss (dB)	0.35	
Tx power (dBm)	30	

The performance analysis of terrestrial LOS radio link was undertaken depending on the calculations of the link budget. The link budget analyses involve the calculation of received signal level, fade margin and noise figure. Therefore, the expected received signal power,P_r was computed using (6.1):

$$P_r = P_t + G_{tx} + G_{rx} - FSL - L \tag{6.1}$$

Where P_t is the transmitter power output at the Antenna input. This is the amount of microwave carrier output power, usually expressed in dBm; L is losses due to the presence of atmospheric gases, vegetation, buildings, clouds and fogs; G_{tx} = Transmit Antenna gain, G_{rx} = Receive Antenna gain, FSL = Free space path loss.

The performance of a radio link is determined by the percentage of the time the signal will be below the threshold of the radio receiver relative to the total time period. Therefore the fade margin, which is the difference between the receiver nominal signal level and the receiver threshold level, has to be calculated as follow:

$$FadeMargin = RSL - R_{XTH} \tag{6.2}$$

Here, RSL is the received signal level and R_{XTH} is the receiver threshold.

The calculated received signal power P_r at the receiver end of the links using a transmitting power of 30 dBm is -50.43 dBm for the link between Addis Ababa and Furi if there is no rain that causes attenuation, no losses because of water vapour and fog, no multipath and diffraction fading. However, because of the other different cause of losses, the real signal levels received goes below this ideal values at both locations.

6.3 Kernel Density Estimation

Kernel density estimation is a method used to estimate the density function of non-parametric distribution directly from the dataset. The most common data characterizing non-parametric models are histograms. However, histograms are relayed on bandwidth of bin and also discontinues between end points [142]. Selecting large size of bin in histogram curve fitting can describe only some of the data points that results in a missing of data elements. On the other hand, choosing small bins width maybe end with turning out of data points. Kernel density estimation were presented to overcome histogram's drawback by introducing the smoothing parameter (h) which determine how best the dataset fit with the appropriate models [142]. The kernel variable estimator PDF $f(k)$ is given by the following equations.

$$f(k) = \frac{1}{nh} \sum_{i=1}^{n} K\left(\frac{K - x_i}{h}\right) \tag{6.3}$$

where h is the smoothing parameter, n is the number of data points, K is the kernel function and x_i is the i^{th} data point.

Kernel properties

$$\int_{-\infty}^{+\infty} K(k)\, dk = 1 \tag{6.4}$$

$$\int_{-\infty}^{+\infty} kK(k)\, dk = 0 \tag{6.5}$$

$$\int_{-\infty}^{+\infty} k^2 K(k)\, dk > 0 \tag{6.6}$$

6.3.1 Bandwidth selection for kernel density estimators

Effectiveness of kernel density estimation is based on the choice of the smoothing parameter. The smoothing parameter value determines the variance and biasness of the estimated model. If the chosen smoothing parameter value is very small compared to the optimal one, the kernel model is usually under- smoothed and very spiky, and hence, difficult to interpret. On the other hand, if the smoothing parameter value is high, the resulting kernel model is over-smoothed, and therefore obscures the data structure. Practically, the choice of an optimal smoothing parameter is done based on the number of data samples, kernel function, as well as their variance [104, 143]. The optimal bandwidths and efficiencies of some common kernel functions are given below. The value of sample variance δ is estimated from the sample data with k observations.

Types of Kernel function and their corresponding equations [144].

a. Box (rectangular)

$$K(k) = \begin{cases} 0.5, & -1 \leq k \leq 1 \\ 0, & otherwise \end{cases} \tag{6.7}$$

Rectangular is 93 % efficiency with Optimal window width of $\frac{1.84\delta}{n^5}$

b. Epanechnikov

Epanechnikov is 100% efficiency with Optimal window width of $\frac{2.34\delta}{n^5}$

$$K(k) = \begin{cases} \frac{3(1-0.2k^2)}{\sqrt{80}}, & -\sqrt{5} \leq k \leq \sqrt{5} \\ 0, & otherwise \end{cases} \tag{6.8}$$

c. Normal

$$K(k) = \frac{e^{-\frac{k}{2}^2}}{\sqrt{2\pi}}, \quad -\infty \leq k \leq \infty \tag{6.9}$$

Normal is 95.1% efficiency with Optimal window width of $\frac{1.06\delta}{n^5}$

d. Triangular

$$K(k) = \begin{cases} \frac{15(1-k)}{16}, & -1 \leq k \leq 1 \\ 0, & otherwise \end{cases} \tag{6.10}$$

Triangular is 98.6% efficient with optimal window width of $\frac{2.56\delta}{n^5}$

In this chapter, four kernels functions seen in equation (6.7 - 6.10) are applied in the derivation of simple non-parametric models that expresses the received signal level characteristics in the mathematical forms. These models are optimized through an error - based optimization procedure. The determination of the optimum kernel models is based on the optimal choice of the bandwidth. Different types of kernel models are used to fit the probability density function of received signal level dataset. To test the best-fit of probability density function (pdf) of the proposed kernel model with respect to the pdf obtained from measured data, the root-mean-square error $RMSE$ statistic is applied and determined using the relations in (5.8).

6.4 Signal Level Analysis

From Table 6.1, it is observed that the receiver threshold signal level value is -76.2 dBm. During non-fading (under clear-air conditions), the averaged received signal level threshold value is -53.344 dBm. Therefore, by applying (6.2), the average fade margin is equal to -22.856 dBm. This implies that, if the fade depth (A) is between 0 and -22.856 dBm, it implies faded reception due to poor signal level. If the fade depth (A) is less than -22.586 dBm, it will results in network outage.

The received signal level measurement was conducted for 10 months from June 2015 to March 2016, however, the data is not available for the months of April and May. The overall measurement days are 250 as seen in the Table 6.2. This data was processed and analysed for each month. For the analysis of signal level, we first determine the minimum threshold received signal level (RSL) value above which no fading observed for all months under study. If the signal levels value is less than the minimum threshold, it refers to faded signal. Therefore, the faded signal levels are classified into five various fade depth (A) levels as follows: $0.1 \leq$ A(dB)$\leq$ 10 dB; 10.1 $\leq$A(dB) $\leq$ 15 dB; 15.1 $\leq$ A(dB) $\leq$ 20 dB; 20.1 $\leq$ A(dB) $\leq$ 23 dB; $>$ 23 A(dB).

Table 6.2 shows that, from the total 22,999 minutes of signal level measurements, the measured signal level is less than the average non-fading value (-53.344 dBm) for 9,189 minutes. this implies that for 39.95% of the time, fading of the signal occurs over this radio link.

Table 6.2: Monthly Measurement Information

Months	Days	Sample size	Total fading time	Average Non-fading RSL
June	14	1344	438	-53.39
July	31	2976	654	-53.32
August	31	2976	575	-53.22
September	30	2880	1019	-53.56
October	27	2592	1413	-53.49
November	28	2688	942	-53.32
December	26	2496	1190	-53.16
January	25	1399	1117	-53.07
February	18	1728	604	-53.386
March	20	1920	1237	-53.527
Total	250	22999	9088	

From Table 6.3, it is observed that, from the total fading time (9,189 minutes), the fade depth (A) is between -0.1 and -10 dBm for 9,088 minutes, between -10.1 and -15 dBm for 49 minutes, between -15.1 and -20 dBm for 24 minutes, between 20.1 and -23 dBm for 12 minutes, and less than -23 dBm for 7 minutes.

Table 6.4 shows the percentage of time for which fade depths (A) occur from the total measurement for each month calculated using (6.11)

Using equation (6.11), results in Table 6.4 are obtained for each fade depth level.

$$P(A \geq F_k) = \frac{F_n}{T_n} * 100\% \tag{6.11}$$

where: $P(A)$ probability of percentage of time certain fade depth A(dB) exceeded , A is any fade depth level (dB),F_k is the fade depth level being analyzed (dB), F_n is the total faded minutes for the fade depth under analysis (mins), and T_n is the total faded minutes for the month being analysed (minutes).

According to Table 6.5, the percentages of fade depth A obtained from measurements are classified into three network functionalities namely: available, slightly available and deep fading. Table 6.5 shows that the network outage is observed in the months of July, August and September. This is indicated that intense rainfall in August and July which results in lower percentages of network availability whereas, during the dry months of October, November and December, high percentages of network availability are observed.

Table 6.3: Total Measurement time (min) of Fade Depths for every months of the Year

	Total	measured	time at	different	fade depth
Months	0.1-10 dB	10.1-15 dB	15.1-20 dB	20.1-23 dB	$>$ 23 dB
June	432	3	2	1	0
July	631	13	5	2	3
August	545	17	8	2	3
September	996	10	8	4	1
October	1412	1	0		0
November	942	0	0	0	0
December	1190	0	0	0	0
January	1115	2	0	0	0
February	602	1	1	1	0
March	1223 2	0	2	0	0
Total	908	49	24	12	7

Table 6.4: Percentage of Time P(A) that a Fade Depth A(dB) is Exceeded from the Total Measurement time for whole year

Percentage	of Time	exceeded at	different	fade	depth(%)
Months	0.1-10	10.1-15	15.1-20	20.1-23	$>$ 23 dB
June	98.627	0.685	0.4566	0.2283	0
July	96.485	1.9877	0.7645	0.306	0
August	94.775	2.956	1.3913	0.348	0.5217
September	97.7426	0.98135	0.785	0.3925	0.098
October	99.93	0.7785	0	0	0
November	100	0	0	0	0
December	100	0	0	0	0
January	99.821	0.179	0	0	0
February	99.669	0.165	0.1655	0	0
March	99.8383	0	0	0.1617	0

Table 6.5: Percentage of Exceedance Probabilities at different fade depths for whole year

Months	Percentage of Available	time of network Slightly Available	availability(%) Deep fading
June	96.117	3.6516	0
July	87.615	11.9282	0.306
August	84.34	15.1306	0.5217
September	94.9946	4.90685	0.098
October	99.7185	0.0707	0
November	100	0	0
December	99.91576	0.084	0
January	99.015	0.9847	0
February	98.3443	1.6545	0
March	98.221	0.08084	0

6.5 Seasonal Signal Level Analysis

Based on the average trends of rainfall and the weather, Ethiopia has four seasons namely: Summer, Autumn, Winter, and Spring [145]. Summer includes June, July, and August. This season experiences heavy rainfall. Autumn covers months of September, October, and November. Winter has months of December, January, and February. Winter is a dry season in Ethiopia with frost in morning specially in January. The last season is Spring that covers the months of March, April, and May.This season has occasional short rainfall events.

6.5.1 Analysis of Signal Level for the Summer Season

Figure 6.2 shows received signal level (RSL) measurements of 4 typical days, where deep fading is noticed, in summer. It is observed that there are fading periods on these days during which the network is severely affected by rainfall. For instance, on 19 July 2015, network outage is observed between 255 and 268 minutes during which the signal level fails below receiver threshold -76.2 dBm. Generally, it is seen that network outages occur for some days in this season due to intense rainfall.

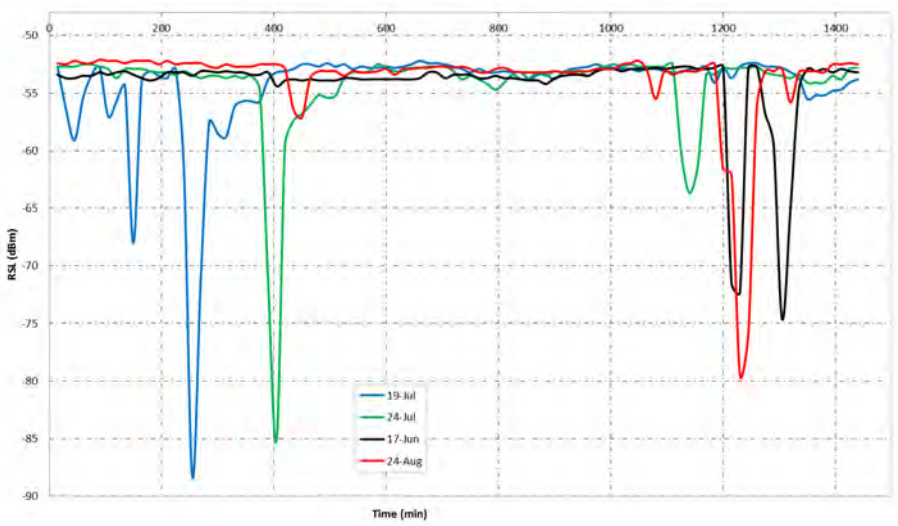

Figure 6-2: Received Signal Level Variation over 24 hours, Summer 2015, Addis Ababa, Ethiopia

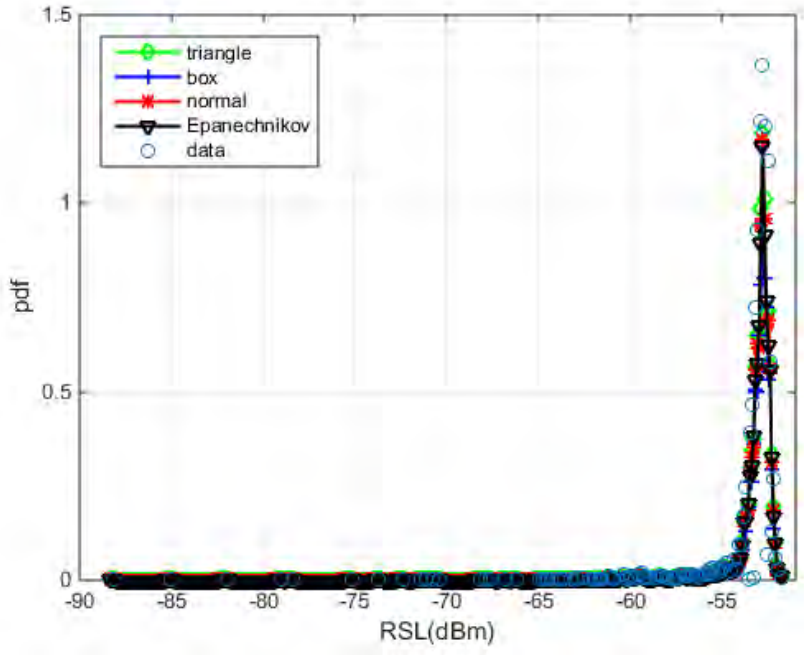

Figure 6-3: Comparison of the kernel model and Measurements for the RSL obtained Summer 2015

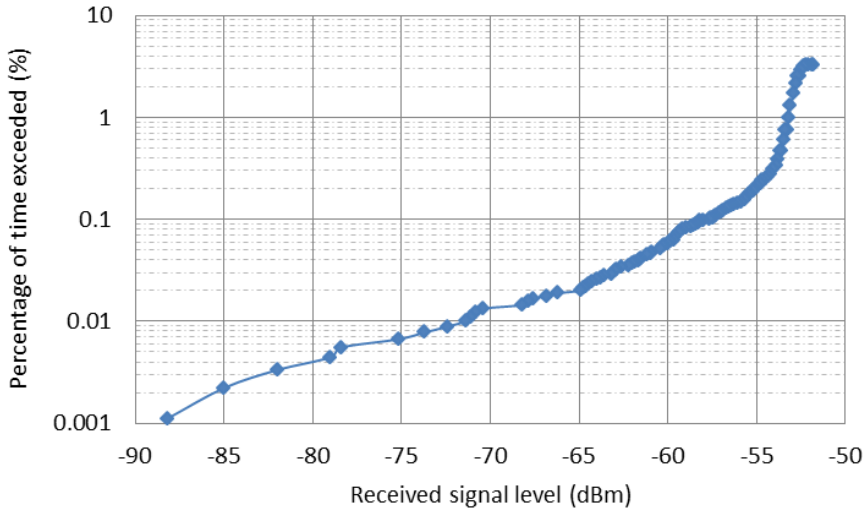

Figure 6-4: Fade depth at different percentages of time exceedence for RSL, Summer 2015

Figure 6.3 presents the PDF of RSL measurements in summer 2015 and their four kernel model approximations. It is seen from the figure that the kernel density estimators closely fit to the measured one. Error analysis also shows that the four kernel models are closer to one another. The average non-fading threshold of the RSL value for summer season, obtained from the corresponding probability density function, is found to be -53.31 dBm. Therefore, RSL values lower than -53.31 dBm are considered as fading. On the other hand, Table 6.6 gives optimum bandwidth values for summer season based on $RMSE$ analysis, and the best kernel model is found to be rectangular at $RMSE$ value of 0.0057.

Figure 6.4 presents the percentage of time of exceedance versus received signal level for this season. Appropriate fade depth of RSL for summer, calculated from cumulative distribution of the received signal level measurements, at 0.01 % outage probability (99.99 % availability) is -70.6 dBm, this is 17.29 dB lower than the average non-fading threshold value. Furthermore, at 99.9% availability (0.1 % outage probability), RSL is given as -57.4 dBm, which again 4.09 dBm lower than the average non-fading threshold value.

6.5.2 Analysis of Signal Level for the Autumn Season

Similar methods was considered for analysis of signal level in the autumn season. Figure 6.5 illustrates received signal level (RSL) measurements of 3 typical days (1 day from the

Table 6.6: Kernel model error analysis for Summer 2015

Kernel model	Optimum bandwidth (h)	RMSE
Triangular	0.115	0.0066
Rectangular	0.043	0.0057
Epanechnikov	0.092	0.0062
Gaussian	0.1003	0.0063

3 months of the season), where fading are noticed, in this season. It is possible to observe from this figure that fading periods are observed but, network outage is not seen during which the signal level below the receiver threshold. Generally, it is noticed from the figure 6.5, fading is noticed for some days ot this season.

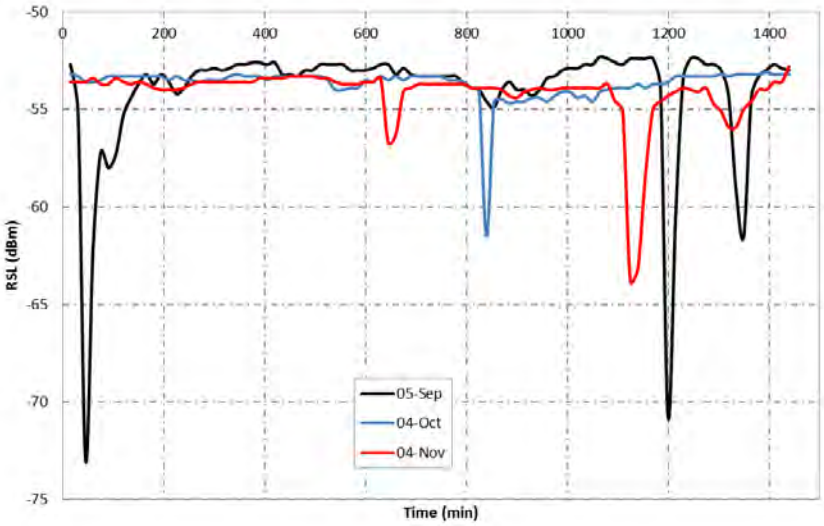

Figure 6-5: Received Signal Level Variation over 24 hours, Autumn 2015, Addis Ababa, Ethiopia

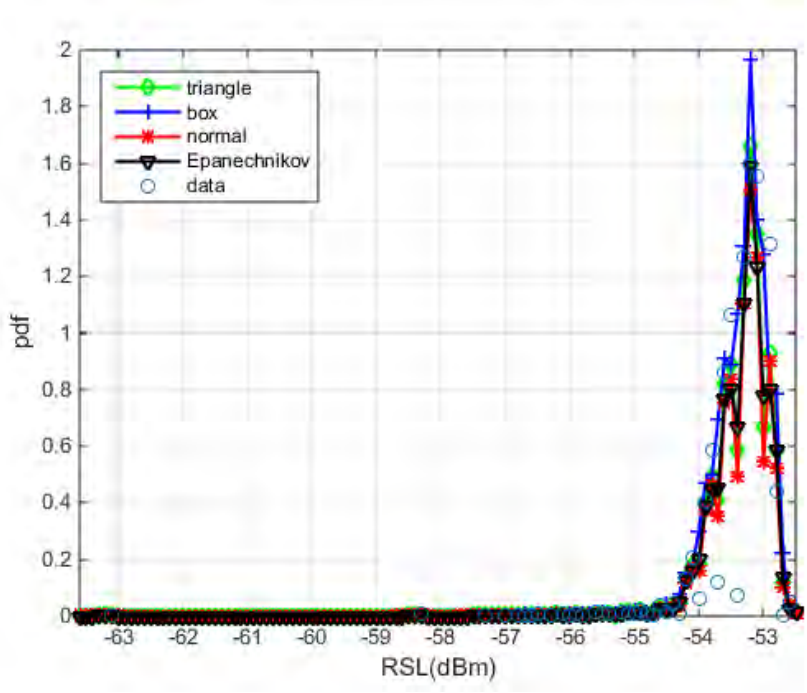

Figure 6-6: Comparison of the kernel model and Measurements for the RSL obtained in Autumn 2015

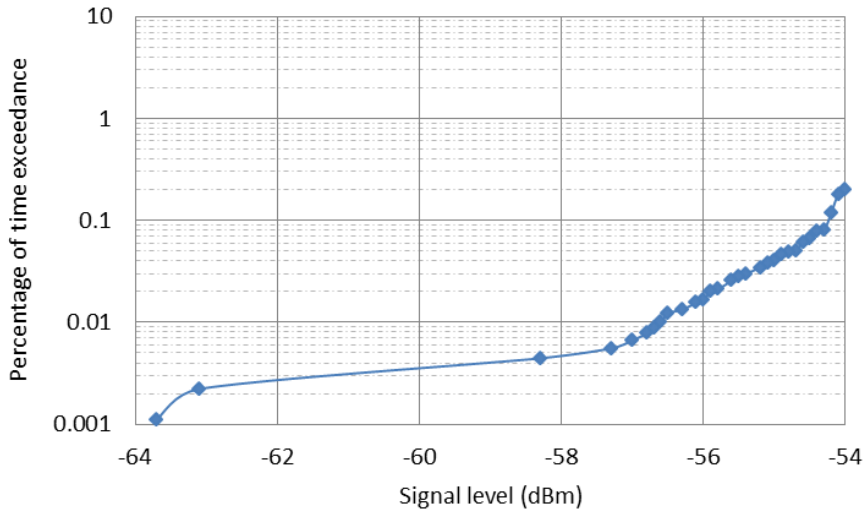

Figure 6-7: Fade depth at different percentage of time exceedence for RSL, Autumn 2015

Figure 6.6 shows the probability density function of RSL measurements in October 2015 and four kernel model approximations. It is seen from the figure that the kernel density

Table 6.7: Kernel model error analysis for Autumn 2015

Kernel model	Optimum bandwidth (h)	RMSE
Triangular	0.0662	0.0048
Rectangular	0.0573	0.0044
Epanechnikov	0.0671	0.005
Gaussian	0.058	0.0046

estimators closely fit to the measured one. Error analysis also shows that the four kernel models are closer to one another. The average non-fading threshold value of the RSL value for this season, obtained from the corresponding probability density function, is found to be -53.4566 dBm. RSL values lower than -53.4566 dBm are considered as fading. On the other hand, Table 6.7 gives optimum bandwidth values for autumn based on $RMSE$ analysis, and the best kernel model is found to be Rectangular at $RMSE$ value of 0.0044.

Figure 6.7 presents the percentage of time of exceedance versus received signal level. It is observed that at 0.01 % outage probability (99.99 % availability) the signal level is -56.6 dBm which is 3.143 dBm lower than the threshold value. At 99.9 % availability (0.1 % outage probability) the received signal level is -54.4 dBm that is -0.9434 dBm lower than the average non fading signal level value.

6.5.3 Analysis of Signal Level for the Winter Season

The same procedure was adopted for the analysis of signal level in the Winter season. Figure 6.8 presents received signal level (RSL) measurements of 3 typical days in this season (on 08 December, 17 January and 17 February). It is possible to observe from this figure that there is almost no day during which a significant fading period observed.This is because of the fact that there is almost no rainfall occurrence in the winter season over most part of Ethiopia. Generally, it is noticed from the figure 6.8, there is no much fading during this dry season.

Figure 6.9 shows the probability density function of RSL measurements in winter and four kernel model approximations. It is observed from the figure that the kernel density estimators closely fit to the measured one. Error analysis also shows that the four kernel models are closer to one another. The average non-fading threshold of the RSL value for this season, obtained from the corresponding probability density function, is found to be -53.205 dBm. RSL values lower than -53.205 dBm are considered as fading. On the other

hand, Table 6.8 gives optimum bandwidth values for winter based on $RMSE$ analysis, and the best kernel model is found to be triangular at $RMSE$ value of 0.0052.

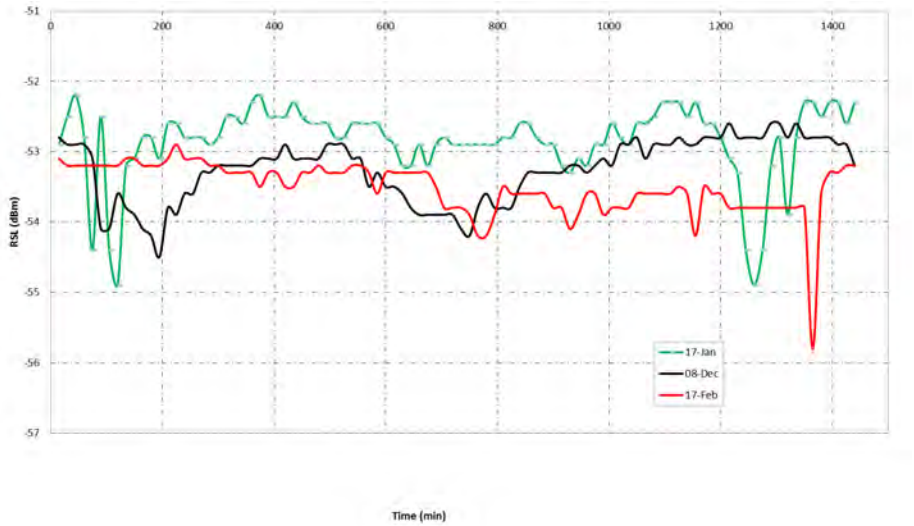

Figure 6-8: Received Signal Level Variation over 24 hours, Winter, Addis Ababa, Ethiopia

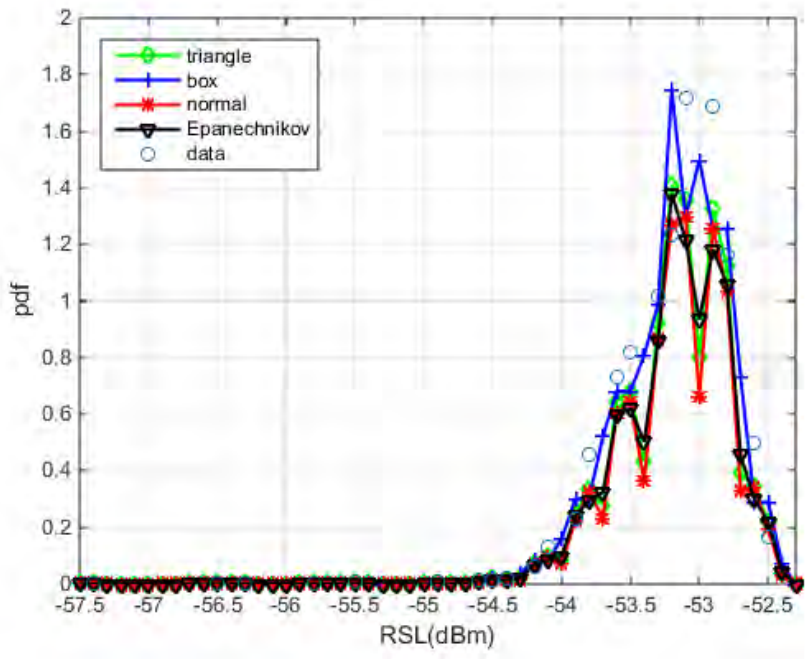

Figure 6-9: Comparison of the kernel model and Measurements for the RSL obtained in Winter Season

Table 6.8: Kernel model error analysis for Winter Season

Kernel model	Optimum bandwidth (h)	RMSE
Triangular	0.0983	0.0052
Rectangular	0.0951	0.0056
Epanechnikov	0.0973	0.0053
Gaussian	0.1017	0.0059

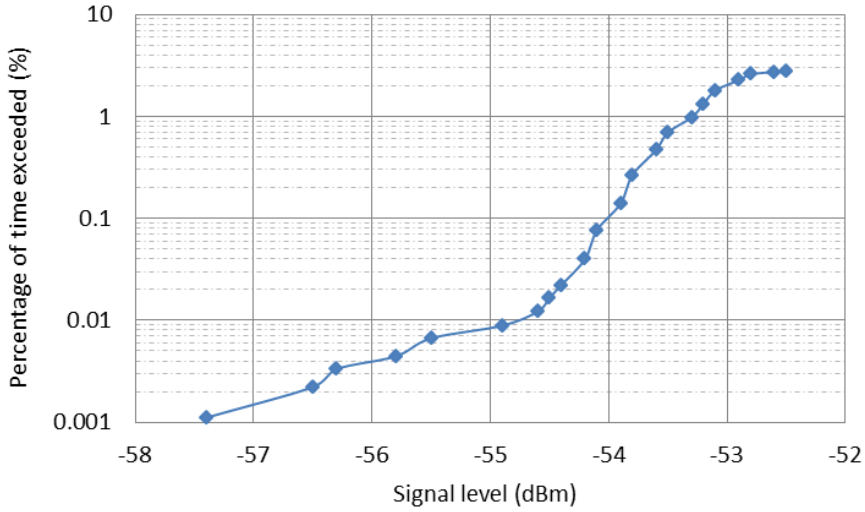

Figure 6-10: Fade depth at different percentage of time exceedence for RSL, Winter Season

Figure 6.10 presents the percentage of time of exceedance versus received signal level. It is observed that at 0.01 % outage probability (99.99 % availability) the signal level is -54.7 dBm this is -1.495 dBm lower than the non-fading threshold value. At 99.9 % availability (0.1 % outage probability) the received signal level is -53.9 dBm.

6.5.4 Analysis of Signal Level for the Spring Season 2016

Similar technique was applied for analysis of signal level in the Spring season,2016. Figure 6.11 presents received signal level (RSL) measurements of 3 days in march. It is possible to observe from this figure that there is a few days during which fading period observed this is because of the fact that there is little rainfall occur in March over most part of Ethiopia. Generally, it is noticed from the figure 6.11, fading is seen in this season, however, network outage is not observed.

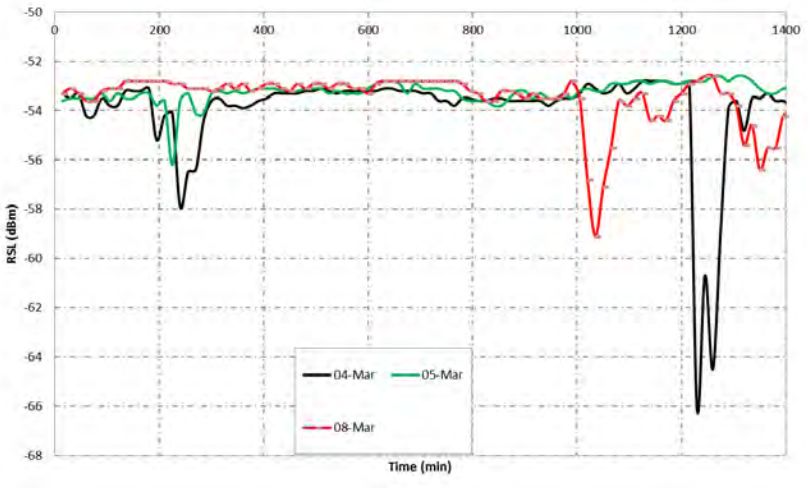

Figure 6-11: Received Signal Level Variation over 24 hours, March 2016, Addis Ababa, Ethiopia

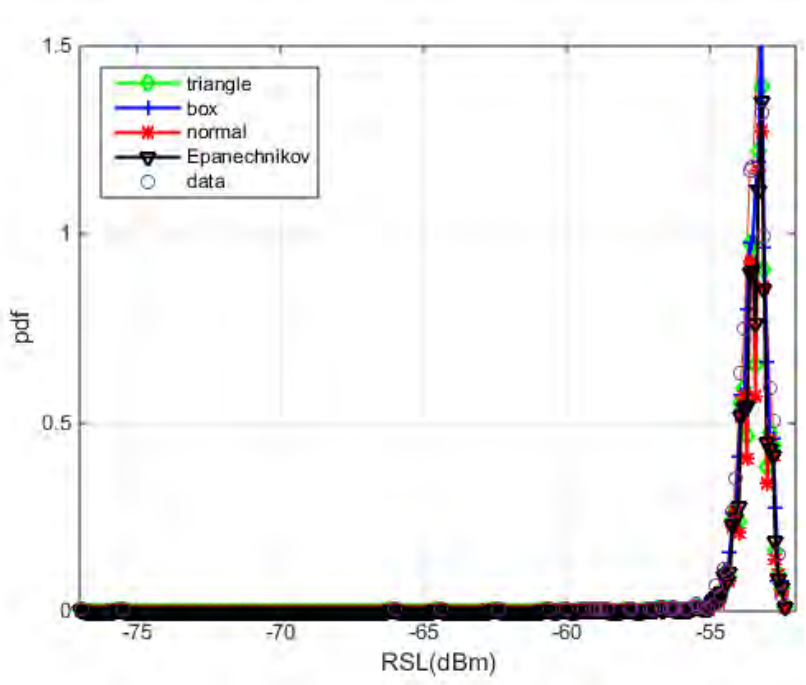

Figure 6-12: Comparison of the kernel model and Measurements for the RSL obtained in March 2016

Table 6.9: Kernel model error analysis for March 2016

Kernel model	Optimum bandwidth (h)	RMSE
Triangular	0.0715	0.0048
Rectangular	0.063	0.0046
Epanechnikov	0.0692	0.0051
Gaussian	0.0903	0.0055

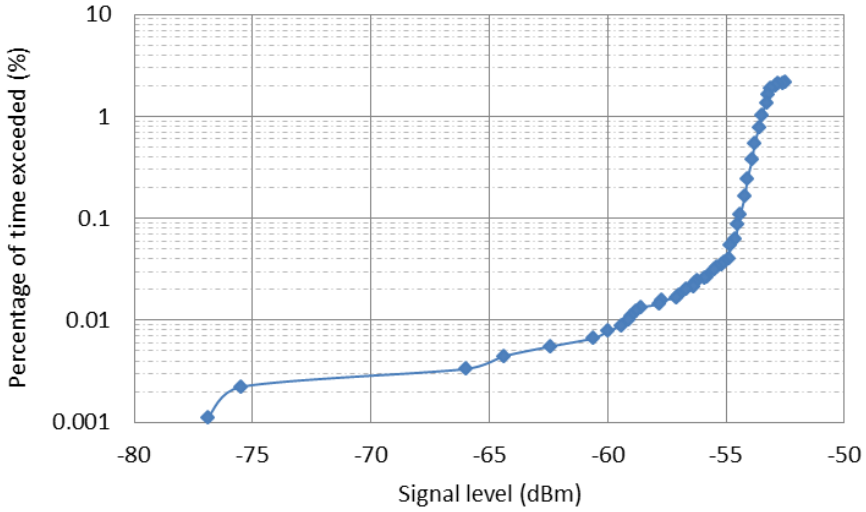

Figure 6-13: Fade depth at different percentage of time exceedence for RSL, March 2016

Figure 6.12 gives the probability density function of RSL measurements in Spring, 2016 and four kernel model approximations. It is observed from the figure that the kernel density estimators closely fit to the measured one. Error analysis also shows that the four kernel models are closer to one another. The average non-fading threshold of the RSL value for this season, obtained from the corresponding probability density function, is found to be -53.527 dBm. RSL values lower than -53.527 dBm are considered as fading. On the other hand, Table 6.9 gives optimum bandwidth values for March based on $RMSE$ analysis, and the best kernel model is found to be rectangular at $RMSE$ value of 0.0046.

Figure 6.13 presents the percentage of time of exceedance versus received signal level. It is observed that at 0.01 % outage probability (99.99 % availability) the signal level is -58.8 dBm which is -5.273 dBm lower than the average non-fading threshold value. At 99.9 % availability (0.1 % outage probability) the received signal level is -54.4 dBm.

Table 6.10: Monthly fade margin at 11 GHz and 16.42 km link distance between Addis Ababa and Furi

Months	Fade margin	at different	percentage of	availability (dB)
	99 %	99.9 %	99.99 %	99.999 %
June	0.7	2.3	9.2	22.4
July	1.3	5.3	19.3	36.4
August	6.3	6.3	17.8	27.8
September	1.5	3.5	18.4	28.8
October	0.8	1.5	2.7	8.7
November	0.8	1.6	3.9	11.1
December	0.4	1.6	2.4	4.9
January	1	2	5.9	14.4
February	0.8	1.4	5.9	16.3
March	0.8	1.9	6.6	24.4

6.6 Fade Margin and Link Availability Analysis

The monthly distribution of percentage of time exceeded gives the required allowance needed for radio wave propagation for reliable radio communication system. Therefore, the outage probability or link availability of wireless communication systems at microwave and millimeteric bands can be predicted for an averaged year [139, 141]. From the exceedence distribution Tables shown in section 6.4, fade margin values are determined at different percentage of time for ten months in Ethiopia.

Tables 6.10 gives the measured monthly fade margin values in dB at 11 GHz for radio link 16.42 km length between Addis Ababa and Furi. In this Table, fade depth that can guarantee different percentage of link availabilities for each month are presented at 99%, 99.9%, 99.99% and 9.999%. According to the ITU-R [13] recommendations, the 0.01% exceedance attenuation value at 0.01% give 99.99% availability on a radio communication link. Hence, it is observed that the month of July requires higher fade margin of up to 19.3 dB to guarantee 99.99% availability.

6.7 Clear-air Signal Level Measurement Analysis

In this section, signal attenuation measurements over a period of 2015 and 2016 are presented to model clear-air fading between Addis Ababa and Furi link. For that purpose, attenuation events caused by rainfall with significant values of fading were removed from data processing.

The temporal variation of the received signal level during signal propagation is well defined by the specific shape of the signal fluctuations of maximum and minimum propagating signals. Figure 6.14 shows the sample daily variation of signal level. From the Figure, it is seen that during clear-air conditions the RSL varies randomly and attenuation tends to occur more during day. This may be due to industrial fog produced around Addis Ababa and Furi (along the link).

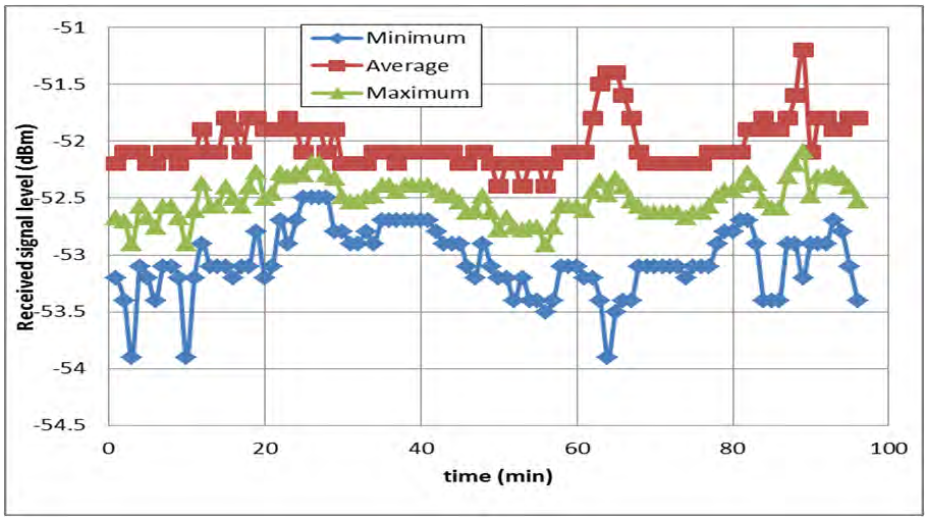

Figure 6-14: Sample Clear-air signal level variation at over 24 hours, 17 June 2015 for Addis Ababa to Furi link

Table 6.11, gives the values from different types of kernel models, it is noted that all kernel techniques perform well; however, the choice of the kernel method to apply for a particular set of data points is only driven by some error-based mechanism.

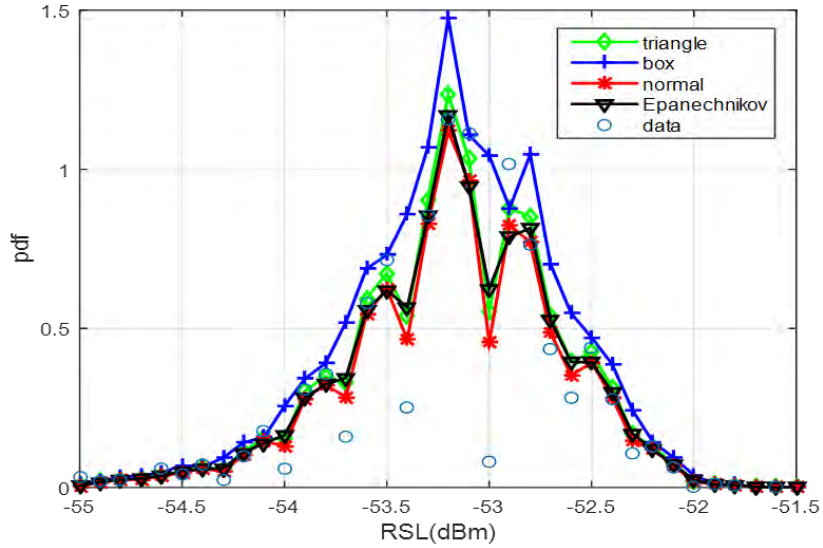

Figure 6-15: Clear-air minimum received signal level

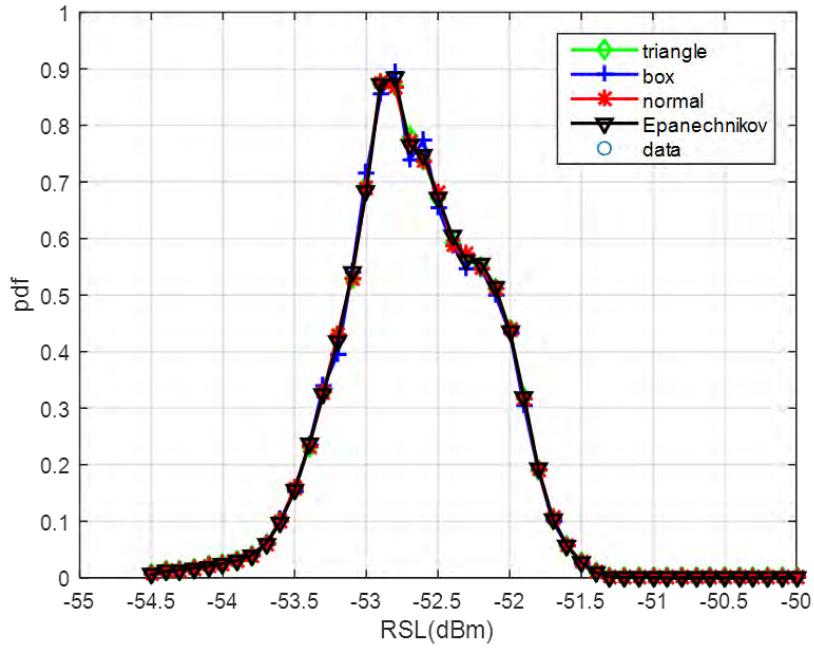

Figure 6-16: Clear-air average received signal level

Table 6.11: Kernel density comparisons based on RMSE for different values of smoothing parameters

RSL	h	Rectangular	Epanechnikov	Normal	Triangle
Minimum	0.063	0.255	0.219	0.092	0.19
	0.071	0.28	0.25	0.13	0.21
	0.083	0.31	0.29	0.24	0.25
Average	0.063	0.02	0.13	0.09	0.41
	0.071	0.056	0.055	0.051	0.059
	0.083	0.18	0.25	0.25	0.22
Maximum	0.063	0.28	0.33	0.26	0.27
	0.071	0.51	0.27	0.24	0.31
	0.083	0.247	0.254	0.234	0.22

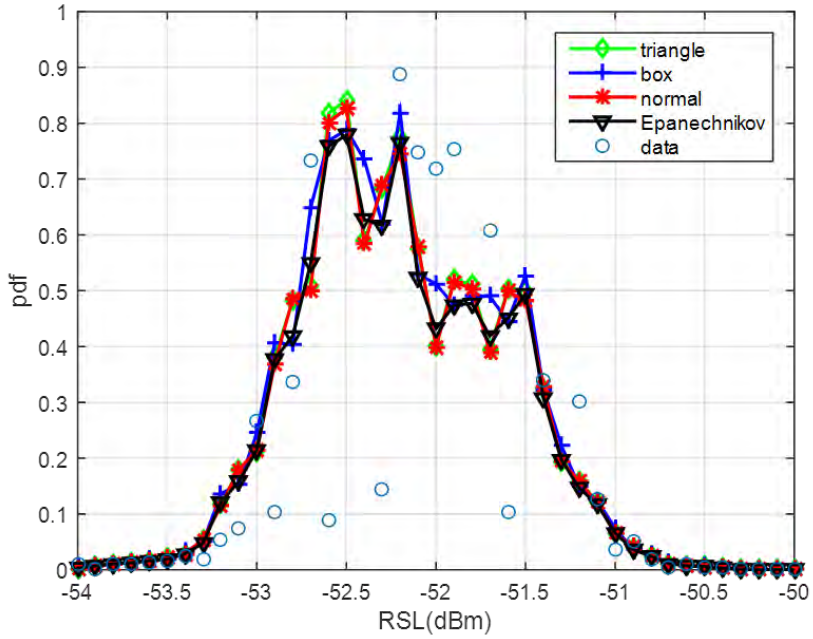

Figure 6-17: Clear-air maximum received signal level

Therefore, statistical distribution results from error analysis using (5.8) are shown in Table 6.11. Three values of the smoothing parameter are discussed in each case and the one which produces the least error is the best choice of the smoothing parameter. The results show that smoothing parameter values around the optimal value are very similar in shape and characteristics, thus, the only way to separate them is by applying error analysis. From Figures 6.15, 6.16, 6.18 the best kernel models for average is box at the optimum window

width, h of 0.071. For minimum received signal level, the best kernel fit is normal with an optimum window width of 0.063. Finally, for maximum received signal level, the kernel model is epanechnikov with an optimum window width of 0.083.

6.8 Comparison of Signal Level Measurement of Percentage of Time Exceeded with ITU-R Exceedence.

Figure 6.18 shows cumulative distributions of attenuations due to clear air fading for minimum, average and maximum received signal levels. Results from measurements show that the minimum received signal gives high amount of attenuation over varying exceedance probability. Predicted fade depth using ITU-R 530-15 nearly matches exceedance probabilities result with measured minimum received signal level as summarized in Table 6.12.

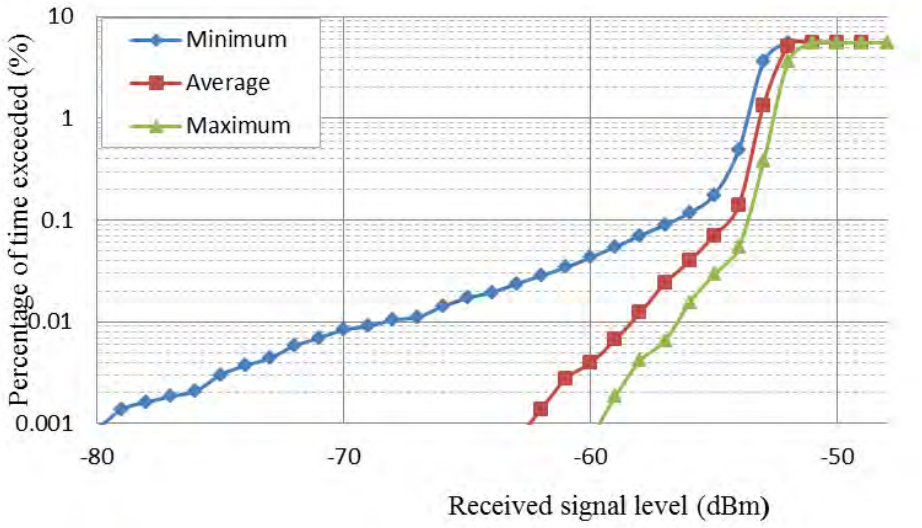

Figure 6-18: Clear air attenuation against different percentage of time exceedance

6.9 Chapter Summary

In this chapter, an extensive analysis of received signal level measurement over a LOS link between Addis Ababa and Furi was presented. The measurement was conducted for a period of ten months from June 2015 to March 2016 at operating frequency of 11 GHz and link

Table 6.12: Comparison of fade margin of measurements and ITU-R prediction

	Fade margin at different percentage of outage probability (dB) 0.001 %	0.01 %	0.1 %	1 %
ITU-R	26.5	16.5	6.5	-3.5
Minimum	29	18.1	5.1	2.7
Maximum	10.5	5.2	3.6	1.4
Average	12.9	8.1	4.5	2

distance of 16.4 km. The analysis has been done in two phases. The first phase was done monthly, and the second phase was done seasonal for all measurement periods.

Received signal level variation over 24 hours was obtained for each month. The minimum threshold value was predicted from probability density function for each season. The four kernel density estimator are fit to the measured probability density function are determined for each season. It is also observed that the error value for the four kernel models and the optimum bandwidth values are obtained for each season. the percentage of time of exceedance versus received signal level also calculated. The percentage signal fade levels were divided into three groups and analysed for application in LOS radio links in each month as available, slightly available and deep fading .

Chapter 7

Conclusions and Recommendations

7.1 Conclusions

7.1.1 Introduction

Wireless communication systems at microwave and millimetric wave bands are affected by atmospheric conditions. In this regard, the main concerns of telecommunication companies, scientists and practitioner engineers are the frequency and time elapsed of communication system interruptions due to rain and clear air conditions. Consequently, performance prediction of wireless links, based on the assessment of multipath fading for clear-air and attenuations for rainy conditions is essential. Rainfall attenuation plays a substantial role in radio link design at higher frequency bands. Attenuations due to rainfall and clear-air can be determined directly from signal measurements or estimated from rainfall rate, rain drop-size distributions and radio climatological parameters. Several models have been established to quantify and forecast the availability and outage probability of networks over a certain period of time in different regions of the world. However, there is no such study under taken to propose radio wave propagation models for Ethiopia. Currently, Ethiotelecom employs the ITU-R models to determine link budget requirements, however, this study have shown that under precipitation these models in Ethiopia are underestimated. To this end, this thesis has dealt with the analysis and modeling of precipitation and clear-air atmospheric parameters that contribute to wireless network outages in the Horn of Africa .This thesis has employed different approaches in chapters 3, 4, 5 and 6, and this section, hereby, discusses the conclusions drawn.

7.1.2 Chapter Three - Clear-Air Multipath Fading Due to Radio Climatological Parameters for Microwave Links in Ethiopia

In this thesis, multipath fading is predicted from radio-climatological parameters for different Ethiopian locations. From the dataset, refractivity gradient, refractivity in the first 100 m above the ground was determined, thereafter; the geo-climatic factor K was computed for various sites of Ethiopia. It is seen that K caters for climate characteristics in multipath fading distribution, with monthly variation in a year. The results also present that in August, refractivity is maximum and Geo-climatic factor K value is highest. This is because of the fact that high rain fall and humidity are experienced in August over various locations of Ethiopia. The fade depth for varies percentage of outage probability are estimated for the existing terrestrial Line-of-Sight links in four Ethiopian sites applying ITU-R P530-15 model; Diredawa gives the highest value of fade margin followed by Jimma, Mekele and Addis Ababa. Finally, the fade depth at different % time exceedance was estimated.

7.1.3 Chapter Four - Rainfall Rate and Attenuation Performance Analysis at Microwave and Millimeter Wave Bands for the Design of Terrestrial Line-of-Sight Radio Links in Ethiopia

Rainfall rate distributions for ten geographical locations in Ethiopia are determined at 15-minute sampling rain rate. The R-H model is then used to convert the local measurement of annual rainfall accummulation into one-minute integration time rain rate distribution. Also, the rainfall rate and fade margin contour maps at 0.01% exceedance are developed for Ethiopia. Using the ITU-R model, specific rain attenuation and total rain attenuation for terrestrial Line-of-Sight links in Ethiopia are predicted for varying frequencies and distances. It is found that the attenuation for shorter link paths is more affected by rainfall than longer distance due to non-uniformity of rain distribution over the link. In descending order, the attenuation of rainfall rate is the highest in Bahirdar, followed by Jimma, Kombolcha, AddisAbaba, Adama, Arbaminch, Diredawa, Mekele, Negele Borena and least in Dubti. The data from these maps will be useful as preliminary design tools for terrestrial microwave engineers.

7.1.4 Chapter Five - Characterization and Generation from Markov Chains for Rain Fade Modeling over Wireless Links in Ethiopia

Markov chain and queue models were studied for the characterization and generation of time series rainfall events for a place where rainfall data is inadequate over radio links. From statistical measurements, it was determined that sojourn times of rainfall spikes follow Erlang-k probability distribution and correlates with rain fade duration of rainy channel. From the result, the steady state vectors show that the percentage of occurrence probability of rainfall spikes increases from drizzle to thunderstorm regimes in Jimma. The synthetically generated time series rainfall events from Markov and queue models were compared with the actual rainfall events measurements exhibiting a good preservation of statistical characteristics. Analysis of rainfall traffic from these approaches is useful to understand the performance of wireless rainy channels under the influence of rain or to deal with rain fade mitigation. More fascinatingly, these concepts in the future can be further developed to model wireless channel states according to the corresponding rainfall rate states for radio wave propagation.

7.1.5 Chapter Six - Attenuation Measurements from Received Signal Level of Terrestrial Line-of-Sight Link

From 10 months extensive signal level measurements between Addis Ababa and Furi, the fade depth at different percentage of exceedance modelled. The measurements spans from June 2015 to March 2016 at operating frequency of 11 GHz. five fade depth levels were analyzed in each of the phases. These fade depth levels are: A = 10 dBm, A = 15 dBm, A = 20 dBm, A = 23 dBm, and greater than 23 dBm. The percentage of time exceeded for each season at these fade depth levels was determined. The average minimum threshold signal level value was calculated monthly and seasonally for further performance analysis of fade depth. The kernel density estimator was applied for the curve fitting with the measured signal level pdf. The type of kernel which results in a minimum error was adopted. Network outages were observed more in the Summer season due to high rainfall during this season.

7.2 Future Work

- More locations should be covered in the Horn of Africa for the future research. This is the fact that the more observation sites included in the study, the more diversified

the climate and topographical structure and seasonal variations that will be studied. This will finally increase the reliability and robustness of future work.

- Correlation of the received signal level measurements with Geo-climatic factor is recommended for future study.
- The study of raindrop size distribution from distrometer or derivation of raindrop size distribution from rainfall rate in Ethiopia and Horn of Africa is suggested for future study.
- The characterization and generation of rainfall time series using Markov model concept should be expanded to incorporate rainfall data from various locations and climatic regions of the world.
- The concepts of Markov chain model can be further developed to model wireless rainy channel states according to the corresponding rainfall rate states for radio wave propagation for future work.

References

[1] S. Begum, "Reliable broadband satellite-integrated network design through propagation and networking solutions," PhD Dissertation, University of Glamorgan, 2009.

[2] R. K. Crane, *Propagation Handbook for Wireless Communication System Design.* CRC Press, 2003.

[3] G. Radha and M. Rao, "Addendum to study on coastal atmospheric effects on los links located in visakhapatnam," *AU J.T.*, vol. 10, no. 4, pp. 276 – 281, 2007.

[4] ITU-R, "Characteristics of precipitation for propagation modelling," in *ITU-R Rec. P.837 - 5.*, Geneva, 2001.

[5] R. K. Crane, *Electromagnetic Wave Propagation Through Rain.* John Wiley, 1996.

[6] H. M. Barclay and M. Hewitt, *Propagation of Radiowaves.* London: IEE Press, 1996.

[7] W. Asen and T. Tjelta, "A novel method for predicting site dependent specific attenuation rain attenuation of millimeter radio waves," *IEEE Trans. Commun.,*, vol. 51, no. 10, pp. 2987 – 2999, 2003.

[8] R. L. Freeman, *Radio System Design for Telecommunications.* John Wiley & Sons Inc., 1997.

[9] M. Grabner, V. Kvicera, P. Pechac, and M. Mudroch, "Multipath fading measurement and prediction on 10 *ghz* terrestrial link," in *Proceedings of IEEE 15th Conference of Microwave Techniques*, 2010, pp. 145 – 148.

[10] J. Bogucki and E. Wielowieyska, "Empirical season's fading's in radio communication at 6 ghz band," *Journal of Telecommunications and Information Technology*, vol. 2, no. 10, pp. 48 – 52, 2009.

[11] M. van de Kamp, J. K. Tervonen, E. T. Salonen, and J. P. V. P. Baptista, "Improved models for long-term prediction of tropospheric scintillation on slant paths," *IEEE Trans. Antennas Propagat.*, vol. 47, no. 2, pp. 249 – 260, 1999.

[12] P. K. Odedina, "Clear-air radioclimatological modeling for terrestrial line of sight links in southern africa," Doctor of Philosophy thesis in Electronic Engineering, University of KwaZulu-Natal, Durban, 2010.

[13] ITU-R, "Propagation data and prediction methods required for the design of terrestrial line-of-sight systems," in *Recommendation ITU-R P.530-15*, Geneva, 2013.

[14] G. O. Ajayi, S. Feng, S. M. Radicella, and B. M. R. (Eds.), "Handbook on radiopropagation related to satellite communications in tropical and subtropical countries," pp. 2–14, 1996.

[15] W. Myers, "Comparison of propagation models," in *IEEE 802.16 Broadband Wireless Access Working Group, IEEE 802.16cc-99/13*, 1999, pp. 1–7.

[16] F. Moupfouma and J. Tiffon, "Raindrop size distribution from microwave scattering measurements in equatorial and tropical climates," *Electron Lett.*, vol. 18, no. 2, pp. 1012 – 1014, 1982.

[17] F. Moupfouma, "Improvement of a rain attenuation prediction method for terrestrial microwave links," *IEEE Trans. Antennas and Propag*, vol. 32, no. 12, pp. 1368 – 1372, 1984.

[18] H. E. Green, "Propagation impairment on ka-band satcom links in tropical and equatorial regions," *IEEE Trans. Antennas Propagat.Mag*, vol. 46, no. 2, pp. 31 – 44, 2004.

[19] R. K. Crane, *Electromagnetic Wave Propagation Through Rain.* John Wiley.

[20] D. V. Rogers and R. L. Olsen, "Calculation of radiowave attenuation due to rain at frequencies up to 1000 ghz," in *Commun. Res. Centre Rep. No. 1299*, Commun. Res. Centre Rep. No. 1299, 1976, pp. 42–43.

[21] T. Oguchi, "Attenuation and phase rotation of radio waves due to rain: Calculation at 19.3 and 34.8 ghz," *Radio Sci.*, vol. 8, no. 1, pp. 31 – 38, 1973.

[22] S. H. . Lin, "A method for calculating rain attenuation distributions on microwave paths," *IEEE Trans. Antennas Propag.*, vol. 54, no. 6, pp. 1051 – 1086, 1975.

[23] S. Lin, "Nationwide long-term rain rate statistics and empirical calculation of 11-ghz microwave rain attenuation," *Bell Syst. Tech. J.*, vol. 56, no. 9, pp. 1581 – 1604, 1977.

[24] F. Moupfouma, "A new theoretical formulation for calculation of the specific attenuation due to precipitation particles on terrestrial and satellite radio link," *Int. J. Sat. Commun.*, vol. 15, pp. 89 – 99, 1997.

[25] F.Moupfouma, "Electromagnetic waves attenuation due to rain: A prediction model for terrestrial or l.o.s shf and ehf radio communication links," *J. Infra, Milli., Tetrahertz Waves*, vol. 30, no. 6, pp. 622 – 632, 2009.

[26] C. Matzler, "Drop-size distributions and mie computations for rain," in *IAP Research Report*, Uni. Bern, Switzerland, 2002b, pp. 2 – 16.

[27] M. Filho, F. C., R. S. Cole, and A. D. Sarma, "Millimeter-wave rain induced attenuation: Theory and experiment," *IEE Proc. Part H, Microwave Antennas Propag.*, vol. 133, no. 4, pp. 308 – 314, 1986.

[28] Garcia-Lopez, J. A., and J. Peiro, "Simple rain-attenuation-prediction technique for terrestrial radio links," *Electron Lett.*, vol. 19, no. 21, 1983.

[29] R. Olsen and T. Tjelta, "Worldwide techniques for predicting the multipath fading distribution on terrestrial los links: Background and results of tests," *IEEE Transactions on Antenna and Propagation*, vol. 47, no. 1, pp. 157 – 170, 1999.

[30] R. K. Crane, "Prediction of attenuation by rain," *IEEE Trans. Commun.*, vol. 28, no. 9, pp. 1717 – 1733, 1980.

[31] P. Maagt, G. Brussard, and J. A. Allnut, "Results of 1.2 ghz propagation experiments in indonesia," *Electron Lett.,*, vol. 29, no. 22, pp. 1988 – 1990, 1986.

[32] N. K. Uzunoglu, B. G. Evans, and A. R. Holt, "Scattering of electromagnetic radiation by precipitation particles and propagation characteristics of terrestrial and space communication systems," *IEE Proc*, vol. 124, no. 5, pp. 417 – 424, 1977.

[33] J. S. Seybold, *Introduction to RF Propagation*. John Wiley and Sons Inc., 2005.

[34] P. Odedina and T. Afullo, "Estimation of secondary radioclimatic variables and its application to terrestrial los link design in south africa," in *Proceedings of the Southern Africa Telecommunication Networks and Applications Conference (SATNAC)*, Wild Coast Sun, South Africa, 2008, pp. 1–6.

[35] T. Afullo and P. Odedina, "Effective earth radius factor measurement and modeling for radio link design in botswana," *South Africa Institute of Electrical Engineers Research Journal*, vol. 99, no. 3, pp. 77 – 86, 2008.

[36] P. Odedina and T. Afullo, "A simplified statistical modeling of radioclimatological parameters for los links in south africa," in *Proceedings of Progress in Electromagnetic Research Symposium (PIERS)*, Beijing China, 2009, pp. 1483 – 1486.

[37] P. Odedina and Afullo, "Alternative formulation for determination of geoclimatic factor using local radiosonde data from southern africa," in *Sixth IASTED Conference on Antennas, Radar and Wave Propagation*, Banff AB Canada, 2009, pp. 31–36.

[38] M. Fashuyi and T. Afullo, "Modeling of attenuation due to rain at 19.5 ghz for line-of sight radio systems in south africa," in *the North American Radio Science Meeting, (URSI 2007)*, Ottawa ON Canada, 2007, pp. 2 – 4.

[39] T. Afullo and M. Fashuyi, "Rain attenuation prediction and modeling for los links on terrestrial paths in south africa," *Radio Science*, vol. 42, pp. 1 – 15, 2008.

[40] M. Odedina and T. Afullo, "Determination of rain attenuation from electromagnetic scattering by spherical raindrops: Theory and experiment," *Radio Science*, vol. doi:10.1029/2009RS004192, 2010.

[41] A. A. Alonge and T. J. Afullo, "Characteristics of rainfall queues over radio links at subtropical and equatorial africa," *Radio Science*, vol. 49, pp. 583–596, 2014.

[42] A. Alonge and T. J. Afullo, "Fractal analysis of rainfall event duration for microwave and millimetric networks," *IET journal of microwave antennas and propagation*, vol. 9, pp. 291 – 300, 2014.

[43] A. Maitra, "Rain attenuation modelling from measurements of rain drop size distribution in the indian region," *IEEE Antennas Wireless Propag. Lett*, vol. 3, pp. 180 – 181, 2004.

[44] P. Owolawi, T. Afullo, and S. Malinga, "Effect of rainfall on millimeter wavelength radio in goughand marion islands," in *Progress in Electromagnetics Research Symposium,*, Beijing, China, March 23- 27,2009.

[45] S. Malinga, P. Owolawi, and T. Afullo, "Computation of rain attenuation through scattering at microwave and millimeter bands in south africa," in *Progress in Electromagnetics Research Symposium*, Taipei, 2013.

[46] M. Odedina and T. Afullo, "Characteristics of seasonal attenuation and fading for line-of-sight links in south africa," in *SATNAC*, Taipei, 2008.

[47] A. Alonge, "Regime analysis of rainfall drop-size distribution models for microwave terrestrial networks," *IET Microwave, Antennas and Propagation*, vol. 6, no. 4, pp. 393–403, 2012.

[48] M. Fashuyi and T. Afullo, "Rain attenuation and modelling for line-of-sight links on terrestrial paths in south africa," *Radio Science*, vol. 42, pp. 1 – 15, December 2007.

[49] A. M. Marcus and B. Patta, "Millimeter wave propagation-spectrum management implications," *IEEE Microwave Magazine*, vol. 6, pp. 54 – 61, 2005.

[50] G. Fairhurst, S. L. Pang, and P. Wan, "Smart codec: an adaptive packet data," *IEE*, vol. 145, pp. 180 – 185, 1998.

[51] F. Moupfouma, "Improvement of a rain attenuation prediction method for terrestrial microwave links," *IEEE Transactions on Ant. and Prop.*, vol. 32, no. 12, pp. 1368 – 1372, 1984.

[52] L. J. Ippolito, *Radiowave Propagation in Satellite Communications.* Van Nostrand Reinhold Company Inc.: springer, 1986.

[53] H. Sizun, *Radiowave Propagation for Telecommunication Applications.* Springer, 2005.

[54] R. L.Freeman, *Radio System Design for Telecommunications*, 3rd ed. John Wiley & Sons Inc., 2007.

[55] ITU-R, "The radio refractive index: Its formula and refractivity data," in *ITU-R P.453 - 11*, Geneva, 2011.

[56] ITU, "Propagation data and prediction methods required for the design of terrestrial line-of-sight systems," in *Recommendation ITU-R P.530 - 16*, Geneva, 2015.

[57] P. K. Odedina and T. J. Afullo, "Use of spatial interpolation technique for determination of geoclimatic factor and fade depth calculation in southern africa," in *Proceedings of IEEE AFRICON Conference*, Windhoek, Namibia, 2007, pp. 1–7.

[58] ITU-R, "The radio refractive index: its formula and refractivity data," in *Recommendation ITU-R P.453 - 9*, Windhoek, Namibia, 2009.

[59] Ayantunji, P. Okeke, J. Urama, and Y. Najib, "A semi-empirical model for extrapolation of surface refractivity over nigeria," *African Review of Physics*, vol. 6, no. 14, pp. 121 – 128, 2011.

[60] T. Tjelta, R. Olsen, and L. Martin, "Systematic development of new multi-variable techniques for predicting the distribution of multipath fading on terrestrial microwave links," *IEEE Transactions on Antenna and Propagation*, vol. 38, pp. 1650 – 1665, 1990.

[61] K. Ghosh, P. P. Bhattacharya, and P. K. Das, "Effect of multipath fading and propagation environment on the performance of a fermat point based energy efficient geocast routing protocol," *International Journal of Wireless & Mobile Networks (IJWMN)*, vol. 4, no. 1, pp. 215 – 224, 2012.

[62] W. T. Barnett, "Multipath propagation at 4, 6 and 11 ghz," *Bell System Technical Journal*, vol. 51, no. 2, pp. 321 – 361, 1972.

[63] A.Vingants, "Space diversity engineering," *the bell sybtem techmcal journal*, vol. 54, no. 1, pp. 103 – 142, 1975.

[64] A. Dabideen, M. Gopichund, and T. Afullo, "Radio refractivity distribution and duct and fading occurrence measurements in kwazulu-natal," *Transactions of South African Institute of Electrical Engineers (SAIEE)*, vol. 96, no. 2, pp. 121 – 132, 2005.

[65] K. Morita, "Prediction of rayleigh fading occurrence probability of lineof- sight microwave links," *International Journal of Wireless & Mobile Networks (IJWMN)*, vol. 18, pp. 810 – 821, 1970.

[66] R. Houze, "Stratiform precipitation in regions of convection: A meteorological paradox?" *Bulletin of the American Meteorological Society,*, vol. 78, no. 10, pp. 2179 – 2196, 1997.

[67] J.S.Mandeep and J. Allnut, "Rain attenuation predictions at ku-band in south east asia countries," *Progress in Electromagnetic Research*, vol. 76, no. 1, pp. 65 – 74., 2007.

[68] F. Moupfouma, "More about rainfall rates and their prediction for radio systems engineering," *IEE Proc.*, vol. 134, no. 6, pp. 527 – 537, 1987.

[69] I. Adimula and G. Ajayi, "Variation in raindrop size distribution and specific attenuation due to rain in nigeria," *Ann. Telecom*, vol. 51, no. 1 - 2, pp. 87–93, 1996.

[70] T. J. O. Afullo, "Raindrop size distribution modeling for radio link design along the eastern coast of south africa," *Progress in Electromagnetic Research B*, vol. 34, pp. 345 – 366, 2011.

[71] A. Alonge and T. Afullo, "Regime analysis of rainfall drop-size distribution models for microwave terrestrial network," *IET Microwave Antennas Propag.*, vol. 6, no. 4, pp. 393 – 403, 2012c.

[72] D. Emiliani, L. Luini, and C. Capsoni, "Performance analysis of rain fades on microwave earth-to-satellite links in bangladesh," *IEEE Antennas and Propagation Magazine*, vol. 51, no. 3, pp. 70 – 84, 2009.

[73] G. Ajayi and E. Ofoche, "Some tropical rain rate characteristics at ile-ife for microwave and millimeter wave applications," *Journal of Climate and Applied Meteorology*, vol. 23, pp. 562 – 567, 1984.

[74] M. Islam, T. Rahman, S. Rahim, K. Al-Tabatabaie, and A. Abdulrahman, "Fade margins prediction for broadband fixed wireless access (bfwa) from measurements in tropics," *Progress In Electromagnetics Research C*, vol. 11, pp. 199 – 212, 2009.

[75] S. Malinga, P. Owolawi, and T. Afullo, "Computation of rain attenuation through scattering at microwave and millimeter bands in south africa," in *Progress in Electromagnetics Research Symposium Proceedings*, Taipei.

[76] C. Capsoni and L. Luini, "A physically based method for the conversion of rainfall statistics from long to short integration time," *IEEE trans Antennas*, vol. 57, no. 11, pp. 3566 – 3569, 2009.

[77] P. Watson, M. Gunes, B. Potter, B. Sasthiaseelan, and J. Leitas, *Development of a climatic map of rainfall attenuation for Europe.* University of Bradford, 1981.

[78] R. Flavin, "Rain attenuation considerations for satellite paths," *Telecom. Australian Research Laboratories*, vol. 6, no. 2, pp. 11 – 24, 1982.

[79] B. Segal, "The influence of rain gauge integration time on measured rainfall-intensity distribution functions," *J. of Atmospheric and Oceanic Tech*, vol. 3, pp. 662 – 671, 1986.

[80] G. Ajayi, S.Feng, S. Radicella, and B. R. (Ed), "Handbook on radiopropagation related to satellite communications in tropical and subtropical countries," 1996.

[81] P. Owolawi, "Derivation of one-minute rain rate from five-minute equivalent for the calculation of rain attenuation in south africa," *PIERS Online*, vol. 7, no. 6, 2011.

[82] M. O. Fashuyi, P. A. Owolawi, and T. J. Afullo, "Rainfall rate modeling for los radio systems in south africa," *South African Institute of Electrical Engineering Journal*, vol. 97, no. 1, March 2006.

[83] O. O. Obiyemi, "Performance analysis of rain rate models for microwave propagation designs over tropical climate," *Progress in Electromagnetics Research*, vol. 39, pp. 115 – 122, 2014.

[84] M. S. Singh, K. Tanaka, and M. Lida, "Conversion of 60-, 30-, 10- and 5-minute rain rates to 1-minute rates in tropical rain rate measurement," *ETRI*, vol. 29, no. 4, 2007.

[85] L. Holmberg, Philip., R. Nettie, and Rice:, "Cumulative time statistics of surface-point rainfall rates," *in IEEE Transactions on Communications*, vol. 21, no. 10, pp. 1131–1136, 1973.

[86] B. Heiko, "Markov chain model for vegetation dynamics," *Electronics Letters*, vol. 126, pp. 139 – 154, 2000.

[87] C. Alasseur, A. Nunez, F. Fontan, L. Hussona, U.-C. Fiebigc, and P. Marino, "Two approaches for effective modelling of rain-rate time-series for radio communication system simulations," *Space Communications*, vol. 20, 2005/2006.

[88] A. Alonge, "Queueing theory approach to rain fade analysis at microwave and millimeter bands in tropical africa," Doctor of Philosophy thesis in Electronic Engineering, University of KwaZulu-Natal, Durban, 2015.

[89] A. A. Alonge and T. J. Afullo, "Characteristics of rainfall queues over radio links at subtropical and equatorial africa," *Radio Sci.*, vol. 49, 2014.

[90] D. Carey and C. Haan, "Markov process for simulating daily point rainfall," *J.Irrig. and Drain Div.*, vol. 104, 1978.

[91] B. Heder and J. Bitos, "General n - state markov model for rain attenuation times series generation," *Space Communications*, vol. 46, 2008.

[92] L. E. Braten and T. Tjelta, "An improved three-state semi-markov propagation model optimised for land mobile satellite communication," in *Proc. AP2000 Millennium Conference on Antennas and Propagation*, April 9- 14 2000.

[93] A. A. Alonge and T. J. Afullo, "'rainfall time series synthesis from queue scheduling of rain event fractals over radio links," *Radio Sci.*, vol. 49, 2015.

[94] A. T. Alonge, A.A., "Approximate queue scheduling for rainfall synthesis over radio links in subtropical regions," in *IEEE Africon*, Addis Ababa; Ethiopia, 14 - 17 sept, 2015.

[95] M. Grabner, V. Kvicera, P. Pechac, and M. Mudroch, "Multipath fading measurement and prediction on 10 ghz terrestrial link," pp. 145 – 148, 2010.

[96] R. Olsen, "Radioclimatological modeling of propagation effects in clear-air and precipitation conditions: Recent advances and future directions," in *in Proceedings of Radio Africa '99 Conference*, Gaborone, Botswana, 1999, pp. 92 – 106.

[97] ITU-R, "Effects of tropospheric refraction on radiowave propagation," in *ITU Radiocommunication Study Group III,p.834-4*, Geneva.

[98] T. Afullo and P. Odedina, "On the k-factor distribution and diffraction fading for southern africa," *South African Institute of Electrical Engineers Research Journal*, vol. 47, no. 2, pp. 172 – 181, 2006.

[99] P. Odedina and T. J. Afullo, "Use of spatial interpolation technique for determination of geoclimatic factor and fade depth calculation in southern africa," in *Proceedings of IEEE AFRICON Conference*, Windhoek, Namibia, 2007.

[100] K. Pearson, "Method for the prediction of the fading performance of a multisection microwave link," *Proc. Inst. Elec. Eng*, vol. 112, pp. 1291 – 1300, 1965.

[101] A. Alonge and T. Afullo, "Seasonal analysis and prediction of rainfall effects in eastern south africaat microwave frequencies," *Progress in Electromagnetics Research B*, vol. 40, 2012.

[102] M.O.Asiyo and T. J. Afullo, "Spatial interpolation for mapping geo-climatic factor k in south africa." in *PIERS Proceedings*, Taipei, March 25 - 28, 2013.

[103] P. A. Owolawi, "Rainfall rate probability density evaluation and mapping for the estimation of rain attenuation in south africa and surrounding islands," *Progress in Electromagnetics Research*, vol. 112, pp. 155 – 181, December 2011.

[104] M. Azpurua and K. D. Ramos, "A comparison of spatial interpolation methods for estimation of average electromagnetic field magnitude," *Progress in Electromagnetics Research M*, vol. 14, September 2010.

[105] F. Moupfouma, "Improvement of a rain attenuation prediction method for terrestrial microwave links," *IEEE Transactions on Ant. and Prop.*, vol. 32, no. 12, 1984.

[106] K. L. Bashar and M. M. Rashid, "Performance analysis of rain fades on microwave earth-to-satellite links in bangladesh," *International Journal of Engineering and Technology*, vol. 4, no. 7, pp. 1368 – 1372, 2014.

[107] A. A. Alonge and T. J. Afullo, "Rainfall microstructural analysis for microwave link networks: Comparison at equatorial and subtropical africa," *Progress in Electromagnetics Research B*, vol. 59, 2014.

[108] ITU-R, "Propagation data and prediction methodsrequired for the design of earth-space telecommunication systems," in *in Recommendation ITU-R P.618-11*, Geneva, 2013.

[109] S. Malinga, P. Owolawi, and T. Afullo, "Estimation of terrestrial rain attenuation at microwave and millimeter wave signals in south africa using the itu-r model," in *in PIERS Proceeding*, Kuala Lumpur, Malaysia, March 27 - 30, 2012., pp. 952 – 962.

[110] S. Malinga, P. O, and T. Afullo, "Determination of specific rain attenuation using different total cross section models for southern africa," vol. 105, 2014.

[111] P. O. Akuon and T. J. O. Afullo, "Rain cell sizing for the design of high capacity radio link systems in south africa," *Progress in Electromagnetics Research B*, vol. 35, 2011.

[112] P. A. Owolawi and T. J. Afullo, "Rainfall rate probability density evaluation and mapping for the estimation of rain attenuation in south africa and surrounding islands," *Progress in Electromagnetics Research*, vol. 112, pp. 155– 181, 2011.

[113] Kesavan, "Rain attenuation prediction for terrestrial microwave link in bangladesh," *in Journal of Electrical and Electronics Engineering*, vol. 7, pp. 63 – 67, 2014.

[114] U. Kesavan, A.R.Tharek, and A. Rahman, "Comparative studies of the rain attenuation predictions for tropical regions," *Progress in Electromagnetics Research*, vol. 18, pp. 17 –30, 2011.

[115] S. M. Sharif, "Microwave signal attenuation due to rainfall in sudan," in *The six African workshop on Wireless Use of Information*, vol. 6, Oct 2007.

[116] S. Walkerand, Y. Eyesus, K. Tesfaye, E. Bekele, A. Yeshana, and G. Mamo, "The use of agro climatic zones as a basis for tailored seasonal rainfall forecasts for the cropping systems in the central rift valley of ethiopia," in *Conference: insights and Tools for Adaptation*, Kuala Lumpur, Malaysia, November 2003.

[117] M. Belda, E. H. andT. Halenka, and J. Kalvova, "Climate classification revisited: from kÃűppen to trewartha," *in Climate Research*, vol. 59, pp. 1–13, 2014.

[118] ITU-R, "Characteristics of precipitation for propagation modeling," in *ITU-R P.837-6*, vol. 6, 2012.

[119] P. Watson, M. Gunes, B. Potter, B. Sasthiaseelan, and J. Leitas, *Development of a climatic map of rainfall attenuation for Europe.* University of Bradford, 1981.

[120] J. C. and. T.A. Rahman, "Development of 1 minrain rate contour maps for microwave applications in malaysian peninsula," *1999*, vol. 35, no. 20.

[121] A. Y. Abdulrahman, T. A. Rahman, S. K. Rahman, and R. Islam, "A new rain attenuation conversion technique for tropical regions," *Progress In Electromagnetics Research B*, vol. 26, 2010.

[122] C. Ito and Y. Hosaya, "Worldwide 1-min. rain rate distribution prediction method which uses thunderstorm ratio as regional climatic parameter," *Electronic Letters*, vol. 35, no. 18, 1999.

[123] F. Moupfouma and L. Martin, "Modeling of the rainfall rate cumulative distribution for the design of satellite and terrestrial communication systems," *Electronics Letters*, vol. 13, no. 2, pp. 105 – 115, 1995.

[124] O. O. Obiyemi, J. S. Ojo, and T. S. Ibiyemi, "The influence of raingage integration time on measured rainfall-intensity distribution functions," *J. of Atmospheric and Oceanic Tech*, vol. 3, pp. 662–671, 1986.

[125] ITU-R, "Specific attenuation model for rain for use in prediction methods," in *in Recommendation ITU-R P.838-3*, Geneva, 1992 - 1999 - 2003 - 2005.

[126] K. Gabriel and J. Neumann, "A markov chain model for daily rainfall occurrences at tel aviv," vol. 88, 1962.

[127] B. Heder and J. Bitos, "General n - state markov model for rain attenuation times series generation," *Space Communications*, vol. 46, 2008.

[128] B. Maruddani, A. Kurniawan, Sugihartono, and A. Munir, "Rain fade modelling using hidden markov model for tropical area," in *PIERS Symposium proceedings*, Cambridge, USA, 5-8 July, 2010.

[129] L. Kleinrock, *Queueing Systems.* John Wiley, 1975, vol. I - Theory.

[130] Hillier, S. F.and, and J. G. Lieberman, *Introduction to Operations Research*, 7th ed. McGraw-Hill, 1975.

[131] B. G. S. Greiner, H. de Meer, and K. S. Trivedi, *Queueing Networks and Markov Chains: Modelling and Performance with Computer Science Application.* John Wiley, 1998.

[132] D.R.Wingo, "Computing maximum-likelihood parameter estimates of the generalized gamma distribution by numerical root isolation," *Space Communications*, vol. 36, 1987.

[133] J. Sztrik, *Basic Queuing Theory.* University of Debrecen, Faculty of Informatics, 2012.

[134] B. Nelson, *Stochastic Modeling: Analysis and Simulation.* Dover Publications, 2002.

[135] S. Mark, "Characterizations of strong ergodicity for continuous time markov chains," 1979.

[136] F. D. Diba and T. J. Afullo, "Estimation of rain attenuation over microwave and millimeter bands for terrestrial radio links in ethiopia," in *IEEE Africon*, Addis Ababa; Ethiopia, 14 - 17 sept, 2015, pp. 805–810.

[137] F. D. Diba, T. J. Afullo, and A. A. Alonge, "Rainfall rate and attenuation performance analysis at microwave and millimeter bands for the design of terrestrial line-of-sight radio links in ethiopia," *SAIEE Africa Research Journal*, vol. 107, no. 3, 2016.

[138] M. O. Odedina, "A semi-empirical formulation for determination of rain attenuation on terrestrial radio links," Doctor of Philosophy thesis in Electronic Engineering, University of KwaZulu-Natal, Durban, 2010.

[139] E. V. Schnell, M.and U-C. Fiebig and C. Catalan, "Propagation impairments and impact on system design," in *Cost Action 255 Final Rep*, March, 2002.

[140] F. N. R. Cole and D. webb, "Cumulative fading and rainfall distribution for a 2.1 km, 38 ghz, vertically polarized, line-of-sight link," *IEEE Trans. Antennas Propag*, vol. 56, no. 4, pp. 1085 – 1093, 2008.

[141] M. O. Odedina and T. J. Afullo, "Characterization of rain attenuation and its application to terrestrial communication systems in south africa," in *In the 6th IASTED Intl. Conf. on Antennas, Radar and Wave Propag.*, Alberta, Canada, 5 - 6. July, 2009a.

[142] A. M. Nyete and T. J. O. Afullo, "Seasonal distribution modeling and map-ping of the effective earth radius factor for microwave link design in south africa," *Progress in Electromagnetics Research B*, vol. 51, pp. 1–32, December 2013.

[143] M. O. Asiyo and T. J. O. Afullo, "Statistical estimation of fade depth and outage probability due to multipath propagation in southern africa," *Progress In Electromagnetics Research B*, vol. 46, 2013.

[144] B. Silverman, *Density Estimation for Statistics and Data Analysis*. Chapman and Hall, 1990.

[145] E. Viste, D. Korecha, and A. T. Sorteberg, "Recent drought and precipitation tendencies in ethiopia," *Theoretical and applied climatology*, vol. 112, pp. 535–551, 2013.

Appendix A-1: Nomenclature of frequency bands [6]

Table 1: Nomenclature of frequency bands [6]

Frequency range	Wavelength	Descriptive designation	
Below 3 KHz	Above 100 km		ELF
3-30 KHz	10-100 km	Myriametric waves	VLF
30-300 KHz	1-10 km	Kilometric waves	LF
300-3000 KHz	100-1000m	Hectometric waves	MF
3-30 MHz	0-100m	Decametric waves	HF
30-300 MHz	1-10 m	Metric waves	VHF
300-3000 MHz	10-100 cm	Decimetric waves	UHF
3-30 GHz	1-10 cm	Centimetric waves	SHF
30-300 GHz	1-10 mm	Millimetric waves	EHF
300-3000 GHz	0.1-1 mm	Sub-millimetric waves	
3-30 THz	10-100 μ m	Far-infrared waves	
30-430 THz	0.7-10 μ m	Near-infrared waves	
430-860 THz	0.35-0.7 μ m	Optical waves	

Appendix B:ITU-R Parameters for the Estimation of Specific Attenuation [125]

The ITU-R recommendation P. 838-3 document gives the procedure for estimating the specific attenuation at different frequencies by applying two power-law coefficients, k and . The independent parameter is given as the rainfall rate at 0.01% of the time, R0.01, which is regional dependent. Thus, The specific attenuation is given by:

$$A = KR_{0.01}^{\alpha} \tag{1}$$

The published values of k and α for horizontal and vertical polarization systems are thus presented:

Table 2: ITU-R Parameters for the Estimation of Specific Attenuation [127]

Frequency(GHz)	K_H	α_H	K_V	α_V
1	0.0000259	0.9691	0.0000308	0.8592
1.5	0.0000443	1.0185	0.0000574	0.8957
2	0.0000847	1.0664	0.0000998	0.9490
2.5	0.0001321	1.1209	0.0001464	1.0085
3	0.0001390	1.2322	0.0001942	1.0688
3.5	0.0001155	1.4189	0.0002346	1.1387
4	0.0001071	1.6009	0.0002461	1.2476
4.5	0.0001340	1.6948	0.0002347	1.3987
5	0.0002162	1.6969	0.0002428	1.5317
5.5	0.0003909	1.6499	0.0003115	1.5882
6	0.0007056	1.5900	0.0004878	1.5728
7	0.001915	1.4810	0.001425	1.4745
8	0.004115	1.3905	0.003450	1.3797
9	0.007535	1.3155	0.006691	1.2895
10	0.01217	1.2571	0.01129	1.2156
11	0.01772	1.2140	0.01731	1.1617
12	0.02386	1.1825	0.02455	1.1216
13	0.03041	1.1586	0.03266	1.0901
14	0.03738	1.1396	0.04126	1.0646
15	0.0448	1.1233	0.05008	1.0440
16	0.05282	1.1086	0.05899	1.0273
17	0.06146	1.0949	0.06797	1.0137
18	0.07078	1.0818	0.07708	1.0025
19	0.08084	1.0691	0.08642	0.9930
20	0.09164	1.0568	0.09611	0.9847
21	0.1032	1.0447	0.1063	0.9771
22	0.1155	1.0329	0.1170	0.9700
23	0.1286	1.0214	0.1284	0.9630
24	0.1425	1.0101	0.1404	0.9561
25	0.1571	0.9991	0.1533	0.9491
26	0.1724	0.9884	0.9780	0.9421
27	0.1884	1.6948	0.1813	0.9349
28	0.2051	0.9679	0.1964	0.9277
29	0.2224	0.9580	0.2124	0.9203
30	0.2403	0.9485	0.2291	0.9129

Frequency(GHz)	K_H	α_H	K_V	α_V
31	0.2588	0.9392	0.2465	0.9055
32	0.2778	0.9302	0.2646	0.8981
33	0.2972	0.9214	0.2833	0.8907
34	0.3171	0.9129	0.3026	0.8834
35	0.3374	0.9047	0.3224	0.8761
36	0.3580	0.8967	0.3427	0.8690
37	0.3789	0.8890	0.3633	0.3633
38	0.4001	0.8816	0.3844	0.8552
39	0.4215	0.8743	0.4058	0.8486
40	0.4431	0.8673	0.4274	0.8421
41	0.4647	0.8605	0.4492	0.8357
42	0.4865	0.8539	0.4712	0.8296
43	0.5084	0.8476	0.4932	0.8236
44	0.5302	0.8414	0.5153	0.8179
45	0.5521	0.8355	0.5375	0.8123
46	0.5738	0.8297	0.5596	0.8069
47	0.5956	0.8241	0.5817	0.8017
48	0.6172	0.8187	0.6037	0.7967
49	0.6386	0.8134	0.6255	0.7918
50	0.6600	0.8084	0.6472	0.7871
51	0.6811	0.8034	0.6687	0.7826
52	0.7020	0.7987	0.6901	0.7783
53	0.7228	0.7941	0.7112	0.7741
54	0.7433	0.7896	0.7321	0.7700
55	0.7635	0.7853	0.7527	0.7661
56	0.7835	0.7811	0.7730	0.7623
57	0.8032	0.7771	0.7931	0.7587
58	0.8226	0.7731	0.8129	0.7552
59	0.8418	0.7693	0.8324	0.7518
60	0.8606	0.7656	0.8515	0.7486
61	0.8791	0.7621	0.8704	0.7454
62	0.8974	0.7586	0.8889	0.7424
63	0.9153	0.7552	0.9071	0.7395
64	0.9328	0.7520	0.9250	0.7366
65	0.9501	0.7488	0.9425	0.7339
66	0.9670	0.7458	0.9598	0.7313
67	0.9836	0.7428	0.9767	0.7287
68	0.9999	0.7400	0.9932	0.7262
69	1.0159	0.7372	1.0094	0.7238
70	1.0315	0.7345	1.0253	0.7215

Frequency(GHz)	K_H	α_H	K_V	α_V
71	1.0468	0.7318	1.0409	0.7193
72	1.0618	0.7293	1.0561	0.7171
73	1.0764	0.7268	1.0711	0.7150
74	1.0908	0.7244	1.0857	0.7130
75	1.1048	0.7221	1.1000	0.7110
76	1.1185	0.7199	1.1139	0.7091
77	1.1320	0.7177	1.1276	0.7073
78	1.1451	0.7156	1.1410	0.7055
79	1.1579	0.7135	1.1541	0.7038
80	1.1704	0.7115	1.1668	0.7021
81	1.1827	0.7096	1.1793	0.7004
82	1.1946	0.7077	1.1915	0.6988
83	1.2063	0.7058	1.2034	0.6973
84	1.2177	0.7040	1.2151	0.6958
85	1.2289	0.7023	1.2265	0.6943
86	1.2398	0.7006	1.2376	0.6929
87	1.2504	0.6990	1.2484	0.6915
88	1.2607	0.6974	1.2590	0.6902
89	1.2708	0.6959	1.2694	0.6889
90	1.2807	0.6944	1.2795	0.6876
91	1.2903	0.6929	1.2893	0.6864
92	1.2997	0.6915	1.2989	0.6852
93	1.3089	0.6901	1.3083	0.6840
94	1.3179	0.6888	1.3175	0.6828
95	1.3266	0.6875	1.3265	0.6817
96	1.3351	0.6862	1.3352	0.6806
97	1.3434	0.6850	1.3437	0.6796
98	1.3515	0.6838	1.3520	0.6785
99	1.3594	0.6826	1.3601	0.6775
100	1.3671	0.6815	1.3680	0.6765
120	1.4866	0.6640	1.4911	0.6609
150	1.5823	0.6494	1.5896	0.6466
200	1.6378	0.6382	1.6443	0.6343
300	1.6286	0.6296	1.6286	0.6262
400	1.5860	0.6262	1.5820	0.6256
500	1.5418	0.6253	1.5366	0.6272
600	1.5013	0.6262	1.4967	0.6293
700	1.4654	0.6284	1.4622	0.6315
800	1.4335	0.6315	1.4321	0.6334
900	1.4050	0.6353	1.4056	0.6351
1000	1.3795	0.6396	1.3822	0.6365